

ACOUSTIC STUDY OF DISORDERED LIQUID  $^3\text{He}$  IN HIGH-POROSITY SILICA  
AEROGEL

By

HYUNCHANG CHOI

A DISSERTATION PRESENTED TO THE GRADUATE SCHOOL  
OF THE UNIVERSITY OF FLORIDA IN PARTIAL FULFILLMENT  
OF THE REQUIREMENTS FOR THE DEGREE OF  
DOCTOR OF PHILOSOPHY

UNIVERSITY OF FLORIDA

2007

Copyright 2007

by

Hyunchang Choi

To my family

## ACKNOWLEDGMENTS

Most of all, I thank my advisor, Yoonseok Lee for his guidance and encouragement. His enthusiasm for the physics subject and his way of approaching the problems has been very inspiring for me. He tried to help me improve my strengths and overcome my weaknesses. I also thank Mark. W. Meisel. His continuous support sustained my confidence as a research student.

I appreciate the help I received from Jian-sheng Xia, Naoto Masuhara, Carlos L. Vicente and Ju-Hyun Park. Their expertise and efforts on the research were amazing. Their knowledge based on their experience with practical problems was crucial to overcome obstacles that I have encountered. Ju-Hyun Park taught me baby steps at the beginning of my laboratory experience. He was a model student who spends his time gladly for other students when they need help.

I would also like to thank our collaborators outside and inside the physics department for their support. All of the aerogel used in my experiments were grown by Mulder's group at University of Delaware. The acoustic cavity employed for the cw shear impedance measurement was made by Guillaume Gervais in Halperin's group and  $\text{Ca}_{1.5}\text{Sr}_{0.5}\text{RuO}_4$  samples were prepared by Rongying Jin in Mandrus group. The experimental cells and maintenance parts were made by Mark Link and other machinists and consistent supply of liquid  $^3\text{He}$  by Greg Labbe and John Graham enabled us to continue the experiment without interruption. Dori Faust did all the paper work for ordering supplies and more. I could complete my projects with their sincere help.

I cannot neglect to say thank you to my lab mates, Pradeep Bhupathi and Miguel Gonzalez, who spent their valuable time to revise this thesis. From time to time, Byoung Hee Moon inspired me with his creative ideas. Pradeep made the Melting Curve Thermometer, which was used as a main thermometer for the attenuation measurement.

## TABLE OF CONTENTS

	<u>page</u>
ACKNOWLEDGMENTS .....	4
TABLE.....	7
LIST OF FIGURES .....	8
ABSTRACT.....	11
CHAPTER	
1 INTRODUCTION .....	13
1.1 Overview.....	13
1.2 Pure Liquid $^3\text{He}$ .....	14
1.2.1 History .....	14
1.2.2 Fermi Liquid.....	16
1.2.3 Superfluid $^3\text{He}$ .....	21
1.3 Superfluid $^3\text{He}$ in Aerogel .....	25
1.4 Liquid in Porous Media .....	28
2 THE $A_I$ PHASE OF SUPERFLUID $^3\text{He}$ IN 98% AEROGEL.....	35
2.1 Overview.....	35
2.2 Experiments .....	36
2.3 Results.....	42
2.4 Discussion.....	44
3 THE $A$ PHASE OF SUPERFLUID $^3\text{He}$ IN 98% AEROGEL.....	60
3.1 Overview.....	60
3.2 Experiments .....	62
3.3 Results.....	62
3.4 Discussion.....	64
4 ATTENUATION OF LONGITUDINAL SOUND IN LIQUID $^3\text{He}$ /98% AEROGEL.....	76
4.1 Overview.....	76
4.2 Experiments .....	78
4.3 Results.....	81
4.4 Discussion.....	88
5 CONCLUSION.....	106

## APPENDIX

A	ORIGIN SCRIPT FOR MTP CALIBRATION IN THE HIGH FIELD PHASE.....	108
	A.1 MPTfukuyamalessTn.c.....	111
	A.2 MPTfukuyamalow5.c.....	114
B	PARTS OF THE EXPERIMENTAL CELL FOR ATTENUATION MEASUREMENT...	117
C	TYPICAL SETTING FOR NMRKIT II.....	124
D	ORIGIN SCRIPT FOR THE DATA ANALYSIS OF THE ATTENUATION MEASUREMENTS.....	126
E	TRANSPORT MEASUREMENT ON $\text{Ca}_{1.5}\text{Sr}_{0.5}\text{RuO}_4$ .....	133
F	NEEDLE VALVE FOR DR137.....	144
	LIST OF REFERENCES.....	148
	BIOGRAPHICAL SKETCH.....	156

TABLE

<u>Table</u>		<u>page</u>
2-1	Slopes (mK/T) of the splitting for the $A_1$ and $A_2$ transitions.....	59

## LIST OF FIGURES

<u>Figure</u>	<u>page</u>
1-1 Temperature dependence of sound velocity and attenuation of pure $^3\text{He}$ .....	31
1-2 P-H-T phase diagram of superfluid $^3\text{He}$ .....	32
1-3 Gap structures of the superfluid $^3\text{He}$ , the <i>B</i> phase and <i>A</i> phase. ....	33
1-4 Microscopic structure of 98% Aerogel by Haard. ....	33
1-5 P-B-T phase diagram of superfluid $^3\text{He}$ in 98% aerogel.....	34
2-1 Splitting of the phase transition temperature in fields .....	46
2-2 Cut-out views of the experimental cell and the acoustic cavity.....	47
2-3 Schematic diagram of the vibrating wire .....	48
2-4 Arrangement of the experimental cell and the melting pressure thermometer .....	49
2-5 Schematic diagram of the continuous wave spectrometer .....	50
2-6 Frequency sweep for two different spectrometer settings at 28.4 bars and 3 T.....	51
2-7 Zero field acoustic signals at 28.4 bars for different spectrometer settings as a function of temperature.....	52
2-8 For high fields, we used the MPT calibration of Fukuyama's group .....	53
2-9 Acoustic traces for 3, 5, 7, 9, 11, and 15 T at 33.5 bars on warming .....	54
2-10 Acoustic traces for 1, 2 and 3 T .....	55
2-11 Acoustic traces for 3, 5, 7, 9, 11, and 15 T at 28.4 bars on warming .....	56
2-12 Transition temperatures vs. magnetic field for 28.4 and 33.5 bars.....	57
2-13 Degree of splitting for each individual transition vs. magnetic field.....	58
3-1 The Stanford NMR measurement on superfluid $^3\text{He}$ in 99.3% aerogel.....	70
3-2 Cooling and warming traces taken at 28.4 bars and 33.5 bars.....	71
3-3 Acoustic traces of tracking experiments .....	72
3-4 The relative size of the steps for the supercooled aerogel A-B transition .....	73

3-5	Field dependence of the warming <i>A-B</i> transition in aerogel for 28.4 bars .....	74
3-6	The zero field phase diagram of superfluid $^3\text{He}$ in 98% aerogel .....	75
4-1	The attenuation of longitudinal sound in liquid $^3\text{He}$ /aerogel at 16 bars for 15 MHz measured by Nomura <i>et al</i> .....	92
4-2	Schematic diagram of experimental setup .....	93
4-3	Temperature determined by MPT and Pt-NMR thermometer .....	94
4-4	Evolution of receiver signals on warming .....	95
4-5	Velocity of bulk $^3\text{He}$ and liquid $^3\text{He}$ in aerogel at $T_C$ .....	96
4-6	Signal from receiver.....	97
4-7	Linearity test .....	98
4-8	No significant change in attenuation indicates that the heating by the transducer is negligible.....	99
4-9	Receiver signal trace vs. time at 0.4 mK and 29 bars .....	99
4-10	The normalized attenuation in the superfluid phase at 12 and 29 bars as a function of the reduced temperature.....	100
4-11	Phase diagram at zero field.....	100
4-12	Absolute attenuations for pressures from 8 to 34 bars are presented as a function of temperature .....	101
4-13	Normalized attenuation in superfluid.....	102
4-14	Attenuation vs. pressure.....	103
4-15	Zero energy density of states at zero temperature vs. pressure for the unitary and the Born scattering limits.....	104
4-16	Attenuation for normal liquid .....	105
A-1	Origin worksheet, 'Pad'. Input parameters .....	109
A-2	Label control window. ....	109
A-3	Origin worksheet, 'PtoT' .....	110
C-1	The typical NMRkitII setting.....	125

D-1	The screen shot of Origin worksheet for data analysis. ....	127
E-1	A Zero field Phase diagram of $\text{Ca}_{2-x}\text{Sr}_x\text{RuO}_4$ from S. Nakatsuji <i>et al.</i> ....	137
E-2	Picture of a test sample .....	138
E-3	Temperature dependence of the resistance in the absence of magnetic fields.....	139
E-4	Resistance vs. temperature for various levels of excitation at low temperature. ....	139
E-5	The excitation dependence of the resistance for each temperature.....	140
E-6	The temperature dependence of the slopes. ....	140
E-7	Normalized magneto resistance. ....	141
E-8	Field sweeps below 200 G. ....	141
E-9	The position of the shoulder and dip structure in fields vs. temperature.....	142
E-10	Magneto resistance for fields perpendicular to the plane (blue) and $20^\circ$ tilted away from the c-axis (red) at 20mK.....	143
E-11	Magneto resistance for low fields perpendicular to the plane (blue) and $20^\circ$ tilted away from the c-axis (red) at 20mK. ....	143

Abstract of Dissertation Presented to the Graduate School  
of the University of Florida in Partial Fulfillment of the  
Requirements for the Degree of Doctor of Philosophy

ACOUSTIC STUDY OF DISORDERED LIQUID  $^3\text{He}$  IN HIGH-POROSITY SILICA  
AEROGEL

By

Hyunchang Choi

May 2007

Chair: Yoonseok Lee

Major Department: Physics

The effect of disorder is one of the most interesting and ubiquitous problems in condensed matter physics. A fundamental question, “How does a ground state evolve in response to increasing disorder?”, encompasses many areas in modern condensed matter physics, especially in conjunction with quantum phase transitions. We address the same question in the low temperature phases of liquid  $^3\text{He}$ , which is of a special interest since, in its bulk form, it is the most well understood unconventional superfluid and the purest substance known to mankind. Unlike conventional *s-wave* pairing superconductors, the unconventional superconductors are vulnerable to any type of impurity, and this fact has been used to test the unconventional nature of the order parameter in heavy fermion and cuprate superconductors. The aerogel/ $^3\text{He}$  system provides a unique opportunity to conduct a systematic investigation on the effects of static disorder in unconventional superfluids. We have investigated the influence of disorder, introduced in the form of 98% porosity silica aerogel, on the superfluid  $^3\text{He}$  using various ultrasound techniques. Our primary effort is in understanding the complete phase diagram of this relatively new system. In particular, the high magnetic field region of the phase diagram has not been explored until this work, and the nature of the *A*-like to *B*-like transition in this system has not been elucidated. We identified a third superfluid phase emerging in the presence of

magnetic fields, which resembles, in many respects, the  $A_1$ -phase in bulk. Our zero field study of the  $A$ - $B$  transition in aerogel revealed that two phases coexist in a narrow window of temperature right below the superfluid transition. Sound attenuation measurements conducted over a wide range of temperatures and pressures show a drastically different behavior than in bulk. In particular, in the  $B$ -like phase, our results can be interpreted as strong evidence of a gapless superfluid.

# CHAPTER 1 INTRODUCTION

## 1.1 Overview

The effect of disorder is one of the most interesting and ubiquitous problems in condensed matter physics. Metal-insulator transitions [Lee85] and the Kondo effect [He69] are two examples of phenomena in which disorder, in the form of various types of impurities, plays a fundamental role. The influence of disorder on ordered states such as the magnetic or superconducting phase has also attracted tremendous interest, especially in systems that undergo quantum phase transitions [Sac99].

The response of Cooper pairs to various types of impurities depends on the symmetry of the order parameter [And59, Abr61, Lar65]. The strong influence of a small concentration of paramagnetic impurities on a low temperature superconductor is in stark contrast to its insensitivity to nonmagnetic impurities [And59, Abr61]. Unconventional superconductors with *non-s-wave* pairing are vulnerable to any type of impurity [Lar65], and this fact has been used to test the unconventional nature of the order parameter in heavy fermion and cuprate superconductors [Vor93, Tsu00, Ma04].

Given a great deal of quantitative understanding of the intrinsic properties of superfluid  $^3\text{He}$  [Vol90], the aerogel/ $^3\text{He}$  system provides a unique opportunity to conduct a systematic investigation on the effects of static disorder in unconventional superfluids. In this system, a wide range of impurity pair breaking can be attained by continuously varying the sample pressure. Furthermore, the nature of the impurity scattering can be readily altered by modifying the composition of the surface layers, the  $^4\text{He}$  preplating. We have investigated the influence of disorder (98% aerogel) on the superfluid  $^3\text{He}$  using various ultrasound techniques. Our primary effort is focused on understanding the complete phase diagram of this relatively new system.

Especially, the high magnetic field region of the phase diagram had not been explored until this work, and the nature of the  $A$ -like to  $B$ -like transition in this system had not been elucidated. In this study, three main experimental results are presented along with in-depth discussions.

In the rest of this chapter, a brief description of  $^3\text{He}$  physics, with an emphasis on the acoustic properties of Fermi liquids and unconventional BCS superfluids, is presented. High porosity silica aerogel acting as quenched disorder is also discussed in this chapter. In chapter 2, the acoustic impedance measurements, in high magnetic fields, which led us to observe the third superfluid phase, are described. Chapter 3 focuses on the zero field experiment that revealed the existence of the  $B \rightarrow A$  transition and the coexistence of the two phases on warming. The third experiment, the absolute sound attenuation measurement by direct sound propagation, is discussed in chapter 4. Finally in chapter 5, we conclude with a summary of the experimental results, the physical implications, and a few suggestions for future directions. Various supplementary materials are collected in appendices. Especially, low temperature transport measurements on  $\text{Ca}_{1.5}\text{Sr}_{0.5}\text{RuO}_4$

Throughout this thesis, many transition temperatures are mentioned. For example,  $T_C$  and  $T_{AB}$  indicate the superfluid transition temperature and the  $AB$  transition temperature, respectively. In most of the cases, it is clear whether the transition is in the bulk or in aerogel. However, in the case where the distinction is warranted,  $T_{aC}$  or  $T_{aAB}$  are used for the transitions in aerogel.

## 1.2 Pure Liquid $^3\text{He}$

### 1.2.1 History

The isotopes  $^3\text{He}$  and  $^4\text{He}$  are the only two stable isotopes in this universe which remain liquid down to the lowest available temperature. They are light enough that the zero-point

motion overcomes the attractive inter-atomic interaction, which is very weak due to their filled 2s electronic configuration. At low temperatures, the matter-wave duality and the degenerate conditions two main pillars of quantum world emerge as their de-Broglie wavelength becomes comparable to the inter-atomic spacing, providing a reason to call them *quantum liquids*.

It is not surprising that the existence of  $^4\text{He}$  (product of vigorous nuclear fusion) was first observed from the visible spectrum of solar protuberances, considering its minute  $\approx 5$  ppm abundance in the Earth's atmosphere. Fortunately (especially to low temperature physicists), a substantial amount of  $^4\text{He}$  trapped underground can be found in some natural gas wells. The much rarer isotope  $^3\text{He}$  was discovered by Oliphant, Kinsey, and Rutherford in 1933 [Oli33]. Unlike  $^4\text{He}$ , a reasonable amount of  $^3\text{He}$  could only be produced artificially by the  $\beta$ -decay of tritium in nuclear reactors. It is not hard to imagine why the first experiment on pure liquid  $^3\text{He}$  was conducted by Sydorik *et al.* at Los Alamos Scientific Laboratory [Syd49a, b]. In this work, the authors proved that  $^3\text{He}$  indeed condenses into a liquid at saturated vapor pressure, contrary to the predictions of distinguished theorists such as London and Tisza. Since then, a tremendous amount of effort has been poured in this subject and has led to discoveries of various low temperature phases in liquid as well as solid  $^3\text{He}$  [Vol90].

One of the most remarkable properties that these two isotopes share is the appearance of superfluid phases in which liquids can flow through narrow capillaries with almost no friction. The superfluid transition temperature in liquid  $^3\text{He}$  ( $\approx 2$  mK) is three orders of magnitude lower than in liquid  $^4\text{He}$  ( $\approx 2.2$  K), reflecting the fundamental difference in quantum statistics. While a  $^4\text{He}$  atom with zero nuclear spin obeys Bose-Einstein statistics, a  $^3\text{He}$  atom with spin 1/2 follows Fermi statistics. A Bose system prefers to condense into the lowest-energy single particle state, the so called Bose-Einstein condensation (BEC), at a temperature where the wavefunction of the

particle starts to overlap. This BEC usually accompanies the onset of superfluidity as evidenced in liquid  $^4\text{He}$  and dilute cold atoms.

The superfluidity of a Fermi system was first discovered in a metal, mercury, in 1911 by Kammerlingh Onnes [Kam11], although the microscopic understanding of the phenomenon did not come to light until almost a half century later by the theory of Bardeen, Cooper and Schrieffer (BCS) [Bar57]. A bound pair of two electrons, known as a Cooper pair, with a spin singlet and *s-wave* orbital state may be looked upon as a composite boson that is Bose-condensed. Cooper pairs can be formed with an arbitrarily small net attractive interaction in the presence of the filled Fermi sea background. In a conventional superconductor it is known that the attractive interaction is provided by the retarded electron-phonon interaction. For liquid  $^3\text{He}$ , however, the origin of the pairing interaction is not clearly understood microscopically.

In his seminal work on Fermi liquid theory [Lan56, Lan57], Landau conceived a phenomenological theory to provide a theoretical framework for an interacting fermionic many body system at low temperatures with a specific example, liquid  $^3\text{He}$ , in his mind. Since then, liquid  $^3\text{He}$  has served as a paradigm for a Fermi liquid whose nature transcends the realm of fermionic quantum fluids.

### **1.2.2 Fermi Liquid**

At the heart of Landau's Fermi liquid theory is the quasiparticle, a long lived elementary fermionic excitation near the Fermi surface [Mar00]. The energy levels of the interacting system have a one to one correspondence to the ones in a Fermi gas without mixing or crossing levels. The quasiparticle represents the total entity of the bare particle and some effect of the interaction. Therefore it is expected that the mass of a quasiparticle is different from the bare mass. The quasiparticle energy should also depend on the configuration of other quasiparticles around, and this molecular field type interaction can be parameterized by a set of dimensionless numbers,

Landau Fermi liquid parameters,  $\{F_l^s, F_l^a\}$ , where  $l$  indicates angular momentum. More specifically, suppose that an excited state was created by adding a quasiparticle labeled by  $\vec{k}$  (let us assume that the spin quantum number is imbedded here) and the energy of the excited state relative to the ground state is given by  $\xi_{\vec{k}}$ . Any perturbation in the occupancy of the states  $\delta n_{\vec{k}}$  near the Fermi sea would cause a change in the excitation energy  $\varepsilon_{\vec{k}}$  of the quasiparticle  $\vec{k}$  no longer identical to  $\xi_{\vec{k}}$ . The difference between these two values produces a change in the molecular field on the quasiparticle,  $\delta\varepsilon_{\vec{k}}$  via interactions between the quasiparticles,

$$\delta\varepsilon_{\vec{k}} = \frac{1}{V} \sum_{\vec{k}'} f_{\vec{k}, \vec{k}'} \delta n_{\vec{k}'} \quad (1-1)$$

where  $f_{\vec{k}, \vec{k}'}$  is Landau's interaction function which generates the change in energy of a quasiparticle with momentum  $\vec{k}$  by the perturbation in the distribution of quasiparticles with momentum  $\vec{k}'$ , and  $V$  is the volume. In a perfectly isotropic system like liquid  $^3\text{He}$  and at low temperatures, the interaction function should depend only on the angle,  $\theta$ , between the two momenta with the magnitude  $k_F$ . Then, the Landau interaction function can be decomposed into symmetric (orbital) and antisymmetric (spin) parts,

$$f_{\vec{k}, \vec{k}'} = f_{\vec{k}, \vec{k}'}^s + \vec{\sigma} \cdot \vec{\sigma}' f_{\vec{k}, \vec{k}'}^a \quad (1-2)$$

where  $\sigma_i$  is the  $i^{\text{th}}$  Pauli matrix and  $s$  ( $a$ ) denotes symmetric (antisymmetric). This separation is possible only when the spin-orbit coupling is negligible; this is justified in  $^3\text{He}$  since the only spin-orbit coupling is the weak dipole-dipole interaction (less than  $\mu\text{K}$ ). Each interaction function can be expanded for each angular momentum component in terms of a basis set of Legendre polynomials. The dimensionless Landau parameters,  $F_l^s$  and  $F_l^a$  are obtained by

normalizing with the density of states at the Fermi surface,  $N(0) = m^* p_F / \pi^2 \hbar^3 \sim 1 / \varepsilon_F$

[Noz64].

These parameters determine various macroscopic properties of the liquid; conversely, some of these parameters can be determined by various experiments. For example, one finds the effective mass,  $m^*$  from the Galilean invariance

$$m^* / m = 1 + F_1^s / 3. \quad (1-3)$$

It is worth mentioning that Eq. 1-3 is an exact result without further higher order corrections.

This is the most important Fermi liquid correction that renormalizes the density of states at the Fermi energy,  $N(0)$ . Consequently, the heat capacity and the magnetic susceptibility need to be modified accordingly,

$$C_V = \frac{m^* p_F}{3\hbar^3} k_B^2 T. \quad (1-4)$$

$$\chi = \frac{\gamma^2 \hbar^2}{4} \frac{N(0)}{1 + F_0^a}, \quad (1-5)$$

where  $\gamma$  is the gyromagnetic ratio. The magnetic susceptibility also receives a correction through the spin channel led by  $F_0^a$ . The strength of Fermi liquid theory is in the fact that with the knowledge of a few (experimentally determined) Landau parameters, most of the physical properties can be calculated self-consistently since the higher angular momentum components decrease rather rapidly. In  ${}^3\text{He}$ ,  $F_0^s \approx 10 - 90$ ,  $F_1^s \approx 5 - 15$ , and  $F_0^a \approx -(0.70 - 0.75)$  indicating that liquid  ${}^3\text{He}$  is indeed a *strongly* interacting (correlated) system with enhanced effective mass and magnetic susceptibility due to ferromagnetic tendency (minus sign in  $F_0^a$ ).

While the thermodynamic properties of a Fermi liquid resemble those of a Fermi gas with an adequate renormalization through the Fermi liquid parameters, dynamical properties are

unique in the sense that new types of collective modes are predicted to exist in this system [Lan57]. Ordinary hydrodynamic sound (first sound) in a liquid propagates by restoring its local equilibrium through scattering processes. Therefore, it requires the sound frequency to be much smaller than the scattering rate, i.e.,  $\omega\tau \ll 1$ , where  $\omega$  is the sound frequency and  $\tau$  is the relaxation time. The sound velocity,  $c_1$ , which is determined by the compressibility,  $\kappa_N$ , and the sound attenuation,  $\alpha_1$ , which is dominated by viscous processes, are given by [Vol90]

$$c_1^2 = (\rho\kappa_N)^{-1} = \frac{1}{3}(1 + F_0^s)(1 + \frac{1}{3}F_1^s)v_F^2, \quad (1-6)$$

$$\alpha_1 = \frac{2\omega^2}{3c_1^3\rho}\eta, \quad (1-7)$$

where  $\rho$ ,  $\eta$ ,  $\omega$  are the mass density, the viscosity and the sound frequency, respectively. At low temperatures ( $\ll 1$  K), the sound velocity at a given pressure is constant in the hydrodynamic regime [Abe61].

In a Fermi liquid  $\tau$  varies as  $1/T^2$  [Wil67]. Therefore, at low enough temperatures where  $\tau$  becomes much longer than the period of the sound wave, the conventional restoring mechanism for hydrodynamic sound becomes ineffective. However, Landau realized that new sound modes emerge in the collisionless regime ( $\omega\tau \gg 1$ ) if the relevant Fermi interactions are strong and repulsive enough, and named these excitations as zero sound modes [Lan57]. At zero temperature, a zero sound mode in a Fermi liquid can be pictured as a coherent oscillation of the elastic Fermi surface ringing without damping. Normal modes of this spherical membrane are associated with specific zero sound modes such as longitudinal zero sound (LZS) and transverse zero sound (TZS). As the temperature rises, incoherent thermal quasiparticle scattering prohibits the coherent oscillations of the Fermi surface, causing a damping of zero sound. For longitudinal

zero sound, a strong repulsive  $F_0^s$  value ( $\approx 10 - 90$  depending on pressure) plays a major role in stabilizing this mode with a slightly higher zero sound velocity,  $c_0$ , compared to that of the first sound and attenuation,  $\alpha_0 \propto 1/\tau$ ,

$$c_0 = c_1 \left\{ 1 + \frac{2}{15} \frac{m^*}{m} \left( 1 + \frac{1}{5} F_2^s \right) \left( \frac{v_F}{c_1} \right)^2 + O\left[ \left( \frac{v_F}{c_1} \right)^4 \right] \right\}, \quad (1-8)$$

$$\alpha_0 = \frac{2}{15} \frac{m^*}{m} \frac{\left( 1 + \frac{1}{5} F_2^s \right)^2}{v_F \tau} \left( \frac{v_F}{c_1} \right)^3 \left\{ 1 + O\left[ \left( \frac{v_F}{c_1} \right)^2 \right] \right\}. \quad (1-9)$$

Since  $\tau \propto T^{-2}$ , the first to zero sound crossover occurs by lowering the temperature at a fixed frequency with a trade mark of a symmetric temperature dependence on both sides of broad attenuation maximum (see Fig. 1-1) [Kee63, Abe65, Ket75].

Other than Landau theory, a visco-elastic model can also well describe the first to zero sound transition. Liquid  $^3\text{He}$  possesses not only viscosity as a liquid but also elasticity like a solid [Hal90], and this elastic character is especially pronounced in the collisionless regime [And75, Cas79, Cas80, Vol84]. Therefore, the existence of zero sound modes (especially the transverse zero sound mode, as can be seen below) implies the solid-like character of liquid  $^3\text{He}$  [Kee63, Kee65, Bet65, Abe66, Ki67, Whe70, Rud80]. From the usual kinetic gas formula, the viscosity coefficient,  $\eta$ , can be written as

$$\eta \sim \rho \langle v_F^2 \rangle^{1/2} \ell = \rho \langle v_F^2 \rangle \tau. \quad (1-10)$$

It is based on momentum exchange between quasiparticles with the Fermi velocity,  $v_F$ , and quasiparticle life time,  $\tau$  ( $\ell = v_F \tau$ ). For  $\omega \tau \gg 1$ , the quasiparticles do not have enough time to collide with each other during a period of sound oscillation and the damping becomes weak. The velocity and sound attenuation of the longitudinal sound from a visco-elastic model are given by

$$c_\ell = c_1 + (c_0 - c_1) \frac{\omega^2 \tau_\eta^2}{1 + \omega^2 \tau_\eta^2}, \quad (1-11)$$

$$\alpha_\ell = \frac{c_0 - c_1}{c_1^2} \frac{\omega^2 \tau_\eta}{1 + \omega^2 \tau_\eta^2}. \quad (1-12)$$

The crossover from the first sound to zero sound is clearly represented in these expressions.

Transverse zero sound is another collective mode predicted by Landau. However, the strength of the relevant interaction ( $F_2^s$ ) is marginal in liquid  $^3\text{He}$ . It turns out that the phase velocity of this mode is so close to the Fermi velocity that the mode decays effectively into quasiparticle-hole pairs causing strong damping (Landau damping). The zero sound modes are expected to disappear in the superfluid state as the gap develops at the Fermi level. As will be discussed in the following section, it is of great importance that these modes actually are resurrected in the superfluid by coupling to order parameter collective modes.

### 1.2.3 Superfluid $^3\text{He}$

The BCS theory immediately invigorated the search for a superfluid transition in liquid  $^3\text{He}$ . However, many physicists struggled for longer than a decade in frustration coming from the lack of evidence of the transition and the difficulty in predicting the transition temperature. Finally in 1971, Osheroff, Richardson and Lee [Os72] observed peculiar features on the melting line in a Pomeranchuk cell filled with  $^3\text{He}$ , which indicated some type of transitions. Although their original paper falsely identified them as transitions associated with magnetic transitions in the coexisting solid<sup>1</sup>, detailed NMR experiments [Osh72a] and the help of tremendous intuition provided by Leggett confirmed that the features were indeed superfluid transitions arising from the liquid. In their NMR experiment, they applied a field gradient along the z-axis in order to

---

<sup>1</sup> The title of the paper is “Evidence for New Phases in Solid  $^3\text{He}$ ”.

determine the position and identity of the NMR signal source as either solid or liquid. This was probably the first 1D magnetic resonance imaging experiment, although the work of Paul Lauterbur in 1973 [Lau73] is officially credited as the first magnetic resonance imaging. Today, three phases ( $A$ ,  $B$ ,  $A_I$ ) in the superfluid have been identified experimentally (Fig. 1-2).

The Cooper pairs in all three phases are spin-triplet  $p$ -wave pairing which possesses an internal structure. The general wave function  $\Psi$  for a spin triplet pair is a superposition of all spin substates ( $S_z = -1, 0, +1$ ) as given by

$$\Psi = \psi_{1,1}(\vec{k}) |\uparrow\uparrow\rangle + \psi_{1,0}(\vec{k})(|\uparrow\downarrow\rangle + |\downarrow\uparrow\rangle) + \psi_{1,-1}(\vec{k}) |\downarrow\downarrow\rangle, \quad (1-13)$$

where  $\psi_{1,1}(\vec{k})$ ,  $\psi_{1,0}(\vec{k})$  and  $\psi_{1,-1}(\vec{k})$  are the complex amplitudes for each substate. The theoretical Balian-Werthamer (BW) state [Bal63] that corresponds to the  $B$ -phase is the most stable state in zero magnetic field at low pressures. The  $B$ -phase is composed of all three substates and accordingly has smaller magnetic susceptibility since the  $|\uparrow\downarrow\rangle + |\downarrow\uparrow\rangle$  component is magnetically inert. Because of the pseudo-isotropic gap in this phase as shown in Fig. 1-3 (this is quite unusual for intrinsically anisotropic superfluid), the  $B$ -phase exhibits similar properties to conventional superconductors: for example, an exponential temperature dependence of the specific heat at low temperatures. On the other hand, the Anderson-Brinkman-Morel (ABM) [And60, And61] state ( $A$ -phase) is an equal spin pairing state, constituted by only  $|\uparrow\uparrow\rangle$  and  $|\downarrow\downarrow\rangle$  states. The gap has nodal points at the north and south poles in the direction defined by the angular momentum of the Cooper pair. At high pressures ( $P > 21$  bars), the ABM state is stabilized near  $T_c$  owing to the strong coupling between quasiparticles [Vol90, And73]. The point where normal phase,  $A$ -phase and  $B$ -phase meet at zero field is called the polycritical point

(PCP). The phase transition between  $A$ - and  $B$ -phase is first order as evidenced by strong supercooling of the transition and the discontinuity in heat capacity at the transition.

Magnetic fields have profound and intriguing influences on the phase diagram of pure superfluid  $^3\text{He}$ . Depairing of the  $|\uparrow\downarrow\rangle + |\downarrow\uparrow\rangle$  component in the  $B$  phase by magnetic fields, an effect that is similar to the Clogston-Chandrasekhar paramagnetic limit in a superconductor [Tin96], promotes the growth and appearance of the  $A$ -phase at all pressures. As a result, a magnetic field shifts the first order  $A$ - $B$  transition line to a lower temperature in a quadratic fashion and eventually quenches the  $B$  phase around 0.6 Tesla and 19 bars [Tan91]. In addition to the effect on the  $A$ - $B$  transition, a magnetic field induces a new phase, the  $A_I$ -phase, between the normal and the  $A$ -phase by splitting the second order transition into two second order transitions. The  $A_I$ -phase is very unique in the sense that it contains only  $|\uparrow\uparrow\rangle$  pairs (it is a fully polarized superfluid). A magnetic field generates small shifts in the Fermi levels of up and down spin quasiparticles by the Zeeman energy and, consequently, results in different superfluid transition temperatures (particle-hole asymmetry). Therefore, in the  $A_I$ -phase, only the spin up component participates in forming Cooper pairs. The splitting in transition temperatures (the width of the  $A_I$  phase) is linear in field and symmetric relative to the zero field  $T_C$  in the weak coupling limit since the two spin states form pairs independently. The width of the  $A_I$ -phase in bulk is about  $60 \mu\text{K}/\text{Tesla}$  at melting pressure [Isr84, Sag84, Rem98].

A stable state can be found by searching a state with the lowest free energy. Since the order parameter of superfluid  $^3\text{He}$  grows continuously from the transition temperature (continuous phase transition), the free energy can be expanded in powers of the order parameter as long as the temperature is near the transition temperature (Ginzburg-Landau theory) [Lan59]. The expansion is regulated by the symmetries of the system, and the coefficients for the

expansion can be determined from microscopic theories. The free energy functional ( $f$ ) should have full symmetry that the higher temperature phase possesses. For example, normal liquid  $^3\text{He}$  possesses a full continuous symmetry including time-reversal symmetry. For  $p$ -wave pairing states,  $f$  with a gap amplitude  $\Delta$  is given by

$$f = f_N + \alpha\Delta^2 + \frac{1}{2}\Delta^4 \sum_{i=1}^5 \beta_i I_i, \quad (1-14)$$

where  $I_i$  is the fourth-order invariant of the order parameter and

$$\alpha(T) = -N(0)(1 - T/T_C). \quad (1-15)$$

In the weak coupling limit,

$$\beta_2 = \beta_3 = \beta_4 = -\beta_5 = -2\beta_1 = \frac{6}{5}\beta_0, \quad (1-16)$$

$$\beta_0 = \frac{7}{8\pi^2} \zeta(3) N(0) (k_B T_C)^{-2}, \quad (1-17)$$

and the BW state is found to be the most stable [Bal63]. One can easily expect that there are many local free energy minima (including a few saddle points) in this multi-dimensional manifold space. The hierarchy among these local minima depends on the specific values of the  $\beta_i$ -parameters. For example, as the pressure rises, the  $\beta_i$ 's start to deviate from the weak coupling values mainly due to strong coupling effects (e.g. spin fluctuations). This strong coupling correction helps the ABM phase win over the BW phase. This effect is responsible for the  $A$ -phase appearing above the polycritical point [And60, 61].

Nonzero angular momentum of the Cooper pair allows pair vibration modes, called order parameter collective modes (OPCM). These collective excitations are measured as anomalies in sound attenuation and velocities below  $T_C$ . An attenuation peak by pair breaking can also occur for a frequency above  $2\Delta/\hbar$ . The frequency range of ultrasound (10 ~100 MHz) conveniently

matches with the size of the gap and the spectra of various OPCM's in superfluid  $^3\text{He}$ . The thermally excited quasiparticle background also provides an independent channel for sound attenuation. In particular, sound attenuation from thermally excited quasiparticles decreases exponentially at low temperature as an isotropic gap opens up in the  $B$ -phase.

### 1.3 Superfluid $^3\text{He}$ in Aerogel

High porosity silica aerogel consists of a nanoscale abridged network of  $\text{SiO}_2$  strands with a diameter of  $\sim 3$  nm and a distance of  $\sim 20$  nm. Since the diameter of the strands is much smaller than the coherence length,  $\xi_0$  (15 – 80 nm for 34 – 0 bars [Dob00]) of the superfluid, when  $^3\text{He}$  is introduced, the aerogel behaves as an impurity with the strands acting as effective scattering centers. Although current theoretical models treat aerogel as a collection of randomly distributed scattering centers, one should not lose sight on the fact that the aerogel structure is indeed highly correlated. The microscopic structure of 98% porosity aerogel is shown in Fig. 1-4 [Haa00], where the density is  $0.044 \text{ g/cm}^3$  and the geometrical mean free path is  $100 \sim 200$  nm [Por99, Haa00]. The velocity of longitudinal sound in 98% aerogel was measured as  $50 \sim 100$  m/s [Fri92].

Early studies using NMR [Spr95] and torsional oscillator [Por95] measurements on  $^3\text{He}$  in 98% aerogel found substantial depression in the superfluid transition and superfluid density [Por95, Spr95, Spr96, Mat97, Gol98, All98, He02a, He02b]. The phase diagram of  $^3\text{He}$ /aerogel (with mostly 98% porosity) has been studied using a variety of techniques [Por95, Spr95, Mat97, Ger02a, Bru01, Cho04a, Bau04a]. The phase diagram in P-T-B domain is shown in Fig. 1-5 [Ger02a].

When aerogel is submerged in liquid  $^3\text{He}$ , a couple of solid layers, which are then in contact with surrounding liquid, are formed on the aerogel surface. Therefore, the scattering off

the aerogel surface has elements of both potential scattering and spin exchange scattering. However, the magnetic scattering between the itinerant  $^3\text{He}$  and localized moments in solid layers can be turned off by preplating magnetically inert  $^4\text{He}$  layers on aerogel surface. Although the early NMR measurement by Sprague *et al.* concluded that the  $^4\text{He}$  coating turns the  $A$ -like phase into a  $B$ -like phase at  $\sim 19$  bars [Spr96], the effect of the spin-exchange scattering on the phase diagram is elusive. Alles *et al.* provided evidence of the BW state in aerogel from the textural analysis of NMR line shape [All98]. However, in these early experiments, no evidence of the  $A$ -like to  $B$ -like transitions were observed until Barker *et al.* observed clear transition features below the aerogel superfluid transition only on cooling while exploiting the supercooling effect [Bar00b]. Considering the fact that data collecting in NMR experiments typically done only on warming cycle to minimize the interaction with the demag field, it is not surprising that the earlier experiments could not observe these transitions. Further studies using acoustic techniques [Ger02a, Naz05] and an oscillating aerogel disc [Bru01] have confirmed the presence of the  $A$ - $B$  like transition in the presence of low magnetic fields.

The nomenclature for the two superfluid phases in aerogel as the  $A$ -like and the  $B$ -like phases heavily relies on the spin structure without direct experimental inputs for the orbital structure. Through detailed NMR studies, we now believe that the  $B$ -like phase at least has the same order parameter structure as the BW phase. On the contrary, the identification of the  $A$ -like phase is far from clear since there are many possible phases with a similar spin structure represented by the equal spin pairing [Fom04, Vol06, Fom06, Bar06].

An interesting aspect of  $^3\text{He}$  in 98% porosity aerogel is that no superfluid transition was found down to  $150 \mu\text{K}$  below 6.5 bars [Mat97]. This experimental observation renders us to contemplate a possible quantum phase transition in this system [Bar99].

The first reports of superfluid transition in 98% aerogel were immediately followed by a theoretical model, the homogeneous scattering model (HSM), based on the Abrikosov-Gorkov's theory [Abr61] in which the spin exchange scattering off dilute paramagnetic impurities in *s-wave* superconductors was treated perturbatively. The isotropic homogeneous scattering model (IHSM) [Thu98a, Han98] could provide a successful explanation for the observed suppression of the transition temperatures. In that theory, the ratio of the coherence length,  $\xi_0$ , to the mean free path,  $\ell$ , plays a major role as a pair-breaking factor,  $\xi_0 / \ell$ . The fact that the coherence length in superfluid  $^3\text{He}$  can be tuned by pressure makes this system very attractive in probing a wide range of parameter space of  $\xi_0 / \ell$  without changing the density of the impurity, i.e. the mean free path. Thuneburg was able to provide a better fit to the pressure dependence of  $T_C$  by using an isotropic inhomogeneous scattering model (IISM) [Thu98a].

One cannot ignore a visually evident fact that aerogel strands are by no means a collection of isotropic scattering centers nor small enough to be treated by a purely quantum mechanical scattering theory. Volovik argued that, in the ABM state, the coupling of the orbital part of the order parameter to the randomly fluctuating anisotropic structure, i.e. aerogel, should prevent the onset of a long range order, thereby leaving it as a glass state in the long wavelength limit [Vol96]. Fomin proposed a class of orbitally isotropic equal spin pairing states, so called the robust phase, as another candidate for the *A*-like phase [Fom03]. In contrast, the robust phase has a long range order in the presence of random anisotropy disorder, but as argued by Volovik, it is not more stable than the ABM state from the free energy point of view [Vol05]. Specific NMR frequency shifts have been calculated for both scenarios [Fom06, Vol06].

## 1.4 Liquid in Porous Media

Normal liquid  $^3\text{He}$  in the hydrodynamic regime might be treated as a classical liquid in porous media. Liquids in porous media have been studied for both technical and academic reasons rooted in a broad range of practical applications such as in biological systems and the oil industry [Zho89, Hai99]. Even though practical structure properties (e.g. permeability) of the pore can be, in principle, extracted from ultrasonic measurements [War94, Joh94a, Joh94b], it is appreciated that the motion of fluid in a porous structure is a non-trivial problem and a theoretical challenge. For the classical hydrodynamic fluid, sound is attenuated by various mechanisms, including the friction between liquid and pore surface and the squirt of fluid in narrow cracks [Bio55a, Bio55b, DVor93]. Biot developed a theory for acoustic response for the friction in the high frequency regime (small viscosity) and in the low frequency regime (large viscosity). For longitudinal sound, the attenuation is proportional to  $1/\eta$  in large viscosity regime and to  $\sqrt{\eta}$  in the other regime [Bio55a, Bio55b]. In Dvorkin *et al.*'s model of a water saturated rock, the attenuation from the squirt-flow mechanism is an order of magnitude stronger than the attenuation from the friction [Dvo93].

In the 1950's, Biot developed a theory for sound propagation in a porous elastic media, which is filled with a viscous fluid [Bio55a,b]. He began his study from the Poiseuille type flow which does not have turbulence and is valid at low frequency. Considering the effect of the relative motion between the fluid and the solid, he found two longitudinal waves (first and second kind) and one rotational wave. The liquid and the solid tend to move in phase for the first kind and to move out of phase for the second kind of longitudinal wave. Because the second kind is highly attenuated, only the first kind is the true wave at lower frequencies. An isotropic porous media with uniform pore size is considered for the calculation. He predicted that the

shape of the pores is not important for the frequency dependence of the frictional force. At low frequencies, decrease in viscosity results in more liquid motion and increases the attenuation quadratically as  $T^2$  for the liquid  $^3\text{He}$ . At higher frequencies, Biot accounted for the deviation from Poiseuille flow by replacing the static viscosity with a frequency dependent one. In this regime, only a thin layer of fluid is locked on to the porous surface and a strong attenuation occurs within this layer [War94]. In this case, the attenuation of the first kind wave is proportional to  $1/T$  for the liquid  $^3\text{He}$ .

In 1994, Warner and Beamish measured the velocity and the attenuation of transverse sound in a helium filled porous media [War94]. They could study both the low frequency regime and the high frequency regime. Based on Biot's model, they could determine the structure parameters of the porous media (tortuosity, permeability and effective pore size) from their acoustic measurements.

The dynamic permeability for a number of realistic models with variable pore size was calculated by Zhou and Sheng [Zho89]. They found that the frequency dependence of the dynamic permeability did not depend on the models except two scaling parameters. However, the dynamic permeability of all the models could not be collapsed into a single curve when the throats connecting the pores were very sharp or the porosity was close to 1 [Joh89].

Yamamoto *et al.* also studied the effect of pore size distribution theoretically [Yam88]. They found that the velocity and the attenuation of sound are not affected by the pore size distribution in the low and high frequency limits, but strongly depend on the pore size distribution in the intermediate frequency range. Their prediction agreed with experimental data of attenuation in marine sediments [Ham72]. In the intermediate frequency regime near the low frequency limit, attenuation of the longitudinal sound decreases as pore distribution increases.

Tsiklauri investigated the slip effect on the acoustics of a fluid-saturated porous medium [Tsi02]. In general, in fluid dynamics, it is assumed that the fluid at the surface of the solid moves at the same velocity as the solid does, which is known as the “no-slip boundary condition”. But when slippage occurs between the fluid and the solid surfaces, the so called “slip effect” becomes important, particularly in the case of a highly confined porous media. Biot’s theory can describe acoustics for the scenario of the sloshing motion between a classical Newtonian liquid and the porous frame assuming no slip effect. Tsiklauri introduced a phenomenological frequency dependence of the slip velocity and found that it affects the effective viscosity in the intermediate frequency domain leading to a higher attenuation than what is predicted by the Biot theory. In the low and high frequency limits, his results agreed with the predictions of Biot.

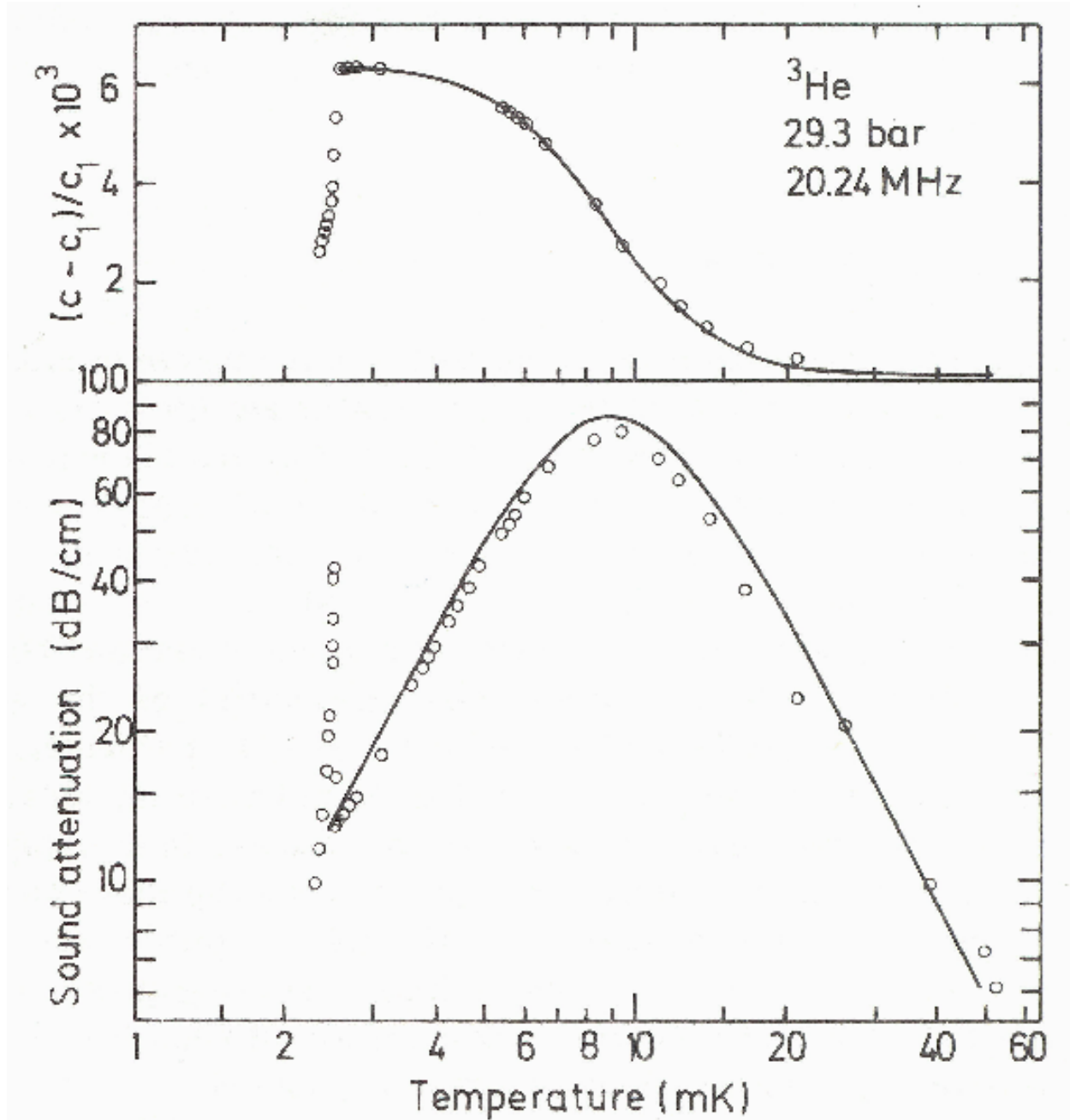


Figure 1-1. Temperature dependence of sound velocity and attenuation of pure  $^3\text{He}$  [Ket75]. The solid lines are the results of fit using Eq. 1-11 and 1-12 [Roa77]. The superfluid transition is signaled by the sharp change near 2 mK. Reprinted figure with permission from P.R. Roach and J.B. Ketterson, in *Quantum Fluids and Solids*, edited by S.B. Trickey, E.D. Adams, and J.F. Duffy (Plenum Press, New York, 1977) p.223. Copyright (1977) by Springer.

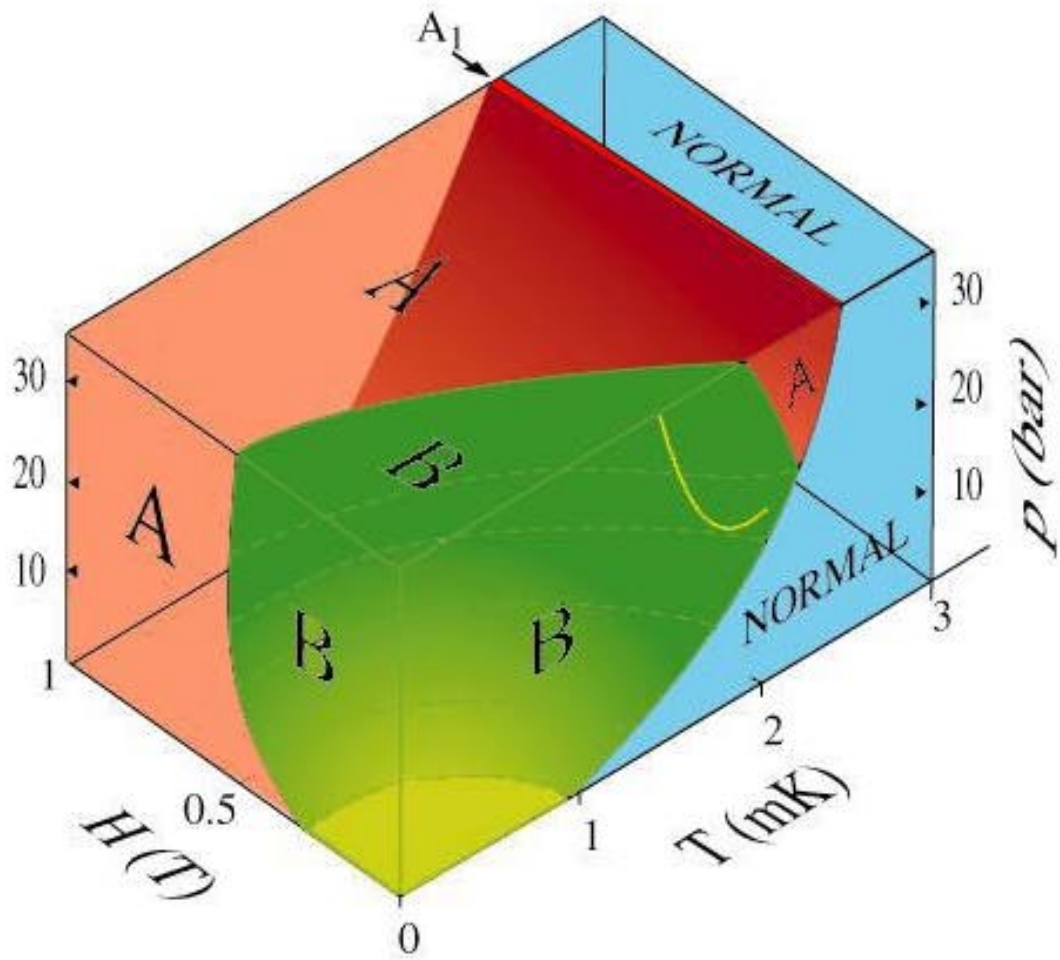


Figure 1-2. P-H-T phase diagram of superfluid  $^3\text{He}$  [Web1].

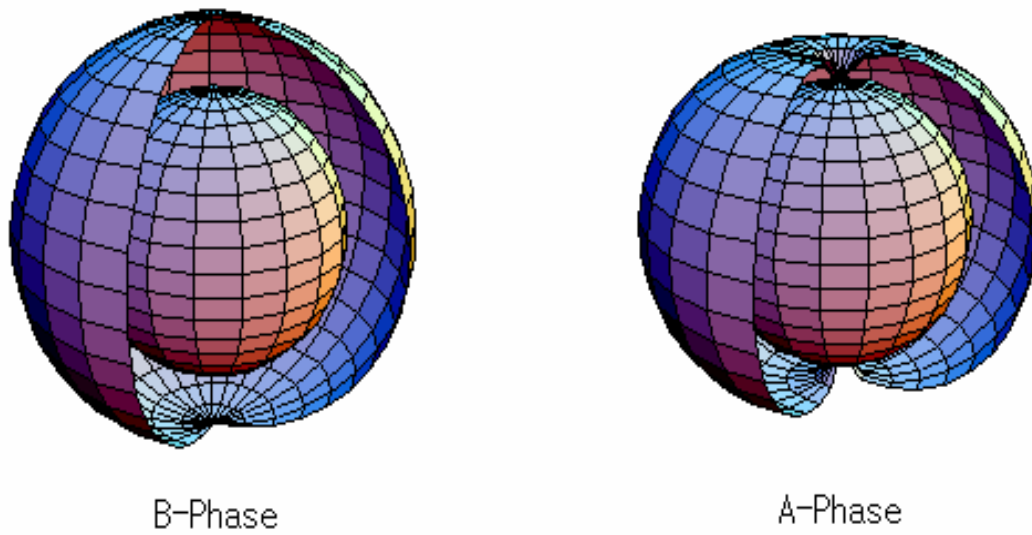


Figure 1-3. Gap structures of the superfluid  $^3\text{He}$ , the *B* phase and *A* phase. The space between inner and outer shell represents a gap amplitude in momentum space.

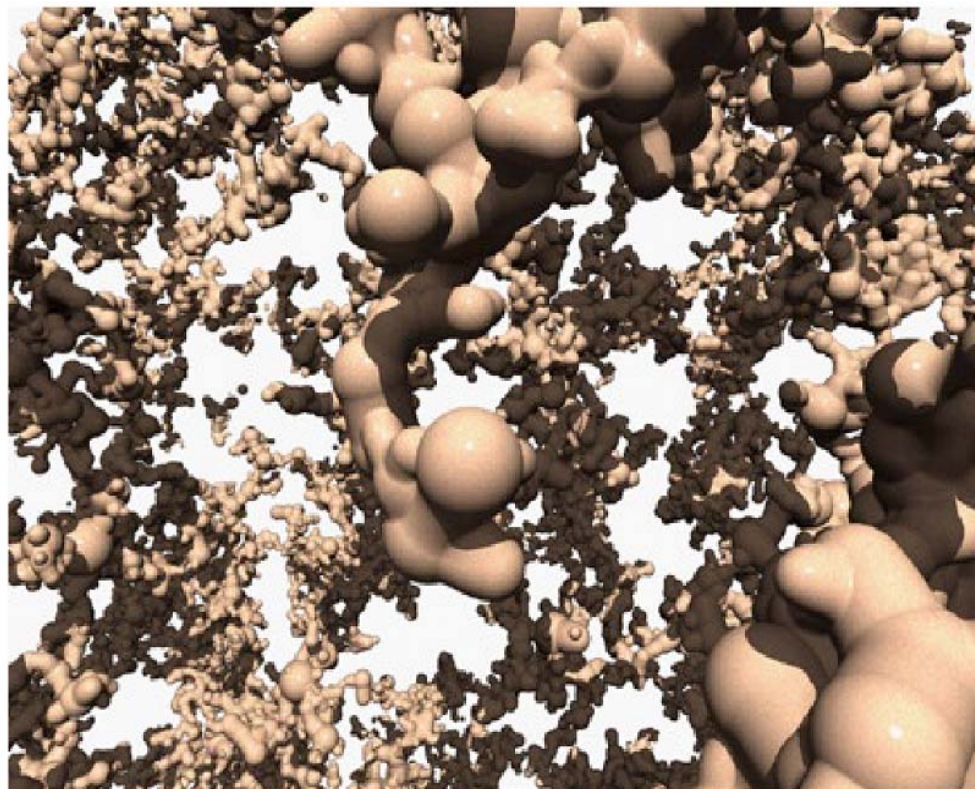


Figure 1-4. Microscopic structure of 98% Aerogel by Haard (computer simulation) [Haa01].

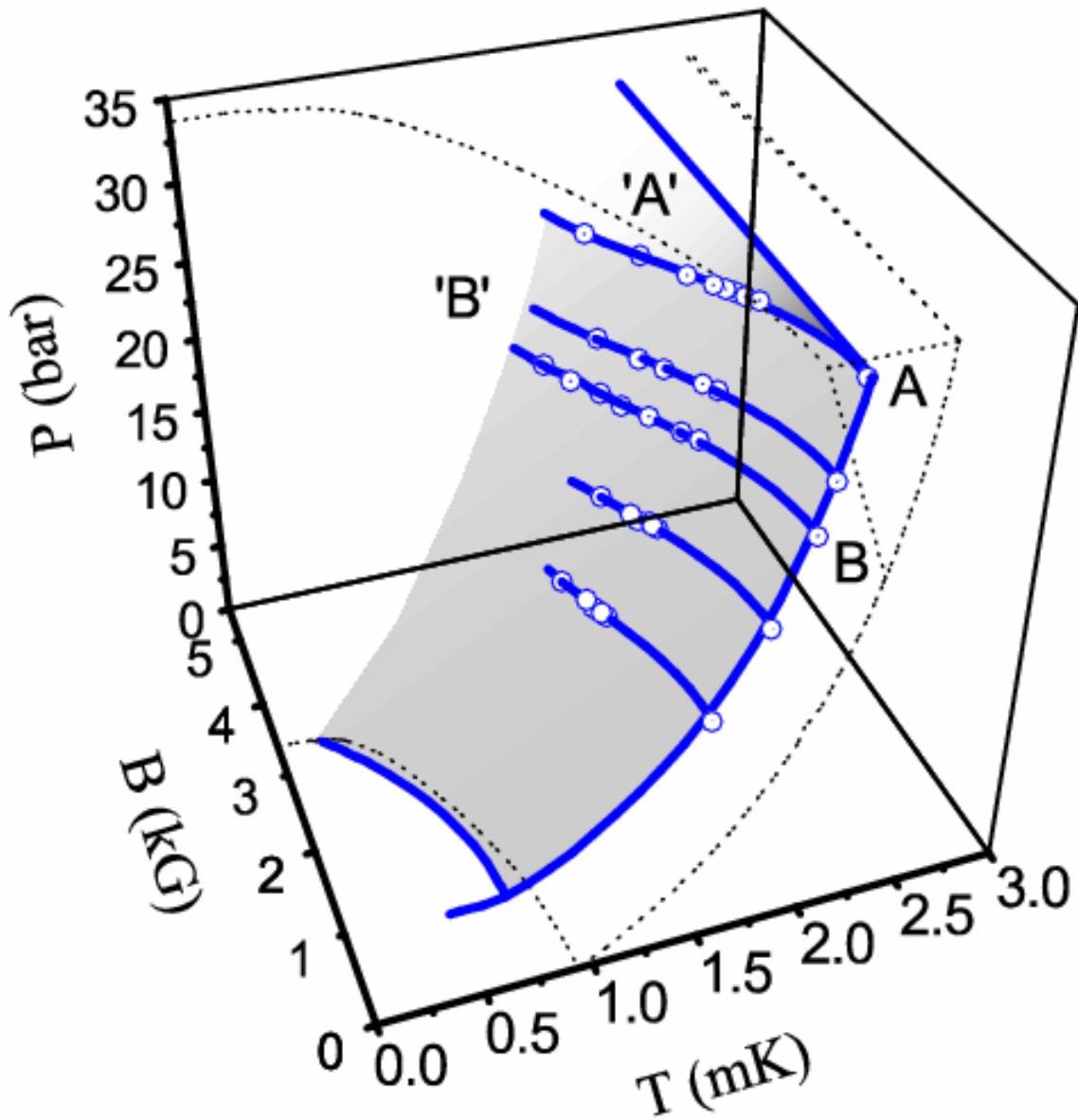


Figure 1-5. P-B-T phase diagram of superfluid  $^3\text{He}$  in 98% aerogel (blue line). Phase diagram for bulk Superfluid  $^3\text{He}$  is shown as a dotted line [Ger02a]. Reprinted figure with permission from G. Gervais, K. Yawata, N. Mulders, and W. P. Halperin, *Phys. Rev. B* **66**, 054528 (2002). Copyright (2002) by the American Physical Society.

CHAPTER 2  
THE  $A_1$  PHASE OF SUPERFLUID  $^3\text{He}$  IN 98% AEROGEL

**2.1 Overview**

In pure superfluid  $^3\text{He}$ , minute particle-hole asymmetry causes the splitting of the superfluid transition through the Zeeman coupling in magnetic fields. As a result, the third phase, the  $A_1$  phase, appears between the normal and the  $A_2$  phase (the  $A$  phase in magnetic fields) [Amb73, Osh74]. In this unique phase, the condensate is fully spin polarized. The  $A_1$  phase has been studied by several groups and the width of the phase was found to increase almost linearly in field by  $\approx 0.065$  mK/T at the melting pressure [Osh74, Sag84, Isr84, Rem98]. Recently, Gervais *et al.* [Ger02a] performed acoustic measurements in 98% aerogel up to 0.5 T and found no evidence of splitting in the transition.

Baramidze and Kharadze [Bar00a] made a theoretical suggestion that the spin-exchange scattering between the  $^3\text{He}$  spins in liquid and solid layers on the aerogel surface could give rise to an independent mechanism for the splitting of the transition. Detailed calculations [Sau03, Bar03] show that antiferromagnetic (ferromagnetic) exchange reduces (enhances) the total splitting in low fields, but one recovers the rate of the particle-hole asymmetry contribution in high fields as the polarization of the localized spins saturates. These calculations were performed with the assumption that the  $A$  phase in aerogel is the ABM state. Figure 2-1 presents the low field data from Gervais *et al.* and the results of the calculation with (green) and without (red) the anti-ferromagnetic exchange. The comparison between the theoretical calculation and the results of Gervais *et al.* suggests that the spin exchange between the localized moments and the itinerant spins is anti-ferromagnetic.

However, Fomin [Fom04] recently formulated an argument that the order parameter of the  $A$ -like phase in aerogel should be inert to an arbitrary spatial rotation in the presence of the

random orbital field presented by the aerogel structure. This condition enforces a constraint on the order parameter for equal spin pairs, he named new state satisfying the constraint as a ‘robust phase’. This theory predicts that an  $A_1$ -like phase would be induced by a magnetic field for a certain condition (e.g., in the weak coupling limit). This is a new type of ferromagnetic phase with nonzero populations for both spin projections – unlike the  $A_1$  phase where only one spin component participates in forming Cooper pairs. However, the splitting of the  $A_1$  and  $A_2$  transitions in this case seems to evolve in a different manner compared to bulk  $^3\text{He}$ . If the  $A$  phase in aerogel is correctly identified as an axial state, then a similar field dependent splitting of the superfluid transition must exist at least in the high field region since the level of particle hole asymmetry is affected only marginally by the presence of high porosity aerogel.

## 2.2 Experiments

The experiment was performed at the High B/T Facility of the National High Magnetic Field Laboratory located at University of Florida. Figure 2-2 shows the cut-out views of the sample cell and the acoustic cavity. The main cell body (except the part of heat exchanger) was originally made out of titanium to reduce the nuclear spin contribution to the heat capacity in magnetic fields. However, a leaky seal was found repeatedly at the silver-titanium epoxy seal and forced us to replace the top part with the one made of coin silver. The top part of the cell body forms a diaphragm so that the cell pressure can be monitored capacitively. We used the same acoustic cavity that was utilized in the work of Gervais *et al.* [Ger02a, Ger02b]. The 98% porosity aerogel was grown inside the acoustic cavity by Norbert Mulders at the University of Delaware. The cavity is composed of a quartz transverse sound (AC-cut) transducer and a longitudinal sound (X-cut) transducer separated by a 0.010” diameter stainless steel wire. The 3/8” quartz transducers were manufactured by Valpey-Fisher (currently Boston Piezo-Optics, Bellingham, MA). The aerogel was grown inside the cavity formed by sandwiching the two

stainless steel wires between the transducers under external force<sup>2</sup>. After the aerogel was grown in the cavity, the copper wires were attached to the transducer with silver epoxy and the cavity was placed on top of a Macor holder, since the vigorous chemical reaction does not allow us to use epoxies or solder before the completion of critical drying process. In this geometry, the transducers are in contact with both bulk liquid and liquid in the aerogel. Therefore, we detected the change in the electrical impedance of the transducer caused by both liquids. The acoustic measurement was performed at the third harmonic resonance, 8.7 MHz, for all the data presented in this chapter.

The volume of the cell is designed to be less than 1 cm<sup>3</sup> to ensure a short thermal relaxation time. The sample liquid in the cell is cooled by the PrNi<sub>5</sub> demagnetization stage (DS) through a 0.9 m-long annealed silver heat link extending below the DS. The transitions in the pure liquid were confirmed independently by a vibrating wire (VW) placed in liquid near the ultrasound transducer [Rem98]. The vibrating wire was made out of 0.1 mm manganin wire bent into a semi-circular shape with a 3.2 mm diameter. The resonance frequency of the VW was 13 kHz. As shown Fig. 2-3, an alternating current is fed through VW by the voltage oscillator, then the Lorentz force causes VW to oscillate. The amplitude of induced voltage across VW at a fixed excitation frequency was measured using a Lock-in amplifier. The amplitude of the induced voltage follows the amplitude and damping of the VW oscillation, which is determined by the viscosity of the surrounding liquid. The acoustic spectrometer output was recorded continuously while the temperature of the sample varied slowly. No significant hysteresis was observed for data taken in both warming and cooling directions. The data presented (if not specified) were taken on warming and the typical warming rate in our study was 0.1 – 0.2 mK/h.

---

<sup>2</sup> Actually aerogel was grown around the whole cavity. All aerogel formed outside of the cavity was removed using tooth pick after the completion of the drying procedure.

Temperature was determined by a  $^3\text{He}$  melting pressure thermometer (MPT) attached to the silver heat link right below the cell in the experimental field region. Figure 2-4 shows the picture of the MPT and the sample cell on the silver heat link.

The spectrometer (Fig. 2-5) used in this experiment was made by Jose Cancino, an undergraduate research assistant [Lee97]. This is a continuous wave (cw) bridge type spectrometer employing a frequency modulation (FM) technique. The FM signal was produced by an Agilent E4423B generator and the rf output was set at 11 dBm. The FM excitation signal was fed into the transducer at its resonance frequency through the first port of a 50 ohm matched quadrature hybrid (QHB, SMC DQK-3-32S). The third port of the QHB was connected to the transducer inside the cryostat. The output signal from the fourth port of the QHB was amplified by a low noise preamplifier (MITEQ, AU-1519) and demodulated by a double balanced mixer (mini-circuits, ZLW-1-1). This procedure converts the FM modulated rf signal into an audio signal at the modulation frequency. The demodulated low frequency signal was detected with a two-channel lock-in amplifier (Stanford Research System, SR530). The impedance mismatch at the transducer causes a reflected signal to appear on the fourth port. The reflected signal from the transducer can be nulled by feeding the (amplitude and phase adjusted) FM signal to the second port of the QHB. The transducer works like a resonator for the FM radio receiver [Kra80]. If the signal to be transmitted and a sinusoidal carrier are given by Eq. 2-1 and Eq. 2-2, the frequency modulated signal can be written as Eq. 2-3.

$$x_m(t) = \cos(\omega_m t) \quad (2-1)$$

$$x_c(t) = x_c \cos(\omega_c t) \quad (2-2)$$

$$V_1(t) = A \cos\left(\int_0^t [\omega_c + \omega_\Delta x_m(\tau)] d\tau\right) = A \cos\left[\omega_c t + \frac{\omega_\Delta}{\omega_m} \sin(\omega_m t)\right] \quad (2-3)$$

$\omega_m$  and  $\omega_c$  are the modulation and carrier frequencies.  $\omega_\Delta$  is the modulation amplitude that regulates maximum shift from  $\omega_c$  [Wik06]. As the FM signal is fed to the resonator, the output signal from the transducer is proportional to the product of the resonator amplitude,  $f(\omega)$ , and the amplitude of the input signal,  $V_1(t)$ . The FM signal has a finite but small oscillation that is centered around  $\omega_c$ . Within this finite region, the slope of the resonance line shape,  $a(\omega)$ , can be taken as a constant. Therefore, the output from the transducer,  $V_2$ , is given by Eq. 2-4. The mixer works as a multiplier of two input signals, which are coming from the transducer through the QHB and from the splitter (mini-circuits, ZFSC-3-1). The multiplied (mixed) signal ( $\propto V_1(t)V_2(t)$ ) has two frequency components, low and high frequency parts. The low frequency part of the signal coming from the mixer is given by Eq. 2-5. Finally, the AC component of this signal is measured by the low frequency lock-in amplifier, which is proportional to  $a(\omega)$ , as shown in Eq. 2-6.

$$V_2(t) \propto f(\omega)V_1(t) = [B + a \frac{\omega_\Delta}{\omega_m} \sin(\omega_m t)]V_1(t) \quad (2-4)$$

$$V_3(t) \propto B + a \frac{\omega_\Delta}{\omega_m} \sin(\omega_m t) \quad (2-5)$$

$$V_4(t) \propto a \quad (2-6)$$

Therefore, the spectrometer detects the slope of the transducer resonance shape,  $a$ , at a given frequency, [Bol71]. In the ideal case, the acoustic response measured by a Lock-in amplifier should produce zero in the 1f mode and a maximum in the 2f mode at resonance. The schematic signal shape at each step is shown in Fig. 2-5. In our measurements, the excitation frequency is fixed at the resonance, while the  $^3\text{He}$  is still in the normal fluid. A large ratio of the modulation amplitude (3 kHz) and the modulation frequency (400 Hz) were chosen to avoid the

discrete nature in frequency spectrum. To be sensitive enough to detect any changes in the slope  $a$ , the modulation amplitude should be chosen such that the magnitude of the deviation from  $\omega_C$  is small compared to the width of the transducer resonance frequency. A crucial part of the measurement is tuning the spectrometer by adjusting the attenuators (JFW, 50R-028) and the phase shifter to produce a null condition for maximum sensitivity. By going through this tedious procedure, better than 1 ppm resolution in frequency shift is achieved.

Figure 2-6 shows the spectrometer outputs obtained by sweeping the frequency through the transducer resonance for two different spectrometer settings at 28.4 bars and 3 T. Frequency sweeps in the normal and deep inside of the superfluid are plotted together. By using Set2, we were able to reduce the asymmetry between the size of maximum and minimum of the acoustic response. It also shifted the crossing point in the normal and superfluid curves closer to zero. Figure 2-7 shows how the spectrometer tuning affects the acoustic response during a temperature sweep. After tuning the spectrometer to shift the crossing point closer to zero, the acoustic responses at  $T_C$  and in the superfluid became almost the same. It can be noticed that Fig. 2-7 (b) shows clearer changes in slope at  $T_{aC}$  and at  $T_{aAB}$  on warming, as opposed to Fig. 2-7 (a). Later on, to obtain the clear slope change, the spectrometer was tuned to produce a symmetric resonance shape in the normal liquid.

At zero field, the Greywall scale [Gre86] was adopted to convert the measured melting pressure to temperature using the solid ordering transition as a fixed point to establish the pressure offset. In the presence of magnetic fields, the calibration by the University of Tsukuba group [Yaw01, Fuk03] was employed. In their work, the calibration was given in two separate regions - the paramagnetic phase and the high field phase of solid  $^3\text{He}$  - up to 14.5 T. However, below 3.5 mK, our region of interest, only the calibration in the high field phase is available.

Consequently, the range of our temperature determination is limited to fields between 7 and 13 T for the pressures of our work. The dash-dotted lines in Fig. 2-8 represent the high field phase transition of the solid  $^3\text{He}$  in the MPT and below the boundary is the region where the calibration is done. The melting pressure in the high field phase was given by Eq. 2-7 [Yaw01], where the fourth-order temperature dependence is expected by spin-wave theory and the sixth-order correction originates from the dispersion correction.

$$P(T;H) = P_o(H) + c_4(H)T^4 + c_6(H)T^6 \quad (2-7)$$

We used interpolated sets of coefficients for the fields applied in our work. The width of the bulk  $A_1$  phase identified in the acoustic trace was used to fix the pressure offset. At each field, the calibration curve  $P(T;H)$  is vertically adjusted so that the measured melting pressure interval of the bulk  $A_1$  phase maps out the correct temperature width at the same experimental condition (two point calibration method). The pressure offsets for all fields (including zero field) are around 6 kPa within 10%. The temperature width of the  $A_1$  phase was obtained using the results from Sagan *et al.* [Sag84] and Remeijer *et al.* [Rem98]. Sagan *et al.* measured the shift of transition temperature in fields for pressures ranging from 6 to 29 bars and determined their splitting ratio (mK/T) from the linear fit. Remeijer *et al.* conducted their experiments only at the melting pressure and performed a fit including a quadratic term. For consistency, our own linear fit from the data of Remeijer *et al.* at the melting pressure and splitting ratio from Sagan *et al.* for other pressures are used to obtain the width of  $A_1$  phase at the pressures studied. By using the  $A_1$  width rather than the actual transition temperature as a fixed point, we can circumvent the possible inconsistency in the absolute temperature scale, which is used in the previous work on the bulk  $A_1$  phase. The data points represented by the solid and open circles in Fig. 2-8 were obtained in this way. For 5 T at 28.4 bars, the aerogel transition temperatures (squares) were

determined by forcing the bulk  $A_2$  transition (diamond) on the linear fit for  $T_{A_2}$  (single point calibration method). We also made an estimation of the aerogel  $A_1$  transition temperatures beyond the field range that our prescribed calibration method allows, by assuming a constant warming rate, which is set by the bulk transition temperatures and time interval. The crosses are obtained in this manner. The agreement between the filled circles and crosses in the overlapping region is excellent and encouraging. The sensitivity of the melting pressure thermometry rapidly declines in higher fields and lower temperatures due to a decrease in solid entropy. For example,  $|dP/dT|$  drops from  $\approx 3.3$  kPa/mK at 2 mK and zero field to  $\approx 0.1$  kPa/mK at 15 T for the same temperature. This intrinsic property of the melting curve, in combination with the enhanced noise in high fields, renders it practically impossible to make an accurate determination of the aerogel  $A_2$  transition temperatures well below the dotted line where  $|dP/dT| \ll 0.1$  kPa/mK. Typical noise in our high field pressure measurement is about  $\pm 4$  Pa. The Origin script for the high field MPT calibration is given on appendix A.

### 2.3 Results

The acoustic traces for six different fields at 33.5 bars are shown in Fig. 2-9. The acoustic trace is plotted along with that of the VW to compare the transition signatures of the bulk liquid. The vibrating wire measurement was done in a similar fashion as described by Remeijer *et al.* [Rem98] and the amplitude at the resonance is shown in the figure. Two sharp cusps in the VW trace correspond to the  $A_1$  and  $A_2$  transitions in pure liquid as reported in a previous work [Rem98]. These features are concurrent with the jumps in the acoustic trace. The transitions in aerogel are not as sharp as in the bulk. However, the smooth slope changes are quite clear and similar signatures of the superfluid transition in aerogel have been observed by Gervais *et al.* [Ger02a]. The field dependent evolution of the transition features is demonstrated in Fig. 2-9.

Below 3 T, we were not able to resolve the double transition features in aerogel while the features from the bulk can be traced down to zero field, merging into one (for example, see Fig. 2-10). As the field increases, the gap between the two transition features in each liquid widens. It is important to emphasize that the bulk  $A_2$  and aerogel  $A_1$  transitions cross each other around 5 T and continue to move apart in higher fields. A similar behavior was observed at 28.4 bars (Fig. 2-11), but the crossing occurred at a different field, around 7 T. The warming traces of the acoustic response are shown in Fig. 2-11 for several fields at 28.4 bars along with those of the vibrating wire (amplitude at resonance).

The straight lines in Fig. 2-12 are the results of linear fits to the data points represented by the open (bulk) and solid (aerogel) circles including zero field results. The slope of each linear fit is listed in Table 2-1. All data points determined by MPT including zero field data (red circles) are used for the fitting with equal weights. The asymmetry in the splitting is of special importance in two ways. First, the asymmetry ratio is a direct measure of strong coupling effects such as spin-fluctuation [Vol90]. Second, it provides a valid self-consistency check for our temperature calibration since only the total width of the splitting has been utilized. The asymmetry ratios are also listed in Table 2-1 where

$$r_{(a)} = -(T_{(a)A1} - T_{(a)C}) / (T_{(a)A2} - T_{(a)C}) \quad (2-8)$$

and  $T_{(a)C}$  is the zero field bulk (aerogel) transition temperature. The bulk slopes and  $r$  are in good agreement, within 8% with previous measurements [Sag84, Rem98]. It is notable that the  $A_1$  slopes for the bulk and aerogel are same in order of magnitude, which is consistent with the theory of Sauls and Sharma [Sau03]. The degree of individual splitting relative to the zero field transition temperature is plotted in Fig. 2-13. For both pressures, the asymmetry in the aerogel is consistently smaller, by 22%, than the bulk value for both pressures.

## 2.4 Discussion

The comparable slopes of the aerogel and bulk transitions suggest that the new phase in aerogel has the same spin structure as the  $A_I$  phase in bulk. The asymmetry ratio is related to the fourth-order coefficients,  $\beta_i$ , in the Ginzburg-Landau free energy expansion as defined by  $r = -\beta_5 / (\beta_2 + \beta_4 + \beta_5)$  [Vol90]. In the weak coupling limit at low pressure,  $r \rightarrow 1$  and the strong coupling effect tends to increase this ratio as pressure rises. Within the spin-fluctuation model, the strong coupling correction factor,  $\delta$ , can be estimated from  $r = (1 + \delta) / (1 - \delta)$  [Vol90]. For 33.5 bars in aerogel,  $\delta \approx 0.09$ . The level of the strong coupling contribution at this pressure corresponds to that of the bulk at around 15 bars [Sag84, Rem98], which indicates substantial reduction of the strong coupling effect. The weakening of strong coupling effects by the presence of impurity scattering has been discussed theoretically [Bar02] and confirmed experimentally through an independent estimation from the field dependent suppression of the  $A$ - $B$  transition by Gervais *et al.* [Ger02a]. In Ginzburg-Landau limit and below the PCP, the width of the  $A$  phase in magnetic field can be derived to have the following form,

$$1 - \frac{T_{AB}}{T_C} = g(\beta) \left( \frac{B}{B_0} \right)^2 + O \left( \frac{B}{B_0} \right)^4. \quad (2-9)$$

Gervais *et al.* extract a value of  $g(\beta)$  at 34 bars in aerogel that also matches that of 15 bars in bulk. It is worth mentioning that  $T_{aC}$  at 33.5 bars also falls on  $T_C$  around 15 bars. However, the  $A_I$ -like phase suggested by Fomin [Fom04] based on the robust phase requires a quite different asymmetry ratio. In this case, the asymmetry ratio

$$r_F = -\{1 + B / (\beta_1 + \beta_5)\}^{-1}, \quad (2-10)$$

where  $B = 9\beta_2 + \beta_3 + 5\beta_4 + 4\beta_5$  and reaches  $\approx 0.16$  in the weak coupling limit [Bar06]. This asymmetry ratio is inconsistent with our observation, even when reasonable variations in the  $\beta$  parameters are allowed. Fomin adopted a condition,  $\Delta_{\uparrow\uparrow} = \Delta_{\downarrow\downarrow}$  in the presence of magnetic fields, to preserve an exact isotropy of the robust phase. According to a recent theoretical work by Baramidze and Kharadze [Bar06], by introducing a small imbalance ( $\Delta_{\uparrow\uparrow} \neq \Delta_{\downarrow\downarrow}$ ) in the Fomin's model, a more symmetric splitting was achieved.

Sauls and Sharma [Sau03] suggested that the anti-ferromagnetic coupling of 0.1~0.2 mK between spins in solid and liquid might be responsible for the suppressed splitting below 0.5 T observed by Gervais *et al.* [Ger02a]. Their calculation shows that the slope of the splitting starts to increase smoothly around 0.5 T ( $\approx$  exchange field strength between spins in solid) and reaches the slope close to that of bulk superfluid in high fields (Fig. 2-1). Our data cannot confirm this behavior owing to the lack of a low field temperature calibration. We point out that the data points acquired by assuming constant warming rate (Fig. 2-12) characteristically fall below the linear fit in the low field region. This fact, along with the observations made in low fields by Gervais *et al.* and us might suggest the presence of antiferromagnetic exchange coupling between the localized and mobile  $^3\text{He}$  spins. This brings up an interesting possibility of a completely new Kondo system.

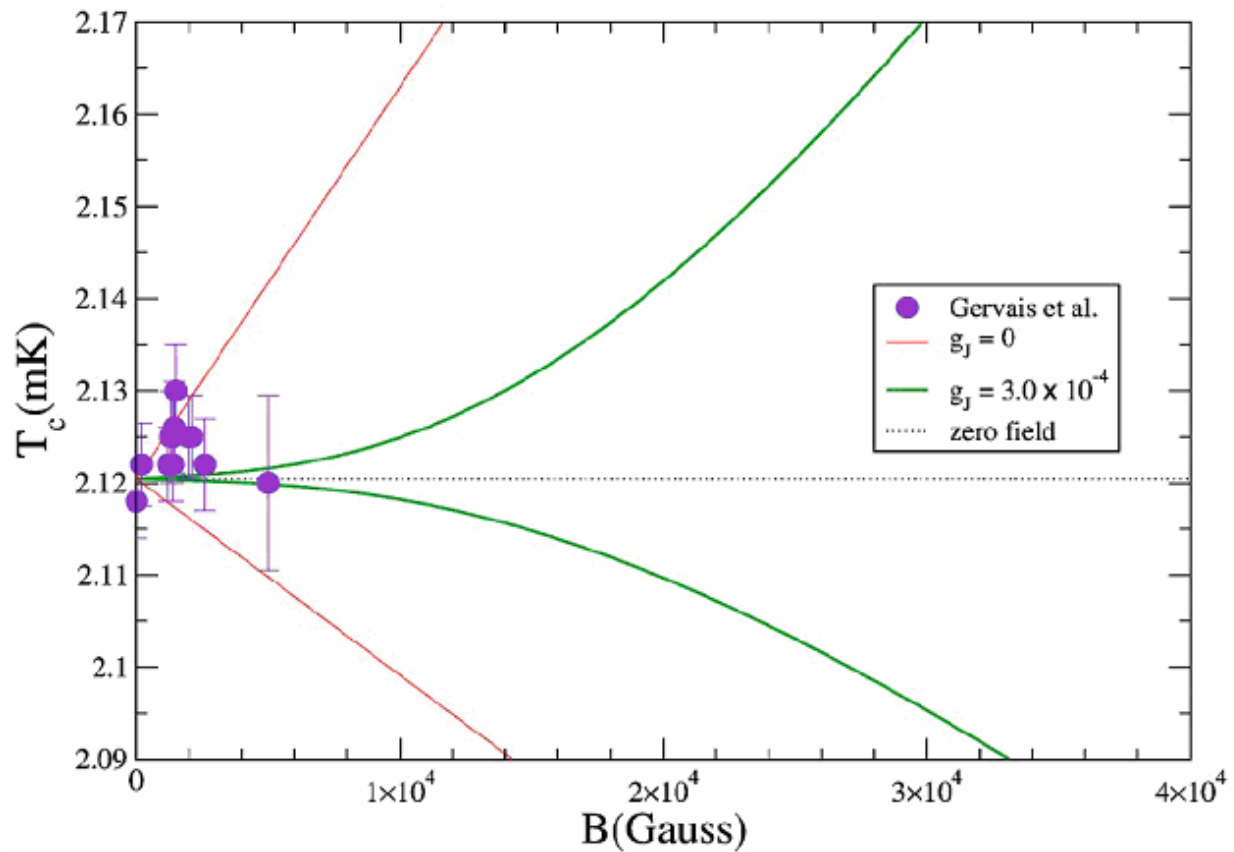
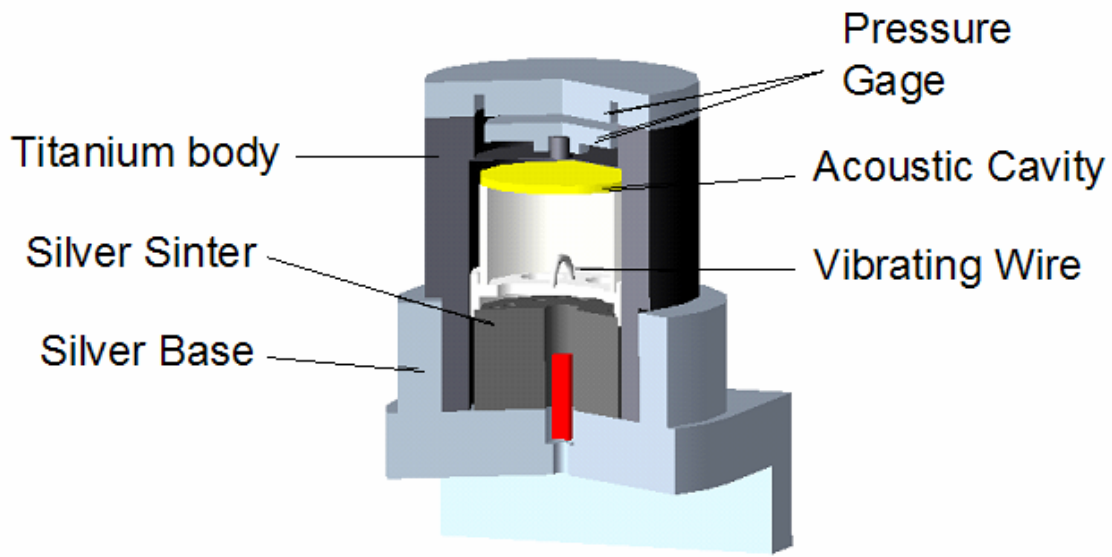
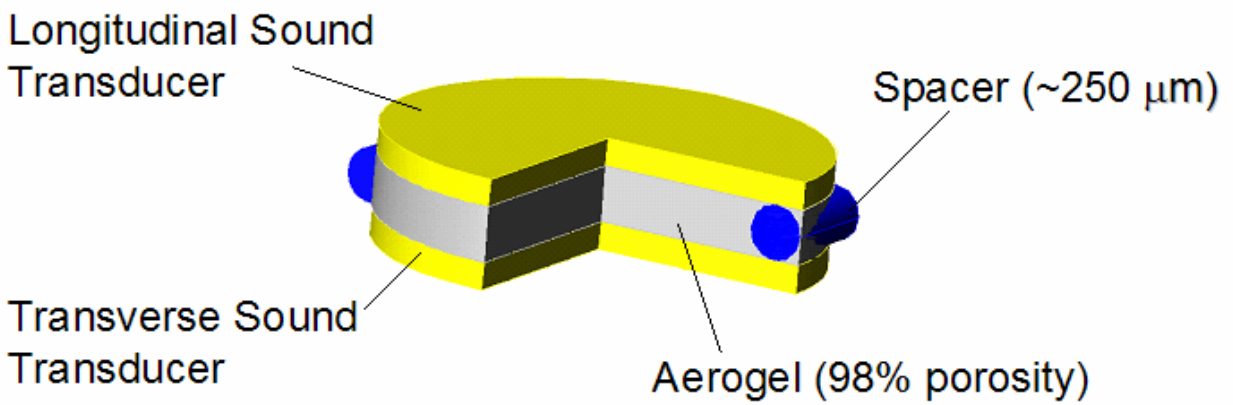


Figure 2-1. Splitting of the phase transition temperature in fields [Sau03]. Circles represent the low field data from Gervais *et al.* [Ger02a] and lines represent the theoretical predictions by Sauls and Sharma [Sau03]. Green lines are calculated including antiferromagnetic exchange between liquid and solid layer of  $^3\text{He}$  and red lines are calculated excluding it. Without the spin exchange interaction, the  $T_c$  splitting is comparable to that of pure  $^3\text{He}$ . Reprinted figure with permission from J. A. Sauls and P. Sharma, Phys. Rev. B 68, 224502 (2003). Copyright (2003) by the American Physical Society.



(a) Experimental Cell



(b) Acoustic Cavity

Figure 2-2. Cut-out views of the experimental cell and the acoustic cavity.

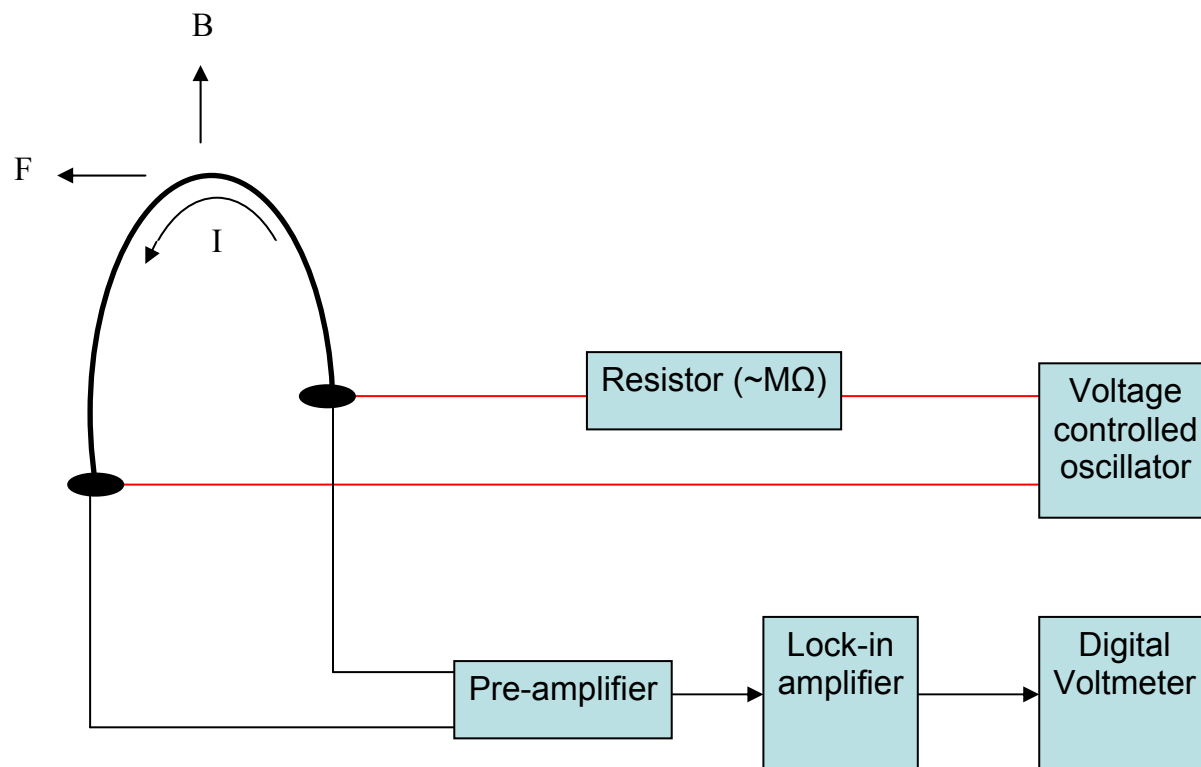


Figure 2-3. Schematic diagram of the vibrating wire (VW).



Figure 2-4. Arrangement of the experimental cell (top) and the melting pressure thermometer (bottom) on the silver heat link extending below the nuclear demagnetization stage to the high field region.

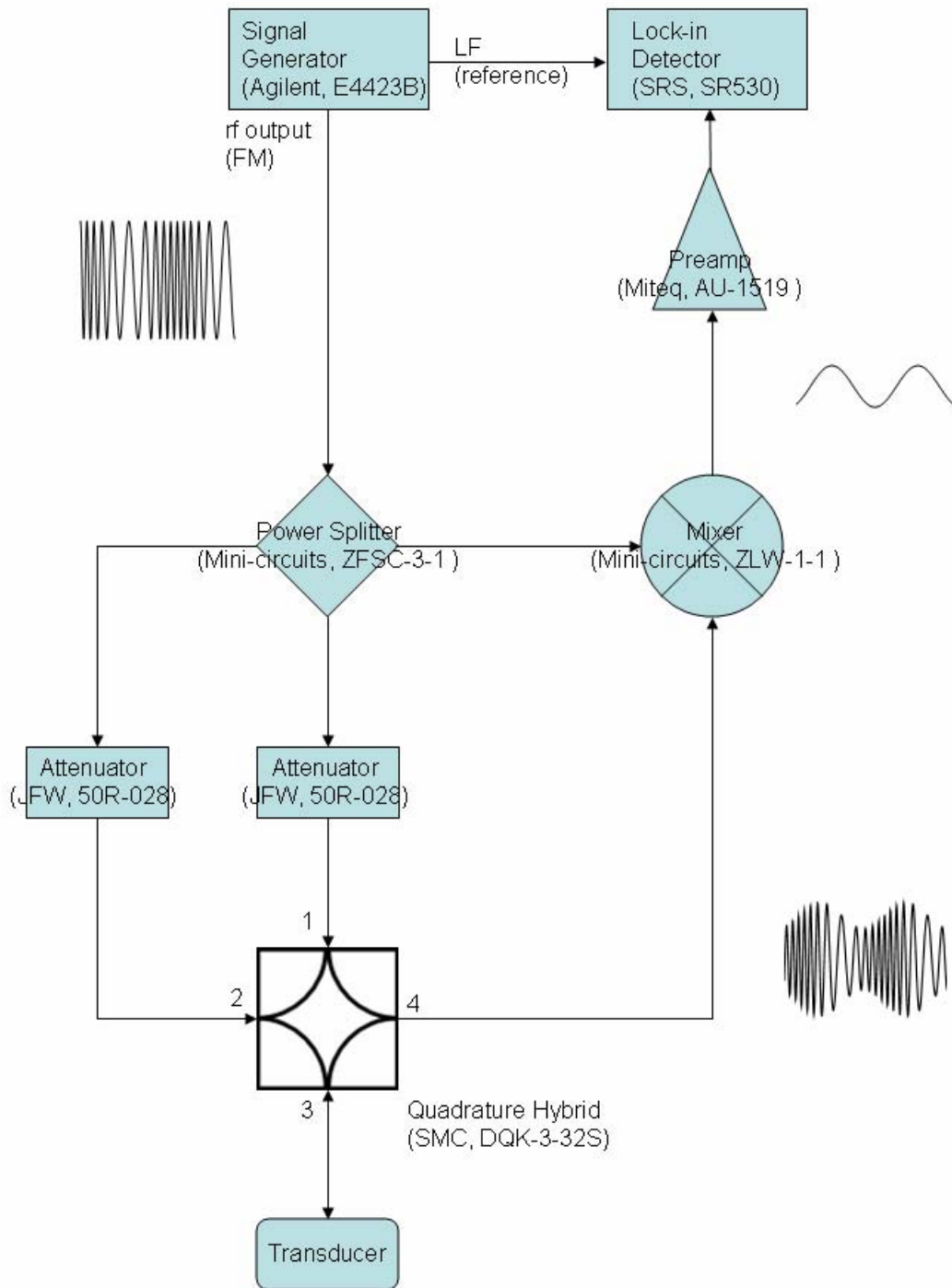


Figure 2-5. Schematic diagram of the continuous wave spectrometer (modified from Lee's design [Lee97]). The arrows represent flow of signal. The signal shape at each step is shown next to the arrow. The model number of each component is specified in parenthesis.

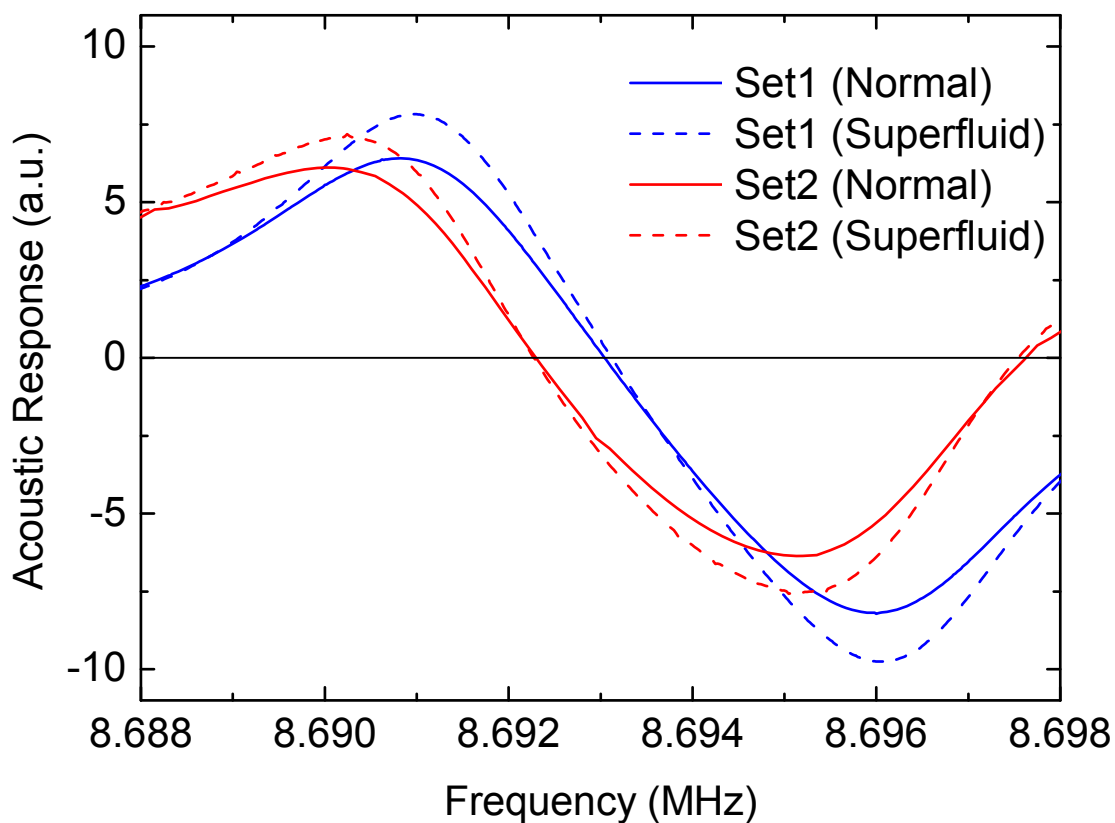


Figure 2-6. Frequency sweep for two different spectrometer settings at 28.4 bars and 3 T. The dashed lines are measured at low temperature which is deep in the superfluid and the solid lines are acquired in the normal fluid phase. Set1 and Set2 represent different attenuation setting in cw spectrometer. In Set2 (red traces), we could reduce the asymmetry in the maximum and minimum. Set2 also shifts the crossing point in the normal and superfluid traces closer to zero.

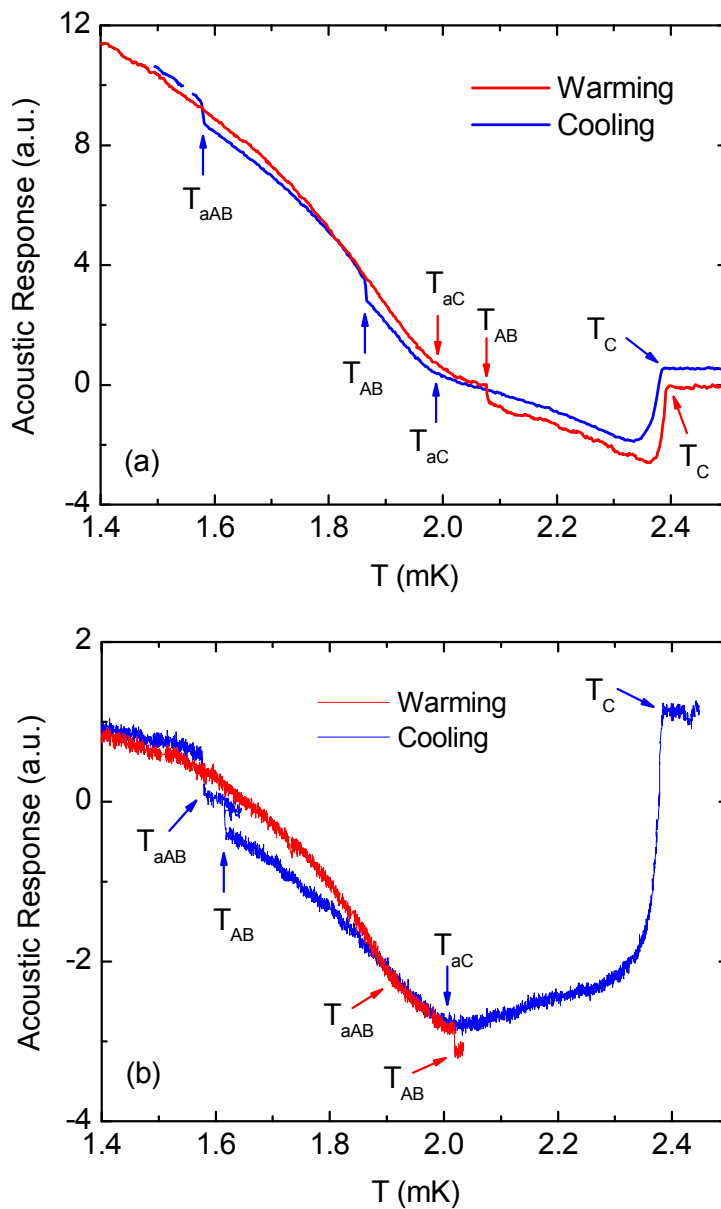


Figure 2-7. Zero field acoustic signals at 28.4 bars for different spectrometer settings as a function of temperature. Panel (b) presents data taken after fine tuning of the spectrometer to Set2 in Fig. 2-6. In Panel (a) the acoustic response at 1.4 mK is much larger than at  $T_C$ . In Panel (b) the acoustic responses at 1.4 mK and  $T_C$  are almost the same as at  $T_C$  and the changes in slope at  $T_{aC}$  and at  $T_{aAB}$  on warming are clearer, compared with those in Panel (a).

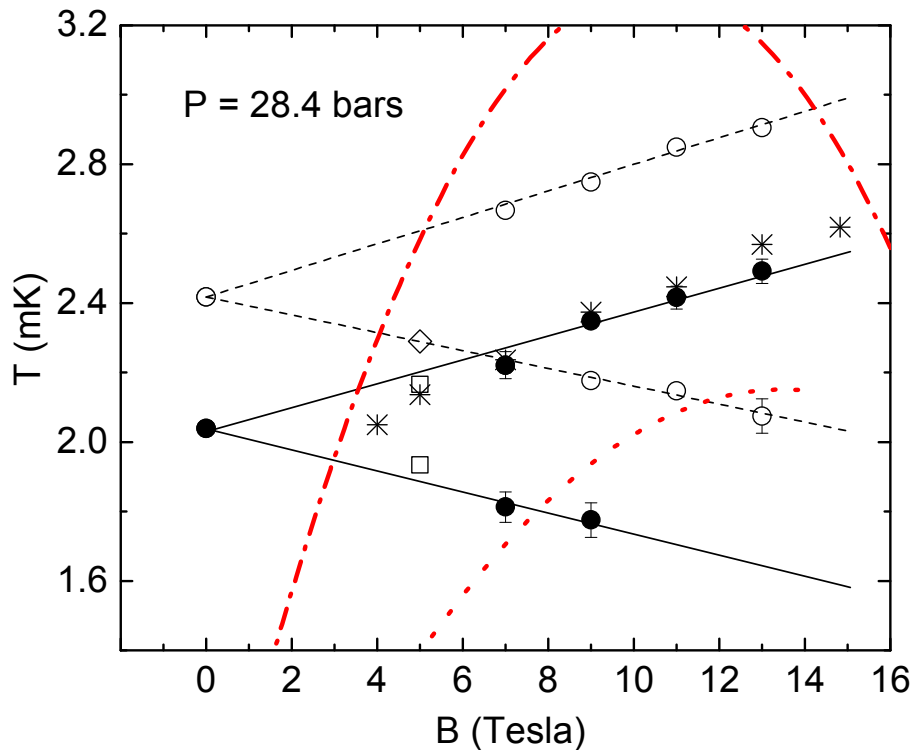


Figure 2-8. For high fields, we used the MPT calibration of Fukuyama's group [Yaw01]. Below 3.5 mK the calibration is given only for the high field phase, i.e. in the area under the dash-dotted line. The sensitivity of the MPT becomes too low to determine temperature well below the red dotted line. We used the width of bulk  $A_1$  phase as a fixed point for the temperature calibration and obtained transition temperatures in aerogel (closed circle). See detailed calibration procedure in the text.

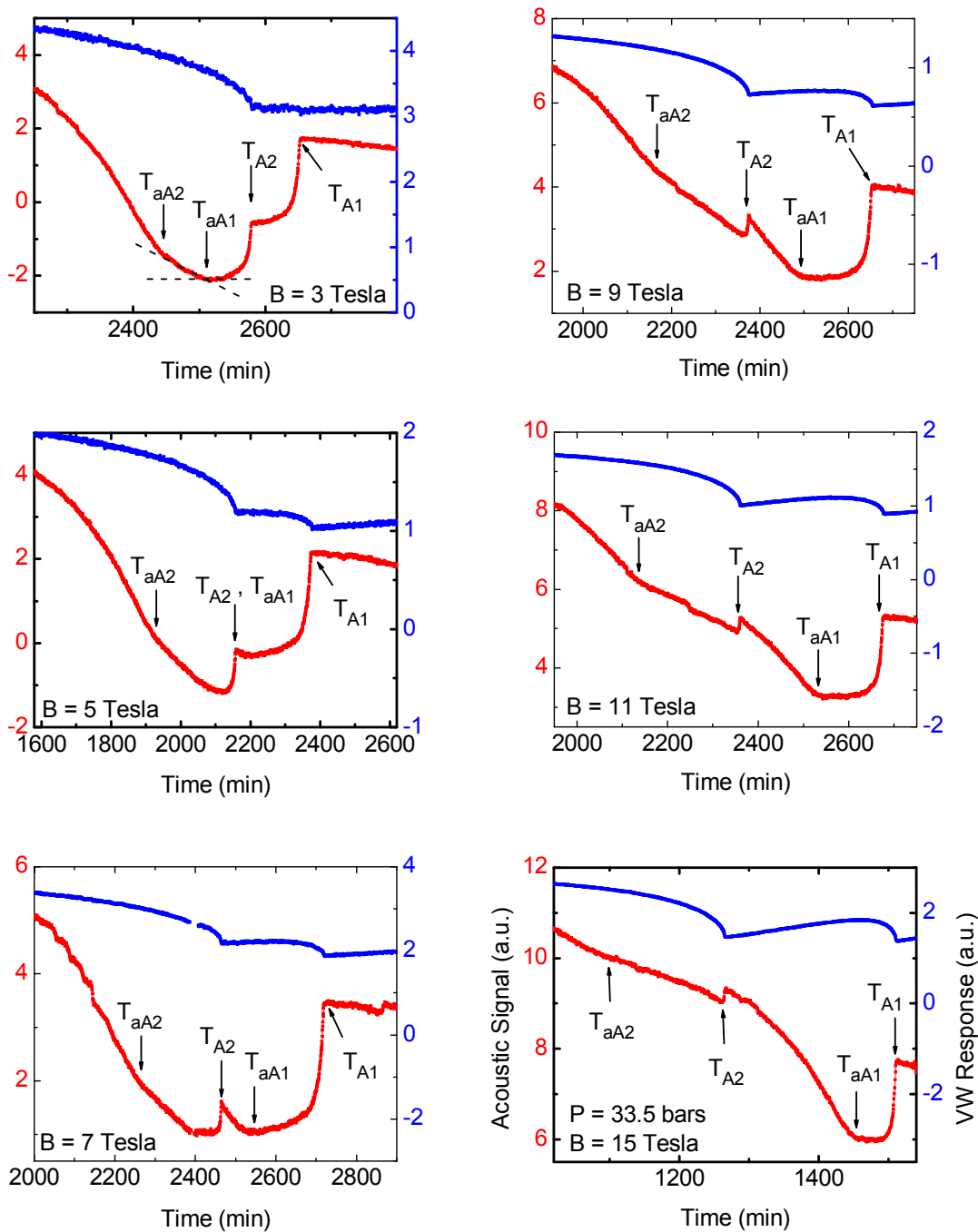


Figure 2-9. Acoustic traces for 3, 5, 7, 9, 11, and 15 T at 33.5 bars on warming. The sharp jumps in the VW trace are identified as the  $A_1$  and  $A_2$  transitions in the bulk liquid. The acoustic trace also shows two sharp features at the exactly same time positions.  $T_{aA1(2)}$  indicates the position of the  $A_{1(2)}$  transition in aerogel. The straight lines in the top-left panel are shown to illustrate the change in slopes at the transition.

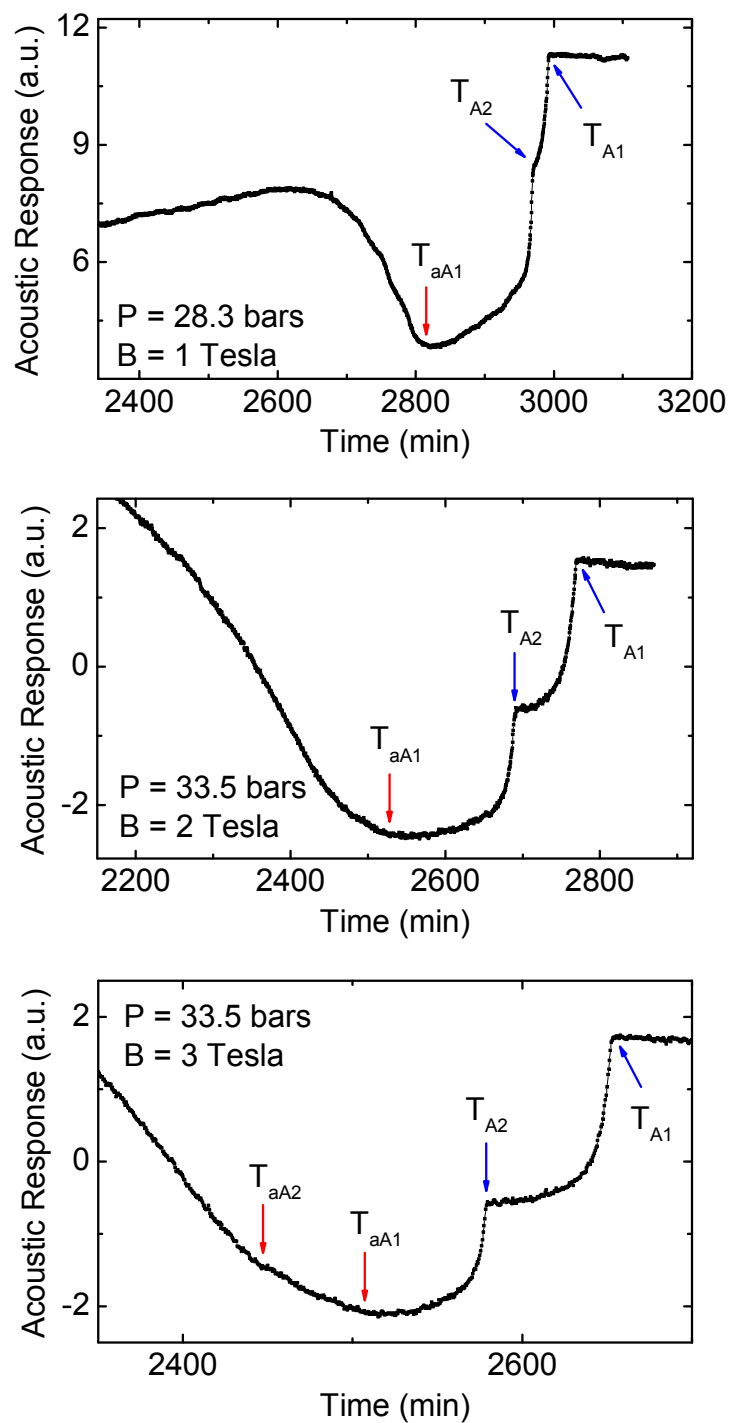


Figure 2-10. Acoustic traces for 1, 2 and 3 T. Pressures for each plot are labeled in the panels. Below 3 T, we were not able to resolve the double transition features in aerogel, while the features from the bulk can be traced at 1 T.

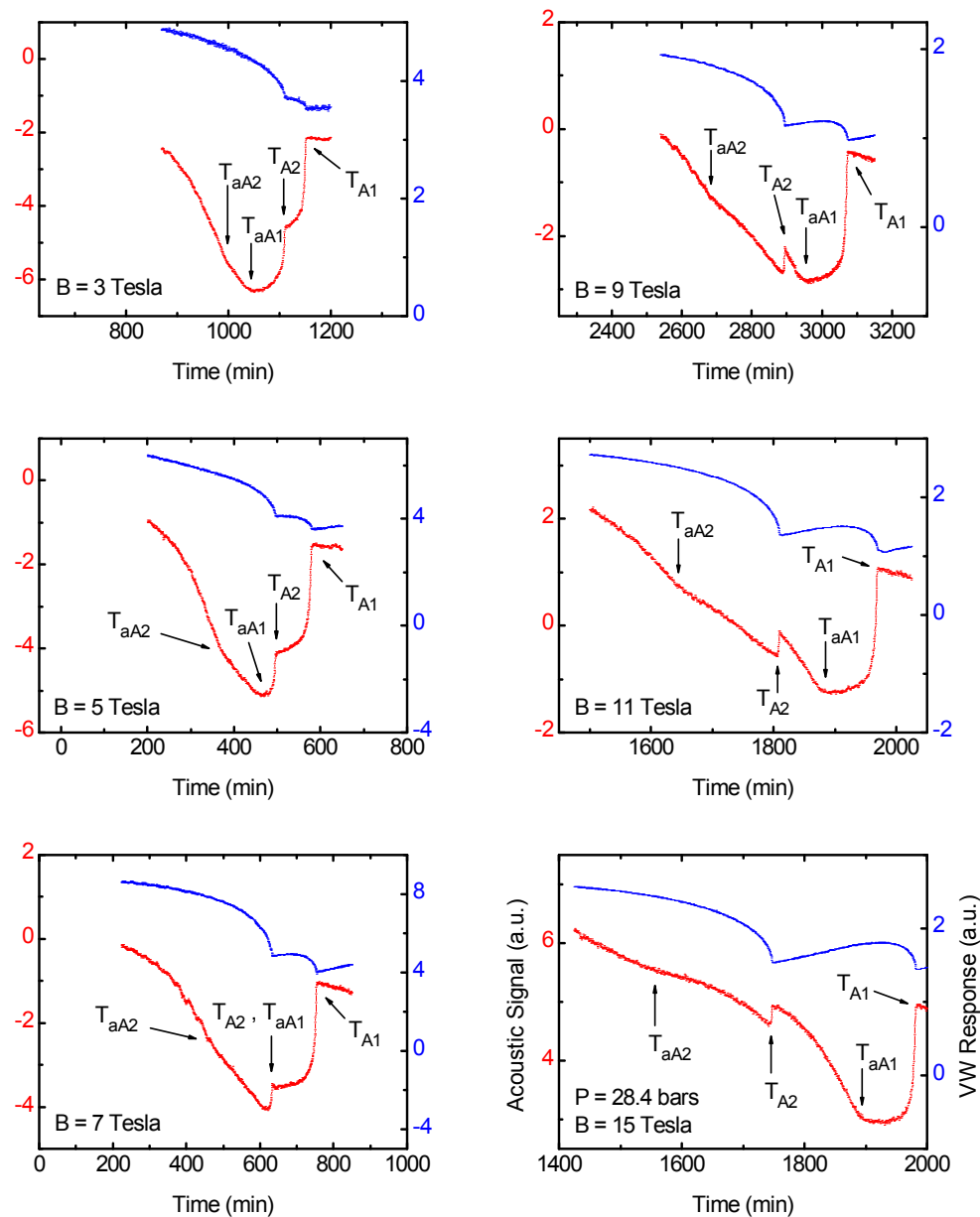


Figure 2-11. Acoustic traces for 3, 5, 7, 9, 11, and 15 T at 28.4 bars on warming. Each graph shows the acoustic (lower) trace along with that of the vibrating wire as a function of time. The sharp jumps in the vibrating wire trace are identified as the  $A_1$  and  $A_2$  transitions in the bulk liquid. The acoustic trace also shows two sharp features at the exactly same time position of  $A_{1(2)}$  transition in aerogel.

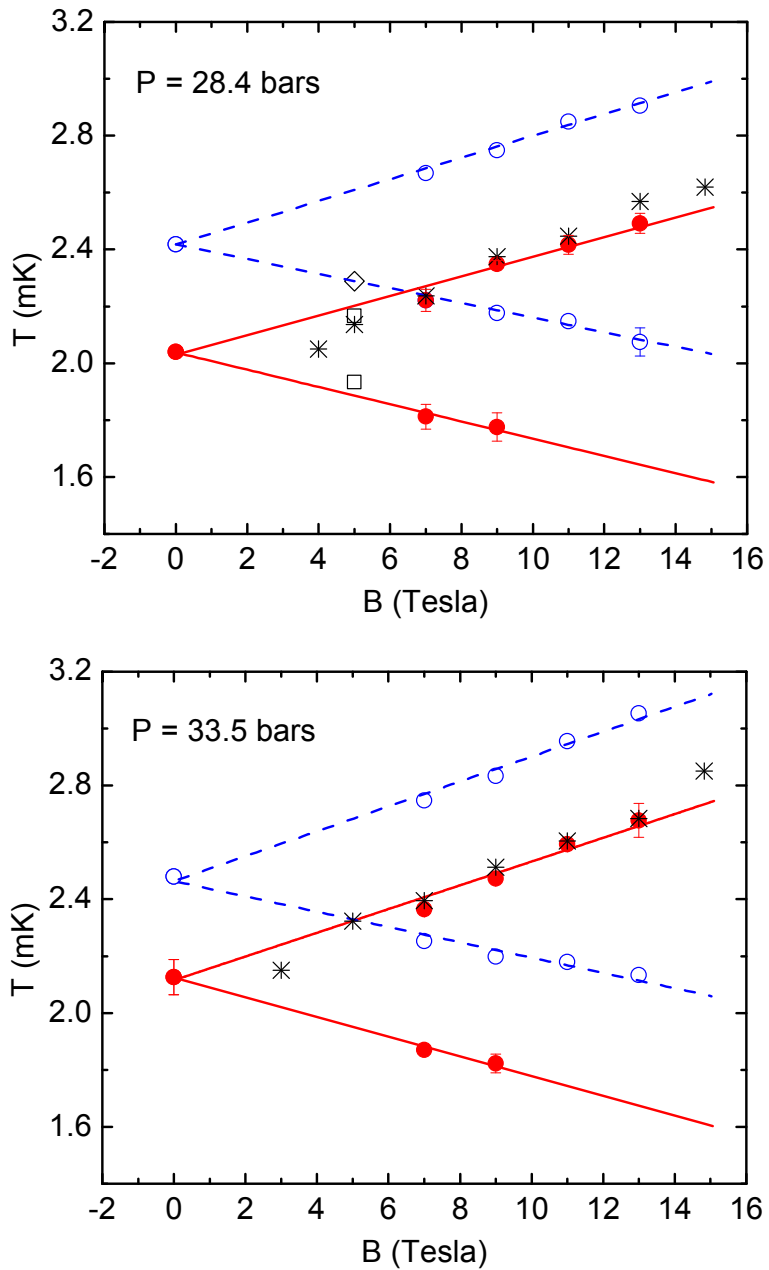


Figure 2-12. Transition temperatures vs. magnetic field for 28.4 and 33.5 bars. Open (solid) circles are for the bulk (aerogel) transitions determined by the two point calibration scheme. Open squares for 28.4 bars are obtained by the single point calibration method. Crosses are based on the constant warming rate. See the text for the temperature calibration procedures. The solid (dashed) lines are the results of linear fit for aerogel (bulk).

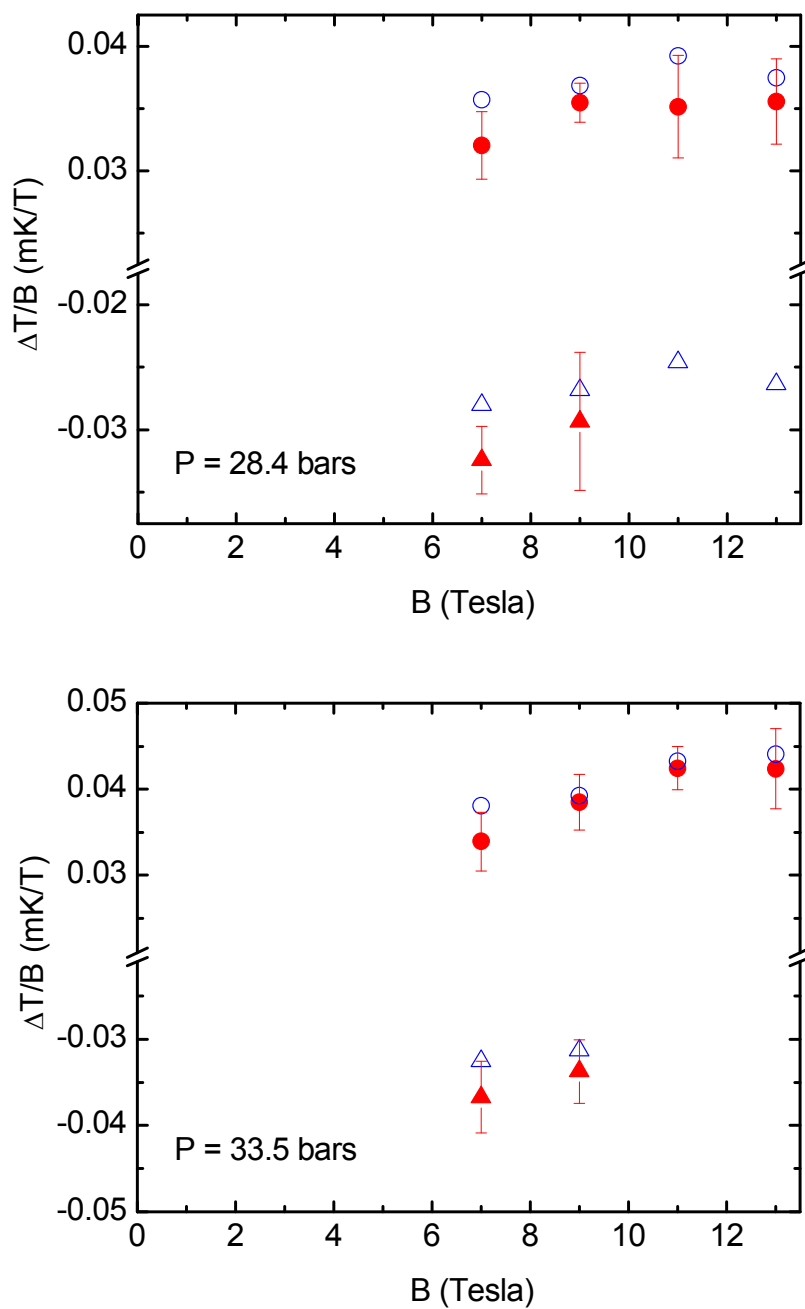


Figure 2-13. Degree of splitting for each individual transition vs. magnetic field.  $\Delta T$  is defined by  $\Delta T = T_{A_{1(2)}} - T_C$  where  $T_C$  is the zero field superfluid transition temperature.  $\Delta T$  is similarly defined for aerogel. For the  $A_{1(2)}$  transition,  $\Delta T$  is positive (negative). Filled (open) symbols are for the aerogel (bulk).

Table 2-1. Slopes  $T/B$  (mK/T) of the splitting for the  $A_1$  and  $A_2$  transitions in bulk and aerogel at 28.4 and 33.5 bars. The asymmetry ratios,  $r$  for bulk and  $r_a$  for aerogel, are also listed (see the text for a definition).

	$T_{A_1}/B$	$T_{A_2}/B$	$r$	$T_{aA_1}/B$	$T_{aA_2}/B$	$r_a$
28.4 (bars)	0.038	-0.026	1.46±0.06	0.034	-0.030	1.13±0.10
33.5 (bars)	0.043	-0.028	1.54±0.11	0.042	-0.035	1.20±0.14

CHAPTER 3  
THE  $A$  PHASE OF SUPERFLUID  $^3\text{He}$  IN 98% AEROGEL

**3.1 Overview**

Early NMR studies of  $^3\text{He}$ /aerogel show evidence of an equal spin pairing (ESP) state similar to the bulk  $A$  phase [Spr95] and a phase transition to a non-ESP state similar to the bulk  $B$  phase [Bar00b]. A large degree of supercooling was observed in this phase transition ( $A$ - $B$  transition), indicating the transition is first order. Further studies using acoustic techniques [Ger02a, Naz05] and an oscillating aerogel disc [Bru01] have confirmed the presence of the  $A$ - $B$  transition in the presence of low magnetic fields.

While the effects of impurity scattering on the second order superfluid transition have been elucidated by these early studies, experiments designed to determine the effects of disorder on the  $A$ - $B$  transition have been rather inconclusive [Ger02a, Bru01, Bar00b, Dmi03, Naz04a, Bau04a]. It is important to emphasize that the free energy difference between the  $A$  and  $B$  phases in bulk  $^3\text{He}$  is minute compared to the condensation energy [Leg90]. Moreover, both phases have identical intrinsic superfluid transition temperatures. The nature of highly competing phases separated by a first-order transition is at the heart of many intriguing phenomena such as the nucleation of the  $B$  phase in the metastable  $A$  phase environment [Leg90], the *profound* effect of magnetic fields on the  $A$ - $B$  transition [Pau74], and the subtle modification of the  $A$ - $B$  transition in restricted geometry [Li88]. We expect this transition to be extremely sensitive to the presence of aerogel and conjecture that even the low energy scale variation of the aerogel structure would have a significant influence on the  $A$ - $B$  transition.

A number of experiments have been performed with the purpose of systematically investigating the  $A$ - $B$  transition in aerogel [Ger02a, Bru01, Bar00b, Naz04a, Bau04a]. In experiments by the Northwestern group [Ger02a] using a shear acoustic impedance technique, a

significantly supercooled  $A$ - $B$  transition was seen while no signature of the  $A$ - $B$  transition on warming was identified. In the presence of magnetic fields, however, the equilibrium  $A$ - $B$  transitions were observed and the field dependence of the transition was found to be quadratic as in the bulk. However, no divergence in the coefficient of the quadratic term  $g(\beta)$  (see Eq. 2-9) was observed below the melting pressure. This result is in marked contrast with the bulk behavior that shows a strong divergence at the polycritical point (PCP) [Hah93]. The Northwestern group concluded that the strong-coupling effect is significantly reduced due to the impurity scattering and the PCP is absent in this system. Although this conclusion seems to contradict their observation of a supercooled  $A$ - $B$  transition even at zero field, other theoretical and experimental estimations of the strong-coupling effect in the same porosity aerogel [Cho04a, Bar02] seem to support their interpretation. On the other hand, the Cornell group [Naz04a] investigated the  $A$ - $B$  transition in 98% aerogel using a slow sound mode in the absence of a magnetic field. While the evidence of the supercooled  $A$ - $B$  transition was evident, no warming  $A$ - $B$  transition was observed. Nonetheless, they observed a partial conversion from  $B \rightarrow A$  phase only when the sample was warmed into the narrow band ( $\approx 25 \mu\text{K}$ ) of aerogel superfluid transition. Recently, the Stanford group conducted low field ( $H = 284 \text{ G}$ ) NMR measurements on 99.3% aerogel at 34 bars [Bau04b]. They found a window of about  $180 \mu\text{K}$  window below the superfluid transition where the  $A$  and  $B$  phases coexist on warming with a gradually increasing contribution of the  $A$  phase in the NMR spectrum (Fig.3-1).

For two sample pressures of 28.4 and 33.5 bars, we have observed the  $A$ - $B$  transition on warming in the absence of a magnetic field and have found evidence that the two phases coexist in a temperature window that is as wide as  $100 \mu\text{K}$ . This chapter provides a detailed description of our results and interpretations.

## 3.2 Experiments

We used the same experimental techniques that were described in Chapter 2. The sample cell experience a stray field of less than 10 G, which arises from the demagnetization magnet.

## 3.3 Results

The traces of acoustic signal taken near 28.4 bars in zero magnetic field are shown in Fig. 3-2 (a). The traces show the acoustic responses between 1.4 and 2.5 mK. The sharp jumps in the acoustic traces around 2.4 mK mark the bulk superfluid transition and the distinct slope changes are associated with the superfluid transitions in aerogel (see chapter 2). The signatures of the supercooled  $A$ - $B$  transition in the bulk and aerogel appear as small steps on the cooling traces. The identification of the step in the acoustic impedance as the  $A$ - $B$  transition has been established by a systematic experimental investigation of Gervais *et al* [Ger02a]. The cooling trace (blue) from the normal state of bulk reveals a well defined aerogel transition at 2.0 mK ( $T_{aA}$ ). The supercooled  $A$ - $B$  transitions from the bulk ( $T_{AB}$ ) and aerogel ( $T_{aAB}$ ) are clearly shown as consecutive steps at lower temperatures. After being cooled through both  $A$ - $B$  transitions, both clean and dirty liquids are in the  $B$  phase. On warming the trace follows the  $B$  phase and progressively merges into the  $A$  phase (cooling trace) around 1.9 mK. This subtle change in slope is the signature of the  $A$ - $B$  transition on warming. This was the first indication of a possible  $A$ - $B$  transition in aerogel on warming at zero field.

Figure 3-2 (b) at 33.5bar shows similar features, but the supercooled  $A$ - $B$  transitions in aerogel and bulk occur at almost the same temperature. On several occasions, we have observed that, when the liquid cooled from the normal phase, the supercooled  $A$ - $B$  transition in bulk and aerogel occur simultaneously. Furthermore, the supercooled bulk  $A$ - $B$  transition always precedes the aerogel transition, which might suggest that the aerogel  $A$ - $B$  transition is induced by the bulk

transition through proximity coupling. However, we have not carried out a systematic study on this issue.

In order to test our identification of this merging point as the warming  $B \rightarrow A$  transition in aerogel, we performed tracking experiments similar to those described by Gervais [Ger02a]. The sample liquid is slowly warmed from the aerogel  $B$  phase up to various points around the feature, and then cooled slowly to watch the acoustic trace for the signature of the supercooled  $A-B$  transition. During the turn around, the sample stays within  $30 \mu\text{K}$  from the highest temperature reached (hereafter referred to as the turn-around temperature) for about an hour. If the warming feature is indeed the  $A-B$  transition, there should be a supercooled signature on cooling only after warming through this feature. The color coded pairs of the traces in Fig. 3-3 (a) are the typical results of the tracking experiments for different turn-around temperatures at 28.4 bars. In the bottom (blue) cooling trace from the normal state, one can clearly see two supercooled  $A-B$  transition steps. The sharper step appearing at  $\approx 1.7 \text{ mK}$  corresponds to the bulk  $A-B$  transition. We find that the size of the step indicating the aerogel  $A-B$  transition depends on the turn-around temperature. We can make a direct comparison of each step size since the supercooled  $A-B$  transitions in aerogel occur within a very narrow temperature range,  $\approx 40 \mu\text{K}$ . Similar behavior was observed for 33.5 bars as shown in Fig. 3-3 (b).

From the data obtained in the tracking experiments, the relative size of the steps at the supercooled aerogel  $A-B$  transition, is plotted in Fig. 3-4 as a function of the turn-around temperature. The relative size is the ratio of the step size for each trace and the step size for the trace cooled down from normal fluid. For both pressures we see narrow temperature regions (shaded regions in the figure) where the size of the steps grows with the turn-around temperature until  $T_{aA}$  is reached. For  $T > T_{aA}$  no appreciable change in the step size is observed. This

suggests that only a portion of the liquid in aerogel undergoes the  $B \rightarrow A$  conversion on warming in that region. An inevitable conclusion is that the  $A$  and  $B$  phases coexist in that temperature window. A similar behavior has been observed in 99.3% porosity aerogel, although in the presence of a 284 G magnetic field [Bau04b]. Nazaretski *et al.* also found the coexistence of the  $A$  and  $B$  phases at zero field from low field sound measurements [Naz04b]. It is worthwhile to note that at 10 G, the equilibrium  $A$ -phase width in the bulk below the PCP is less than 1  $\mu\text{K}$ . A quadratic field dependence in the warming  $A$ - $B$  transition is observed in our study up to 2 kG (Fig. 3-5). The suppression of  $B$ -like phase is proportional to  $B^2$  as seen in the previous experiment by Gervais *et al.* [Ge02a]. Unfortunately, no information on the spatial distribution of the two phases can be extracted from our measurements.

### 3.4 Discussion

In Fig. 3-6, a composite low-temperature phase diagram of  $^3\text{He}$  in 98% aerogel is reproduced along with our  $A$ - $B$  transition temperatures. We plot the lowest temperatures where the  $B \rightarrow A$  conversion is first observed on warming. It is clear that the slope of the  $A$ - $B$  transition line in aerogel has the opposite sign of that in the bulk in the same pressure range. However, in a weak magnetic field, the slope of the bulk  $A$ - $B$  transition line changes its sign from positive ( $p < p_C$  where  $p_C$  represents the polycritical pressure) to negative ( $p > p_C$ ) (see the dotted line in Fig. 3-6)<sup>3</sup>. The first order transition line is governed by the Clausius-Clapeyron relation,

$$\left(\frac{dP}{dT}\right)_{AB} = \frac{s_B - s_A}{v_B - v_A} \quad (3-1)$$

where  $s$  and  $v$  represent molar entropy and volume for the  $A$  and  $B$  phase. Since  $s_B < s_A$ , the

---

<sup>3</sup> In the bulk, this behavior persists even in high fields up to the critical field. The sign crossover point gradually moves down to around 19 bars near the critical field. See Ref. Hah93.

change of the slope indicates the sign change in  $\Delta v = v_B - v_A$ . It is interesting to ponder why the strong coupling effects cause this sign change. We find no published results addressing this issue. Nonetheless, this observation and the fact that no divergence in  $g(\beta)$  has been observed in aerogel allow us to look at the phase diagram from a different point of view. It appears, that in effect, the  $P$ - $T$  phase diagram is shifted to higher pressures in the presence of aerogel rather than simply shifted horizontally in temperature. As a result, the PCP has moved to a physically inaccessible pressure as a liquid, thereby leaving only the weak coupling dominant portion in the phase diagram. If this interpretation is correct, then we have to face a perplexing question: How can we explain the existence of a finite region of the  $A$  phase at pressures below the PCP at  $B = 0$ ? We argue that anisotropic scattering from the aerogel structure is responsible for this effect. Although there is no successful quantitative theoretical account of the  $A$ - $B$  transition for  $p > p_C$ , the Ginzburg-Landau (GL) theory presents a quantitative picture for the  $A$ - $B$  transition in a small magnetic field  $B$ , (relative to the critical field) for  $p < p_C$ . Under these conditions, the quadratic suppression of the  $A$ - $B$  transition arises from a term in the GL free energy, namely

$$f_z = g_z B_\mu A_{\mu i} A_{\mu i}^* B_\nu, \quad (3-2)$$

where  $A_{\mu i}$  represents the order parameter of a superfluid state with spin ( $\mu$ ) and orbital ( $i$ ) indices [Vol90]. The main effect of this term is to produce a tiny splitting in  $T_C$  for the  $A$  and  $B$  phases.

In the GL limit, the free energy (relative to the normal state) of the  $A$  ( $B$ ) phase is

$f_{A(B)} = -\alpha^2 / 2\beta_{A(B)}$  and  $\beta_{A(B)}$  is the appropriate combination of  $\beta$  parameters that determine the fourth-order terms in the GL theory. For  $p < p_C$ , the  $B$  phase has lower free energy than the  $A$  phase ( $\beta_B < \beta_A$ ). However, when the two phases are highly competing, i.e.,  $\beta_A \approx \beta_B$ , even a

tiny splitting in the superfluid transition,  $\delta T_C = T_C^A - T_C^B (> 0)$  results in a substantial temperature region (much larger than  $\delta T_C$ ) where the  $A$  phase becomes stable over the  $B$  phase.

The simplified representation of the aerogel as a collection of homogeneous isotropic scattering centers is not sufficient to describe minute energy scale phenomena such as the  $A$ - $B$  transition. The strand-like structure introduces an anisotropic nature in the scattering, e.g.,  $p$ -wave scattering. This consideration requires an additional term in the GL free energy<sup>4</sup> [Thu98b, Fom04],

$$f_a = \alpha_1 a_i A_{\mu i} A_{\mu j} a_j, \quad (3-3)$$

where  $\hat{a}$  is a unit vector pointing in the direction of the aerogel strand. In other words, the aerogel strand produces a random field that couples to the orbital component of the order parameter. This random orbital field plays a role analogous to the magnetic field in spin space, thereby splitting the superfluid transition temperature. If the correlation length of the aerogel structure,  $\xi_a$  is longer than the length scale represented by  $\xi_0$ , the local anisotropy provides a net effect on the superfluid component, and  $f_a$  would give rise to the  $A$ - $B$  transition, even in the absence of a magnetic field. Detailed free energy considerations indicate that the anisotropy would favor the  $\hat{a} \perp \hat{l}$  configuration for the  $A$  phase [Rai77], where  $\hat{l}$  indicates the direction of the nodes in the gap. Using the expression for the coupling strength  $\alpha_1$  calculated in the quasiclassical theory [Thu98b], we find that  $f_a$  is comparable to  $f_z$  produced by a magnetic field  $B_e = \sqrt{\alpha_1 / g_z} \approx (T_C / \gamma \hbar) \sqrt{\xi_0 / \ell} \sim 1$  kG, where  $\gamma$  is the gyromagnetic ratio of  $^3\text{He}$  and  $\ell$  is the mean free path presented by the impurity scattering off the aerogel strand. Since

---

<sup>4</sup> Private communication with J.A. Sauls.

$B_e \propto \sqrt{\delta\ell/\ell}$  [ $f_a \propto (\delta\ell/\ell)$ ], where  $\delta\ell/\ell$  represents the anisotropy in the mean free path, only a fraction of 1% anisotropy is sufficient to produce the observed  $A$  phase width. The inhomogeneity of the local anisotropy over length scales larger than  $\xi_0$  naturally results in the coexistence of the  $A$  and  $B$  phase.

A PCP where three phases merge, as in the case of superfluid  $^3\text{He}$ , should have at least one first order branch [Fom04, Yip91]. When this branch separates two highly competing phases with distinct symmetry, the PCP is not robust against the presence of disorder. In general, the coupling of disorder to the distinct order parameters will produce different free energy contributions for each phase. Consequently, a strong influence on the PCP is expected under these circumstances [Aoy05]. It is possible that the PCP vanishes in response to disorder (as it does in response to a magnetic field) and a region of coexistence emerges. An experiment on  $^3\text{He}$ - $^4\text{He}$  mixtures in high porosity aerogel reported a similar disappearance of the PCP [Kim93]. Strikingly similar phenomena have also been observed in mixed-valent manganites where the structural disorder introduced by chemical pressure produces the coexistence of two highly competing phases (charge ordered and ferromagnetic phases) separated by a first-order transition [Dag01, Zha02]. A growing body of evidence suggests that the coexistence of the two phases is of fundamental importance in understanding the unusual colossal magnetoresistance in that material.

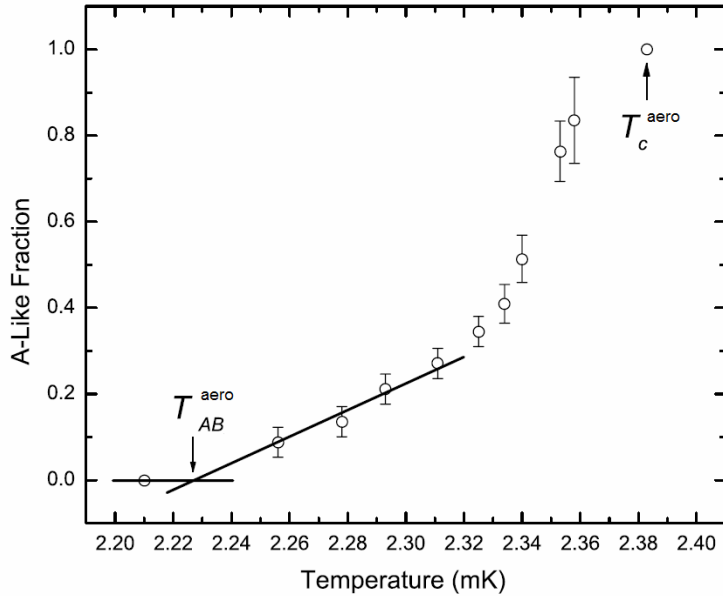
Considering the energy scales involved in the  $A$ - $B$  transition and anisotropy, it is not surprising to see a difference in the details of the  $A$ - $B$  transition in aerogel samples even with the same macroscopic porosity. However, it is important to understand the role of anisotropic scattering. We propose that the effect of anisotropic scattering can be investigated in a

systematic manner, at least in aerogel, by introducing controlled uniaxial stress, which would generate global anisotropy in addition to the local anisotropy.

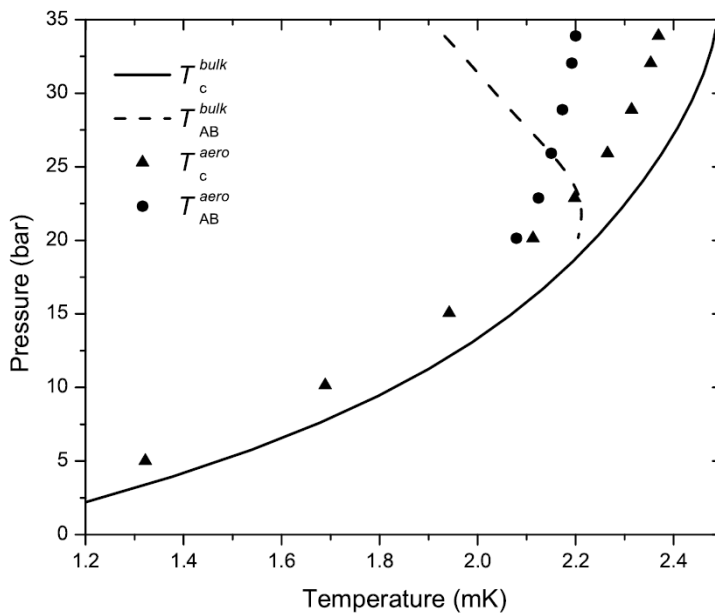
Aoyama and Ikeda have studied the  $A$ -like phase in the Ginzburg-Landau regime and found that the quasi-long-ranged ABM state has a free energy lower than the planar and the robust states [Aoy05]. Neglecting the inhomogeneous effect of aerogel on the order parameter, they parameterized the impurity effect only through the relaxation time and found that the impurity scattering weakens the strong coupling effect. The reduction of the strong coupling, which is consistent with our result in chapter 2, shrinks the width of ABM phase,  $T_{aC} - T_{aAB}$ . They also studied an inhomogeneity effect of the impurity scattering, especially with strong anisotropy, and found the anisotropy increases the width,  $T_{aC} - T_{aAB}$ . Their expectation on the anisotropy scattering is consistent with our arguments. They interpreted the existence of the  $A$ -like phase below the bulk PCP [Ger02a, Naz04b, Bau04b] as a lowering of the PCP, and this effect is explained qualitatively by taking into account the anisotropic scattering on the ABM state. The pressure of the PCP, which is different from that of bulk, was determined by the competition between two effects from the reduced  $\tau$  and the anisotropy scattering. Inspired by our suggestion, Aoyama and Ikeda calculated the effect of global anisotropy induced in uniaxially deformed cylindrical aerogel of two distinct flavors, compressed and stretched along the symmetry axis [Aoy06]. For both cases, they found that the ABM state opens up for all pressures. Furthermore, in stretched aerogel, a sliver of a new phase, the polar phase is predicted to appear just below  $T_{aC}$ .

Recently, Pollanen *et al.* performed x-ray scattering experiments on the aerogel and found that a certain degree of anisotropy exists even in an undeformed aerogel sample and argued that the global anisotropy could be generated during the growth and drying stages [Pol06]. Now, P.

Bhupathi in our group is pursuing a transverse acoustic measurement on the superfluid  $^3\text{He}$  in compressed aerogel. He did cut a commercial 98% aerogel sample and put it on a transducer. The other side of the aerogel was pressed by a cap for 5% in length or just enough to hold the aerogel. With 5% uniaxial compression, both the supercooled and stabilized  $AB$  transitions in aerogel could be identified, but not in uncompressed aerogel. We suspect that rough surface of aerogel establishes large open space on the boundary to the transducer, except at some contact points. Because of the high attenuation of the transverse sound, the transducer measures the liquid property very near to its own surface and if the open space is dominant, the acoustic response will be the same as those from the bulk. It is important to measure the  $A$ -like phase for a sample without compression as a bench mark. For the next trial, aerogel will be grown on a transducer *in situ* by the Mulders' group at the University of Delaware.



(a)



(b)

Figure 3-1. The Stanford NMR measurement on superfluid  $^3\text{He}$  in 99.3% aerogel. (a) The fractions of A-like phase vs. temperatures. The superfluid  $^3\text{He}$  in 99.3% aerogel was warmed up from  $B$  phase at low temperature and was cooled down at certain temperature. The temperatures of data (open circle) represent those turning points. The fraction was determined from the weight of the NMR line for the A-like phase [Bau04a]. (b) The phase diagram of superfluid  $^3\text{He}$  in 99.3% aerogel at 28.4 mT [Bau04b]. The closed circles represent the AB transition on warming. Reprinted figure with permission from J.E. Baumgardner, Y. Lee, D.D. Osheroff, L.W. Hrubesh, and J.F. Poco, Phys. Rev. Lett. **93**, 055301 (2004)] and [J.E. Baumgardner and D.D. Osheroff, Phys. Rev. Lett. **93**, 155301 (2004)]. Copyright (2004) by the American Physical Society.

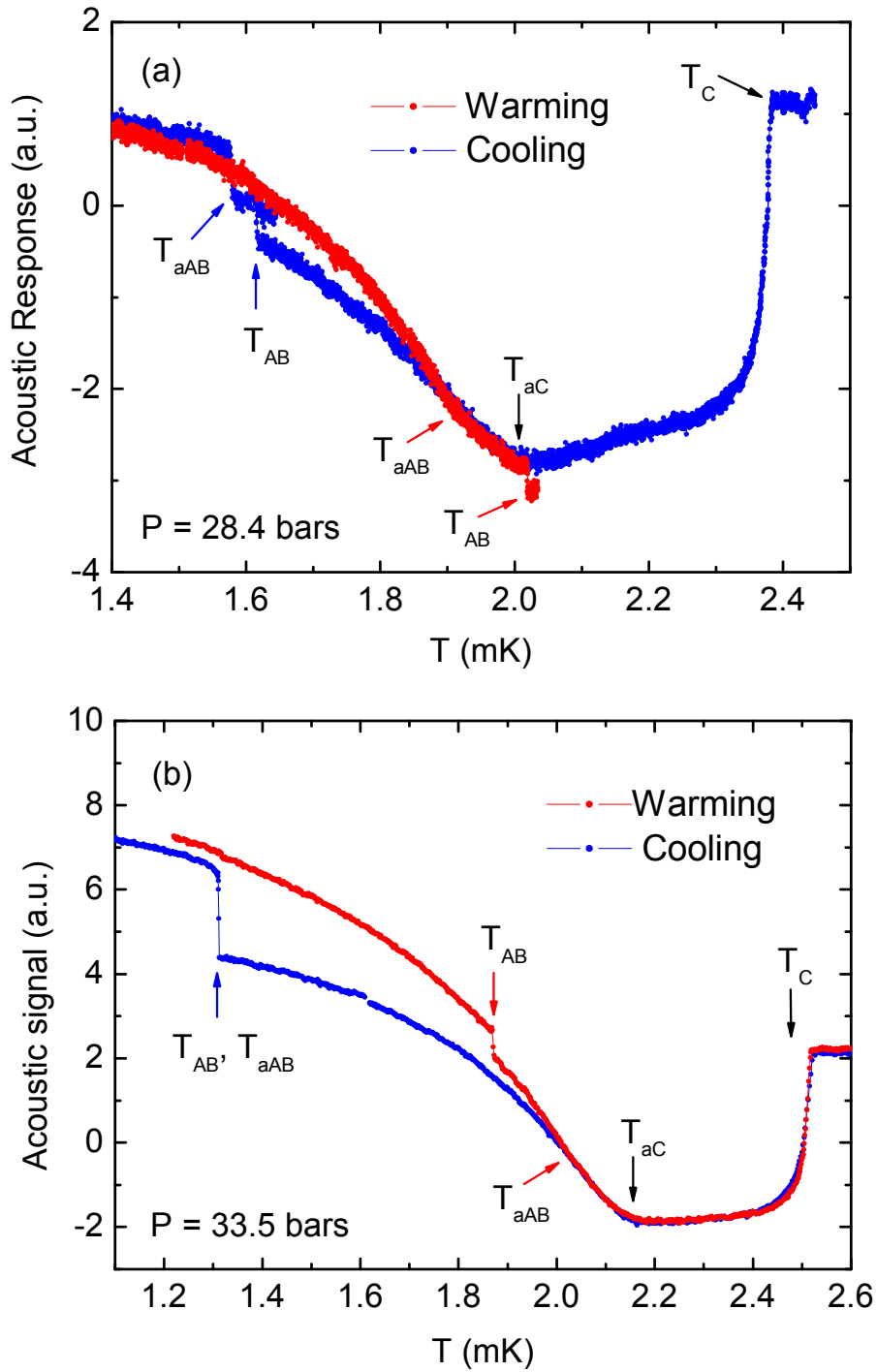


Figure 3-2. Cooling (blue) and warming (red) traces taken at 28.4 bars (a) and 33.5 bars (b). The signatures of the aerogel superfluid transitions and the aerogel  $A-B$  transitions are labeled as  $T_{aA}$  and  $T_{aAB}$ .

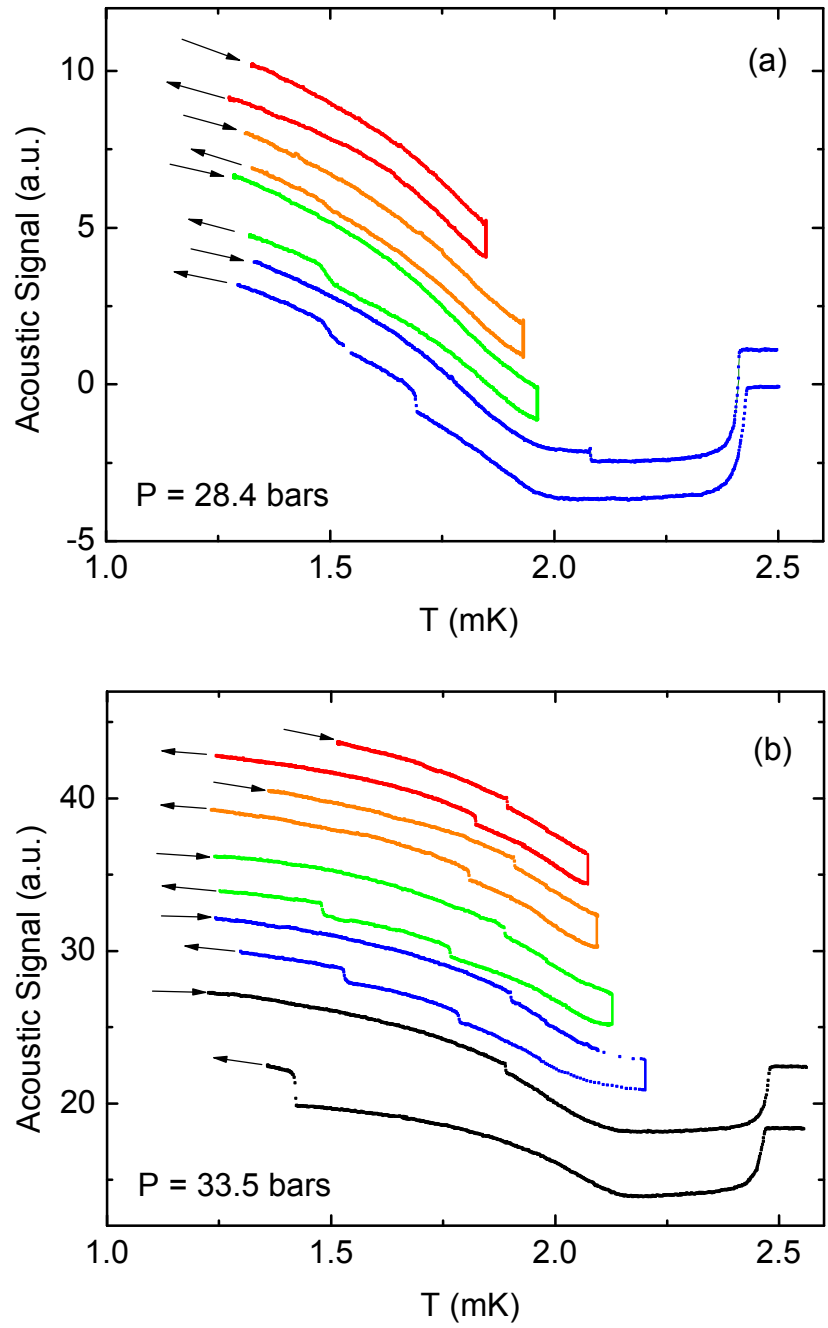


Figure 3-3. Acoustic traces of tracking experiments at 28.4 bars and 33.5 bars in zero magnetic field. Each pair of warming and subsequent cooling is color coded. The turn-around temperatures are indicated by the vertical line for each pair. For clarity the traces are shifted vertically and vertical lines are added manually. The arrows indicate the direction of temperature change in time.

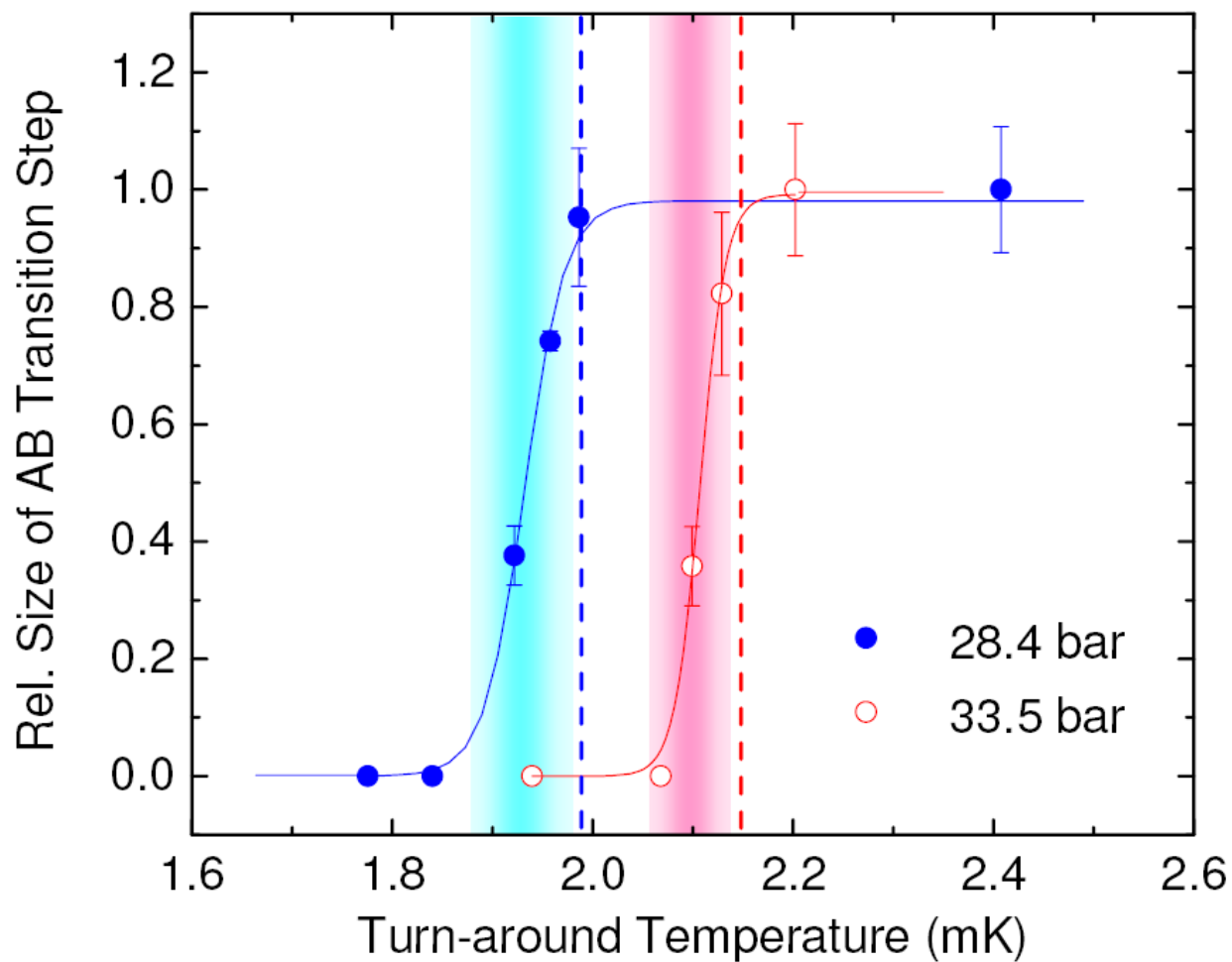


Figure 3-4. The relative size of the steps for the supercooled aerogel A-B transition is plotted as a function of the turn-around temperature for 28.4 and 33.5 bars. The relative size is the ratio of the step size for each trace and the step size for the trace cooled down from normal fluid. The lines going through the points are guides for eyes. The dashed vertical lines indicate the aerogel superfluid transition temperatures.

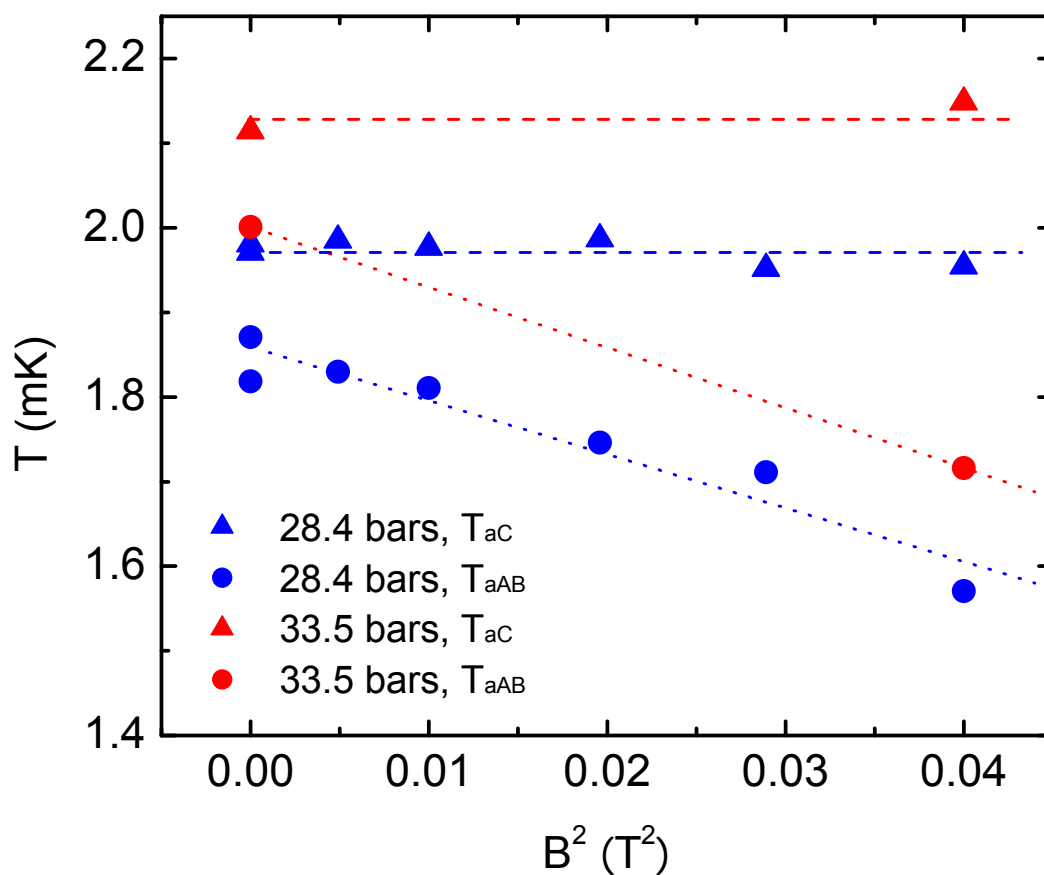


Figure 3-5. Field dependence of the warming  $A$ - $B$  transition in aerogel for 28.4 bars (blue circle) and 33.5 bars (red circle). Triangles represent  $T_{aC}$  for each pressure. The dashed lines show the average value of  $T_{aC}$  and the dotted lines are linear fits of  $T_{aAB}$  in each pressure.

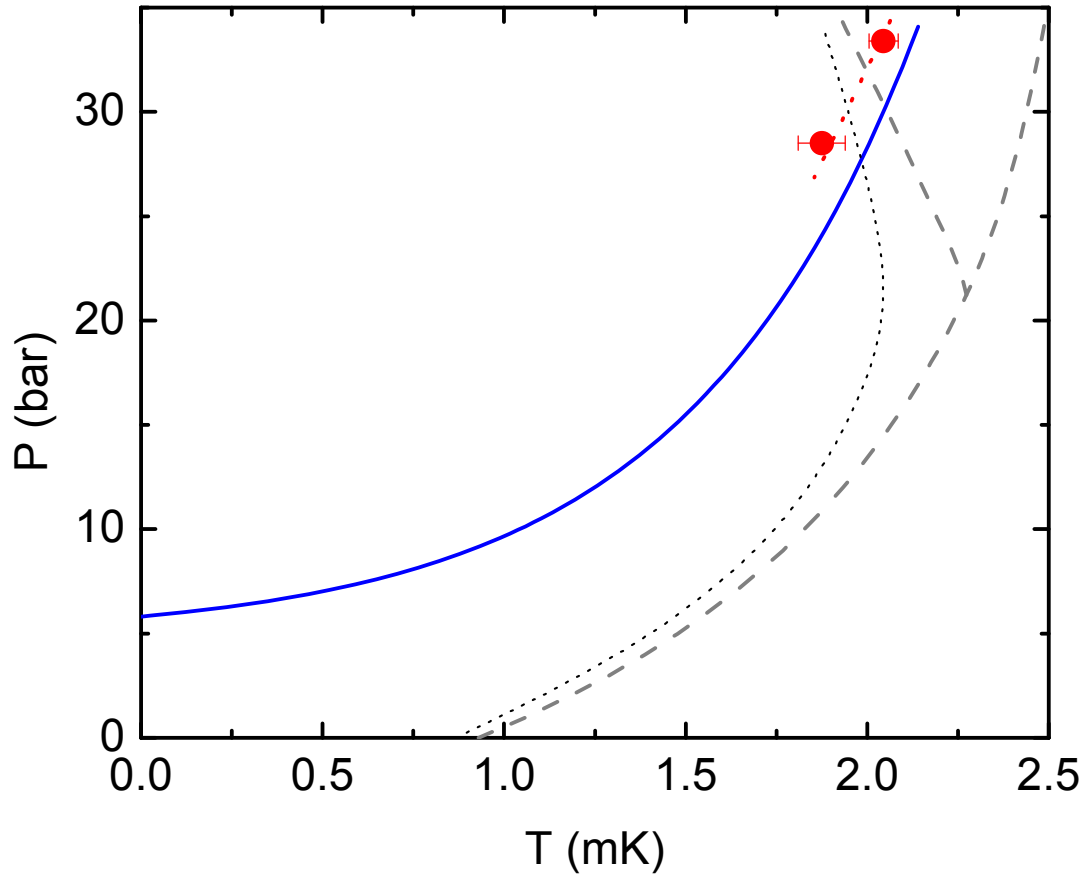


Figure 3-6. The zero field phase diagram of superfluid  $^3\text{He}$  in 98% aerogel along with that of the bulk (dashed lines) [Gre86]. The dotted line is the bulk A-B transition at 1.1 kG measured by Hahn [Hah93]. The aerogel superfluid transition line shown in blue is obtained by smoothing the results from Cornell and Northwestern groups [Mat97, Ger02a]. The two closed circles are the lowest temperatures where the  $B \rightarrow A$  conversion starts on warming, and the points are connected by a dashed line that is a guide for the eyes.

CHAPTER 4  
ATTENUATION OF LONGITUDINAL SOUND IN LIQUID  $^3\text{He}/98\%$  AEROGEL

**4.1 Overview**

High frequency ultrasound lends us a unique spectroscopic tool for investigating the superfluid phases of liquid  $^3\text{He}$  [Hal90, Vol90]. The frequency range of ultrasound conveniently matches with the superfluid gap, and the exotic symmetry of the superfluid phases allows various acoustic disturbances to couple to the superfluid component. The sharp pair-breaking edge occurs at  $\hbar\omega = 2\Delta(T)$ , where  $\omega$  is the ultrasound excitation frequency and  $\Delta(T)$  represents the temperature dependent superfluid gap. The coupling of ultrasound to many of the order parameter collective modes has been demonstrated by strong anomalies in sound attenuation and velocity [Hal90]. All of these rich ultrasound spectroscopic signatures could be elucidated because zero sound continues to propagate in the superfluid phase despite the presence of a gap at the Fermi energy.

In the presence of high porosity aerogel, the mean free path,  $\ell_a = v_F\tau_a$ , presented by the 98% aerogel is in the range of 100 - 200 nm as mentioned earlier. This length scale competes with the inelastic quasiparticle scattering length,  $\ell_i = v_F\tau_i$ , and becomes relevant only below  $\approx 10$  mK. Although impurity scattering has a marginal influence on the thermodynamic properties of the normal liquid, a significant change in the transport properties, specifically thermal conductivity, has been predicted at low temperatures [Ven00].

The pair-breaking mechanism from impurity scattering is known to induce impurity bound states inside the gap and to smooth the square root singularity at the gap edge [Buc81]. In the presence of severe pair-breaking, the system turns into a so-called gapless superconductor with the gap completely bridged by the impurity states. The impurity states have a broad influence on

the physical properties in the superfluid states. In superfluid  $^3\text{He}$ /aerogel, the gapless nature has been evidenced by recent thermal conductivity and heat capacity measurements [Fis03, Cho04b].

The acoustic properties of liquid  $^3\text{He}$  in aerogel are also affected by the presence of impurity scattering [Rai98, Gol99, Nom00, Ger01, Ich01, Hig03, Hig05, Hri01]. The classic first to zero sound crossover in the normal liquid was found to be effectively inhibited by the impurity scattering, maintaining  $\omega\tau < 1$ , where  $\tau = \tau_a\tau_i / (\tau_a + \tau_i)$  [Nom00]. It was also argued that an attempt to increase the excitation frequency would face an extremely high damping [Rai98]. Losing the luxury of having well defined zero sound modes at low temperatures has hampered investigations on the superfluid phases in aerogel using high frequency ultrasound. Although the high frequency transverse acoustic impedance technique [Lee99] has been successful in identifying various transition features [Ger02a, Cho04a, Vic05], only a few attempts have been made to investigate the superfluid gap structure using conventional high frequency longitudinal sound by Northwestern group [Nom00] and Bayreuth group [Hri01]. However, the Bayreuth experiment, which used a direct sound propagation technique, suffered from poor transducer response and observed no suppression of the superfluid transition temperature in aerogel. We suspect that there might be a thin layer of bulk liquid between the transducer and aerogel, which complicated the sound transmission through the liquid in aerogel. No published results are available from this work other than the aforementioned reference.

In 2000, Nomura *et al.* conducted high frequency sound (14.6 MHz) attenuation measurements of liquid  $^3\text{He}$  in 98% aerogel at 16 bars using an acoustic cavity technique [Nom00]. They found that the crossover from first to zero sound was effectively obscured by the impurity scattering of aerogel strands below  $\approx 10$  mK (Fig. 4-1). This behavior was rather easily understood in the framework of a simple viscoelastic model. However, this approach failed to

explain their results at higher temperatures, where the inelastic scattering between the quasi-particles is dominant. Furthermore, the sound attenuation in aerogel was found to saturate around 50 mK rather than follow a  $1/T^2$  dependence as observed in the bulk liquid. Higashitani *et al.* attempted to explain these results by incorporating a collision drag effect [Nom00, Hig03]. The Northwestern group employed a cw method using a short path length acoustic cavity, which is not adequate in determining the absolute sound velocity or, especially, the attenuation. This cw method relies on observing interference patterns developed in the cavity, and under conventional operation this pattern can be generated by sweeping the excitation frequency. However, with a high Q quartz transducer, this method is not feasible. Therefore, they had to sweep sample pressure to generate the necessary variations of the sound velocity, and this approach inevitably accompanies temperature drift. In addition to these difficulties, an auxiliary assumption had to be made to perform a two-parameter fit in attenuation and the reflection coefficient at the transducer surface<sup>5</sup>. In this work, we present our results of high frequency (9.5 MHz) longitudinal sound attenuation measurements using a pulsed ultrasound spectroscopic technique.

## 4.2 Experiments

Figure 4-2 (a) shows the schematic diagram of the experimental cell used for this study. The conceptual design of the cell is similar to the one used in the transverse acoustic impedance experiment described in previous chapters. The experimental cell consists of a pure silver base with  $9 \text{ m}^2$  of silver sinter and a coin silver enclosure. The ceiling of the enclosure forms a diaphragm, so the cell pressure can be monitored capacitively. Dimensions of each part can be

---

<sup>5</sup> They assumed that the attenuation at 25 bars and 0.6 mK is zero. The reflection coefficient was determined as 0.8, which satisfies the pressure dependence of attenuation at  $T_C$ . The attenuation of each pressure was calculated by the visco-elastic model. The visco-elastic model contains an aerogel mean free path as another parameter, which was taken as 240 nm in their work.

found in appendix B. Two matched longitudinal LiNbO<sub>3</sub> transducers (A and B as indicated in Fig. 4-2 (a)) are separated by a Macor spacer, which maintains a 3.05 ( $\pm 0.02$ ) mm gap between them. The aerogel sample was grown in the space confined by the transducers (1/4" diameter, 9.5 MHz resonance frequency) to ensure the contact between the transducer surface and the aerogel sample. This is an extremely important procedure since a thin layer of bulk liquid or an irregular contact between the transducer and aerogel would cause an unwanted reflection at the boundary of aerogel and liquids [Joh94a]. A 1 MHz AC-cut quartz transducer is placed right above the transducer A to monitor bulk response using a FM modulated cw method as described in chapter 2 (12.8 MHz, 500 Hz deviation frequency, 100 Hz modulation frequency). A piece of cigarette paper interrupts the path between the transducer A and the quartz transducer in order to spoil the back reflection. For transducer B, the irregular surface of silver sinter effectively diffuses unwanted sound propagation through the bulk liquid. The sample cell is thermally attached to the gold-plated copper flange welded to the top of the Cu nuclear demagnetization stage. An MPT and a Pt wire NMR thermometer (PLM-3, Instruments of Technology, Helsinki, Finland) are located right next to the sample cell on the same flange. The MPT was used for  $T > 1$  mK and the Pt NMR thermometer, calibrated against the MPT, was used for  $T < 1$  mK. Figure 4-3 shows temperature determined by MPT and Pt-NMR thermometer as a function of time for a complete cooling and warming cycle. The Pt-NMR thermometer is calibrated using an equation,  $T = M / (A_S - B)$ , where  $M$ ,  $A_S$ ,  $B$  are the normalized Curie constant, the magnetization determined by NMR and of the background signal, respectively.  $A_S$  was obtained by integrating the NMR free induction decay for a fixed time span. Two coefficients ( $M$  and  $B$ ) were treated as fitting parameters to match the temperature determined by the MPT. The green line in Fig. 4-3 was obtained in this way. As a result the thermal gradient between the MPT and the

Pt-NMR thermometer the green line does not match perfectly with the black line. However, by shifting about 5 minutes in Pt-NMR response one can find an excellent consistency between two thermometers (red line in Fig. 4-3). The typical warming and cooling rates were 3  $\mu\text{K}/\text{min}$ .

A commercial spectrometer, LIBRA/NMRKIT II (Tecmag Inc., Houston, TX) was employed for this study (Fig. 4-2 (b)). The same spectrometer was used for acoustic measurement on pure liquid  $^3\text{He}$  by Watson at UF [Mas00, Wat00, Wat03]. Typically, the output level from the NMRKIT II was set to the maximum of 13 dBm and was fed to the transmitter through a -20 dB attenuator. This input signal, after amplified to an appropriate level by a power amplifier, was used to excite transducer B. A 1  $\mu\text{s}$  pulse was generated by the transducer B (transmitter) and the response of the transducer A (receiver) was detected. The acoustic signal from the receiver was amplified by a low noise preamplifier, Miteq AU-1114, and was passed to NMRKIT II. The data acquisition began right after the end of the excitation pulse. The width of pulse, 1  $\mu\text{s}$ , is short enough to separate echoes in the low attenuation regime and wide enough in frequency to cover the resonance spectrum of the transducers. Although a matched pair of transducer was used, the slight difference in resonance spectra of two transducers determines the overall shape of the response (see next section). The typical setting of the LIBRA/NMRKIT-II can be found in appendix C. Origin scripts are used for data analysis and the details are in Appendix D. Each measurement presented in this work is the result of averaging 8 pulses responses generated in the phase alternating pulse sequence at 9.5 MHz of primary frequency. The data was taken every 5 minutes and the interval between pulses for the average was 4 seconds. All the measurements presented in this work were done at zero magnetic field.

### 4.3 Results

Figure 4-4 (a) shows the responses of transducer A at 34 bars in the time domain for selected temperatures. The primary response, which begins to rise around 8  $\mu$ s, grows below the aerogel superfluid transition ( $T_C = 2.09$  mK, indicated by an arrow in the figure). As temperature decreases, a train of echoes starts to emerge and four clear echoes are visible at the lowest temperature. The time interval between the primary response and the subsequent echo is twice of that between the excitation pulse and the primary response. For 14 bars, only the first echo is clear at the lowest temperature due to the higher attenuation (Fig 4-4 (b)). From the time of flight measurements, the speed of sound was determined to be 350 ( $\pm 10$ ) m/s at 34 bars, which is approximately 20% lower than in bulk. The velocity did not show temperature dependence within  $\pm 3\%$ . At 9.3 kHz, Golov *et al.* observed velocity enhancement of about 2% below  $T_C$  at 22 bars [Gol99]. The coupling between the normal component of the superfluid  $^3\text{He}$  and the mass of the elastic aerogel modifies the two-fluid hydrodynamic equation [Gol99]. Two longitudinal sound modes are found and the velocities of slow mode and fast mode ( $v_s, v_f$ ) are given as

$$c_f \sim c_1 / \sqrt{1 + \rho_a / \rho}, \quad (4-1)$$

$$c_s = c_a \sqrt{\rho_s \rho_a} / \rho. \quad (4-2)$$

The velocity of the fast mode calculated from the modified equation agrees well with our result (with a 5% discrepancy at most) (see Fig. 4-5). Due to the ringing of the transducers, the width of the received pulses is much broader than the excitation pulse (1  $\mu$ s). The location of the rising edge of the signal depended on the sample pressure, and the receiver signal disappeared when the sample cell was completely evacuated. These observations assure that the detected signal at the receiver is from the sound pulse passing through the aerogel/liquid. The step-like shape of the

responses, as shown in Fig. 4-6 (a), is caused by a slight mismatch in the spectra of the transducers. Figure 4-6 (b) shows a Fourier transformed transmitted signal (black circle) and the frequency profile of each transducer (blue and red lines). The frequency profile of each transducer was obtained using a duplexing scheme involving a directional coupler. The green line in Fig. 4-6 (b) is the result of simple multiplication of the two frequency profiles from the transmitter and receiver. As can be seen, this profile mimics the spectra of the receiver obtained by the conventional method used in this experiment. A weighted multiplication would improve the match and the difference in fine structures may be caused by duplexing the signal.

For most of our measurements, -7 dBm excitation pulses were used (+13 dBm excitation with -20 dB attenuator). Various levels of excitations ranging from 3 to -27 dBm were tested in order to check the linearity. Figure 4-7 (a) presents the signals for different excitations taken at 40 mK and 33 bars. The signal shows a mild distortion near the peak area at a 0 dBm excitation and the peak structure is severely distorted with a -3 dBm excitation due to saturation. However, the unsaturated part of the response scales linearly with the excitation. The linearity of the acoustic response was confirmed in the superfluid as well where the sound attenuation is lower. In Fig. 4-7 (b), the signal is normalized to its peak amplitude and the normalized signal for lower excitations fall on top of the signal from our typical setting (-20 dB). The signal shapes and the attenuations did not show any dependence on excitation within 5%, which means the sample and measurement scheme are in the linear regime. The warming traces with -7 dBm and -13 dBm excitations overlap well within the experimental error indicating that that heating effect caused by pulse transmission is negligible (Fig. 4-8).

In Fig. 4-6 (a), two normalized primary responses, taken at 0.4 mK and 2.5 mK and at 29 bars, are displayed for comparison. Despite the difference in their absolute sizes, the normalized

responses have an almost identical shape, which indicates that the spectra of the transducers remain the same throughout the measurements, and the change in the response is caused by the change in the acoustic properties of the medium. Therefore, the relative sound attenuation can be obtained by comparing the primary responses. We have used two different methods to extract the relative attenuation from the signal before being normalized: one was to use the peak value of the primary response and the other was to use the area under the curve by integrating the signal from the rising edge (8  $\mu\text{s}$  point in Fig. 4-6 (a)) to a fixed point in time (23  $\mu\text{s}$  point in Fig. 4-6 (a)). Both methods produce consistent results to within 7%, except at 10 bars (13%). The absolute attenuation at 0.4 mK and 29 bars was used as a reference point in converting the relative attenuation into the absolute attenuation. Absolute attenuations for the other temperatures were calculated by comparing the area of the primary response for each temperature to that for the standard absolute attenuation.

Because of an electronic glitch, probably from a slip of the relay switch in the NMRKIT II, the spectrometer sensitivity was not guaranteed to be the same for every run. Therefore, data were collected in one batch for each pressure at a fixed temperature, 9 mK. The relative attenuations for all other pressures were obtained by linking it to the attenuation at 9 mK and 29 bars. Only for 34 bars, the absolute attenuation was calculated independently from its own echoes. We decided the slope of the signal decay from two points, the peaks of the primary response and the first echo. To check the uncertainty of this method, we compared it to the slope determined by the peaks of the primary response, the first echo, and the second echo. The discrepancy of two methods gives a negligible difference on the standard absolute attenuation ( $\pm 0.08 \text{ cm}^{-1}$ ).

As shown in Fig. 4-9, the peaks of the primary response and the subsequent echoes exhibit a *bona fide* exponential decay. With the knowledge of the gap between the transducers, the absolute value of attenuation was determined. Due to the drastic acoustic impedance mismatch at the boundary between the transducer and the aerogel/<sup>3</sup>He sample, the echoes were assumed perfectly reflected at the interface<sup>6</sup>.

The normalized attenuations for 12 and 29 bars as a function of the reduced temperature are shown in Fig. 4-10 along with that of pure <sup>3</sup>He measured at 29 bars using 9.5 MHz sound excitation [Hri01]. There are three main contributions to the ultrasound attenuation in pure superfluid <sup>3</sup>He: (1) pair-breaking mechanism, (2) coupling to order parameter collective modes (OPCM), and (3) scattering of the thermal quasi-particles [Hal90]. All the features mentioned above have been extensively investigated theoretically and experimentally. At ~ 9.5 MHz, the contributions from (1) and (2) give rise to a strong attenuation peak as clearly shown in the figure. These salient features are completely missing in the aerogel, although the superfluid transition is conspicuously marked by the rounded decrease in attenuation. A similar behavior was observed by Nomura *et al.* [Nom00] and this behavior was interpreted as indirect evidence that the sound propagation remained hydrodynamic even in the superfluid phase [Hig05]. We have checked the primary responses in the normal liquid (13 mK at 29 bars) and the superfluid (1 mK at 34 bars) using higher harmonics of the transducers (up to 96 MHz). Only the 9.5 MHz excitation produced a recognizable response in the receiver, thereby confirming that the sound mode at 9.5 MHz remains hydrodynamic even in the superfluid phase. If the sound at 9.5 MHz was the zero sound, the attenuation would not show that much frequency dependence. The zero

---

<sup>6</sup> Using the composite density of <sup>3</sup>He/98% aerogel at 29 bars,  $\rho_c = 0.113 \text{ g/cm}^3$ , measured sound velocity, 330 m/s, and the known acoustic impedance value for LiNbO<sub>3</sub>,  $Z_t = 3.4 \times 10^6 \text{ g/s}\cdot\text{cm}^2$ , less than 1% loss is expected at the boundary.

sound regimes are still supposed to exist at high frequencies, but the attenuation of zero sound is expected to be too high for a quantitative measurement.

On cooling at 29 bars (filled circles in Fig. 4-10), our data show a sharp jump at 1.5 mK ( $T/T_C = 0.7$ ). This feature is the supercooled  $A \rightarrow B$  transition in aerogel. On warming, the sound attenuation follows the  $B$ -phase trace of cooling and then merges smoothly with the cooling trace of the  $A$ -phase around 1.8 mK ( $T/T_C \approx 0.9$ ) without showing a clear  $B \rightarrow A$  transition feature. This observation is consistent with the previous transverse acoustic impedance measurements described in chapter 3 [Vic05], which proved that this merging point is where the  $B \rightarrow A$  conversion begins. On cooling, the  $A$  to  $B$  transition is observed down to 14 bars (Fig. 4-11). Neither an  $A$ - $B$  transition feature nor hysteretic behavior was observed for 12 bars and below. Therefore, our attenuation results on warming are for the  $B$  phase in aerogel, except for the 200  $\mu$ K window right below the superfluid transition at high pressures. A broad shoulder feature around  $T/T_C \approx 0.6$  in the 29 bars trace progressively weakens as the pressure decreases, and this structure eventually disappears, as can be seen in the 12 bars trace. In Fig. 4-11, the  $T_{aC}$  and the  $T_{aAB}$  determined in this attenuation measurement are plotted along with previous results presented in chapter 3 (open circle). Our phase diagram is in good agreement with the ones mapped by different methods [Mat97, Ger02a, Hal04]. In the  $B$  phase with a clean isotropic gap, sound attenuation,  $\alpha \propto e^{-\Delta(T)/k_B T}$  (where  $k_B$  is the Boltzmann constant) is expected from the thermal quasi-particle contribution mentioned above. However, the temperature dependence of attenuation in aerogel is far from exponential and is not quenched down to  $T/T_C \approx 0.2$ . Furthermore, the sound attenuation approaches a fairly high value for both pressures at zero temperature, allowing a reasonable extrapolation.

The absolute attenuations on warming for several pressures are plotted in Fig. 4-12. The attenuation increases as pressure is reduced. The shoulder is less pronounced for low pressure and disappears below 21 bars completely. Zero temperature attenuations  $\alpha_0$  are estimated by assuming a quadratic temperature dependence (thin black line) for the low temperature region – we do not believe that this specific assumption affects our conclusion since our data already reached very close to zero temperature limit. The attenuation at lowest temperature decreases as the pressure is enhanced and it saturates above 25 bars. At the superfluid transition temperature, the attenuation of 8 bars is very close to that of 10 bars. Due to the high attenuation at this pressure, the signal from receiver was quite small but still we could detect the temperature dependence below the superfluid transition.

The normalized attenuations show the shoulder features disappear below 21 bars (Fig. 4-13(a)). Higashitani *et al.*'s calculations [Hig06] for several pressures are plotted with our data at 34 bars (Fig. 4-13(b)). Their calculations show more pronounced shoulder features and lower zero temperature attenuation for the same pressure. The absolute attenuation at the superfluid transition,  $\alpha_c$ , and the normalized zero temperature attenuation,  $\alpha_0/\alpha_c$  are given in Fig. 4-14(a). All values are taken from warming data except at 8 bars, and it is noteworthy that both  $\alpha_0$  and  $\alpha_c$  increase as the pressure is reduced. Although the dashed line following the normalized zero temperature attenuation is a guide for eye,  $\alpha_0/\alpha_c$  approaches 1 near 7 bars, which is close to the critical pressure below which no superfluid transition in 98% aerogel has been observed. The error bar is estimated from the differences of the attenuations calculated by the peak and the area of the primary response.

Absolute attenuation measurements allow quantitative analyses. Based on the theory of Higashitani *et al.* in which collision drag effect is incorporated, one can get the mean free length

in this system. As shown in Fig. 4-14(b), the whole pressure dependence of  $\alpha_c$  can be nicely fit with a single parameter for  $\ell = 120$  nm. Figure 4-15 shows the lower bounds of the zero energy density of states at  $T=0$  estimated from  $\alpha_0 / \alpha_c$  (details in next section).

For the normal liquid, the low temperature part of the attenuation is quite similar to those reported by Nomura *et al.* [Nom00]. However, our results show quite different behavior above 40 mK (Fig. 4-16 (a)). A broad minimum appears around  $T_M = 40$  mK for 29 bars and the attenuation continues to increase with temperature for  $T > T_M$ . Based on our measurements for three pressures, it seems that  $T_M$  decreases with the sample pressure. Interestingly, Normura *et al.* expected a similar rise in attenuation at high temperatures by considering the decoupling of liquid from aerogel, although their experimental results did not follow their prediction. In general, decoupling of liquid from the hosting porous medium occurs when the viscous penetration depth,  $\delta = \sqrt{2\eta / \rho\omega}$ , is of the order of the average pore size. This sloshing motion of the porous medium and viscous liquid provides an extra damping mechanism. Since the viscous penetration depth of  $^3\text{He}$  follows  $1/T$ , Nomura *et al.* argued that the condition for decoupling would be satisfied at a certain temperature. Furthermore, by invoking Biot's theory [Bio55a], they projected a  $T^2$  dependence of attenuation in the high temperature region. However, our high temperature data can be best fit to  $\sim T^{0.7}$  for all sample pressures that we studied. High temperature fits shown as dashed lines in Fig. 4-16 (a) present temperature dependences with powers of 0.64, 0.73 and 0.73 for 10, 21 and 29 bars, respectively. For the whole temperature range, the sound velocity remains constant within our experimental resolution.

#### 4.4 Discussion

Recently, Higashitani *et al.* [Hig05] calculated the hydrodynamic sound attenuation for this specific system based on the two-fluid model. Their calculation considered the aerogel motion generated by the collision drag effect [Ich01, Hig03]. In their theory, the total sound attenuation,  $\alpha_t$ , has two contributions,  $\alpha_t = \alpha_d + \alpha_h$ , where  $\alpha_d$  is the attenuation caused by the friction between the aerogel and the liquid, and  $\alpha_h$  is the hydrodynamic contribution.  $\alpha_d$  is proportional to the temperature dependent frictional relaxation time,  $\tau_f$ , whereas  $\alpha_h$  is proportional to the shear viscosity,  $\eta(T)$ . The detailed temperature dependence of the attenuation also requires knowledge of the superfluid density,  $\rho_s$ , in addition to the parameters described above. Despite the complexity of the model, their calculation provides a reasonably good account for our observation, such as the broad shoulder structure observed at 29 bars and the monotonic approach to finite attenuation near zero temperature [Hig05]. The moderate change of attenuation below  $T_C$  agrees with Higashitani *et al.*'s prediction based on the friction and the viscosity contribution (Fig. 4-13(b)). The relatively steep slope of Nomura *et al.* [Nom00] might be caused by their assumption that the attenuation at 25 bars and 0.6 mK is close to zero, which is about  $2 \text{ cm}^{-1}$  in our data. The shoulder of the temperature trace at high pressure can be explained by the combination of the continuously decaying viscosity contribution and the friction contribution which increases just below  $T_C$  for high pressure with reasonable aerogel mean free path. However, as pointed out earlier, the shoulder feature is much more pronounced in their calculation and the  $\alpha_0$  is lower than our projected values from the measurements. Their calculation is based on the homogeneous scattering model which tends to overestimate the

frictional damping but to underestimate the viscous damping<sup>7</sup>. The agreement between our experimental results and their calculation can be improved by incorporating inhomogeneous scattering which gives rise to further reduction of the average value of the order parameter. The extra reduction in the order parameter would be reflected in a larger viscosity and, accordingly, a larger  $\alpha_0$  is expected. In addition, an increased normal fluid fraction will weaken the frictional effect. It is also expected that the effect of anisotropic scattering would enter into play through various relaxation times. Detailed calculations including these effects are under consideration.

In particular, as the temperature approaches zero,  $\tau_f \rightarrow 0$  and  $\alpha_d \rightarrow 0$ . Consequently, the zero temperature attenuation is proportional to the finite shear viscosity, itself related to the zero-energy density of states,  $n(0)$ , by the relation,  $\eta(0)/\eta(T_C) = n^4(0)$  for the unitary limit<sup>8</sup> [Hig05]. Here,  $n(0)$  is the zero energy density of states at zero temperature, which is normalized to the density of states for normal liquid. Regardless of a specific theoretical model, the finite zero temperature attenuation reflects the existence of a finite zero-energy density of states induced by impurity scattering. Our results are in concert with the work of Fisher *et al.* [Fis03] in which finite thermal conductivity (mostly in the *A*-phase) in the zero temperature limit was observed [Sha03]. Indirect evidence for the presence of finite impurity states has also been suggested from the heat capacity measurement performed by a Northwestern group [Cho04b]. They inferred a linear temperature dependence in the heat capacity below  $\approx 1$  mK by analyzing the heat capacity jump at the aerogel transition and the heat capacity in the superfluid phase down to 1 mK. However,  $n(0)$ , estimated by the two different experimental techniques, shows significant discrepancies, especially in the pressure dependence. Because the frictional

---

<sup>7</sup> Private communication with Higashitani

<sup>8</sup> A power of 2 is theoretically predicted in the Born limit.

contribution disappears at  $T = 0$ , the attenuation ratio  $\alpha_0 / \alpha_C$  is the same as the ratio of the viscosity, if we ignore the frictional contribution at  $T_C$ . Therefore,  $\alpha_0 / \alpha_C$  in Fig. 4-14(a) provides the lower bound for the viscosity ratio. The lower bounds of  $n(0)$  are estimated from the viscosity ratio for the unitary and the Born scattering limits (Fig. 4-15). The density of states estimated from the specific heat measurements by the Northwestern group is about 0.6 for pressures from 10 to 30 bars [Cho04b].

The unique porous structure could be responsible for the increase of the attenuation at high temperature (Fig. 4-16 (a)). In other words, there is no well-defined pore size as aerogel has a completely different topology than other conventional porous materials. Furthermore, the nano-scale strand diameter is much smaller than any other length scale involved in the  $^3\text{He}$ /aerogel system up to  $\approx 70$  mK. In Fig. 4-16 (b), we show several relevant length scales estimated for 98% porosity aerogel: the effective mean free path,  $\ell$ , including aerogel scattering, the viscous penetration depth of  $^3\text{He}$ ,  $\delta$ , the average distance between aerogel strands,  $R = 20$  nm, and the diameter of aerogel strand,  $a = 3$  nm [Thu98a]. At all temperatures shown,  $\delta$  is larger than any other length scales. However, it is interesting to notice that the attenuation minimum ( $T_M$ ) occurs around the temperature where  $\ell$  crosses  $R$  and  $T_M$  moves to a higher temperature for lower pressure. For  $T < T_M$ ,  $\ell$  is larger than  $a$  and the hydrodynamic description for the motion between the aerogel and the liquid ceases to be valid. Therefore, Biot's theory which is basically a hydrodynamic theory may not be applicable. Only for  $T > T_M$ , the system enters into a regime where Biot's theory can be considered, particularly the intermediate frequency regime for most of our high temperature data, and  $\alpha$  is expected to be  $T$  independent. Currently, we do not have an explanation for the origin of the  $T^{0.7}$  dependence for  $T > T_M$ . However, the slip effect

[Tsi02] may give rise to a more temperature dependence owing to the enhanced velocity gradient of liquid at a solid surface. A distribution of pore sizes [Yam88, Pri93], the squirt mechanism [Dvo93], and/or the unique topology of the aerogel also need to be considered for a better understanding.

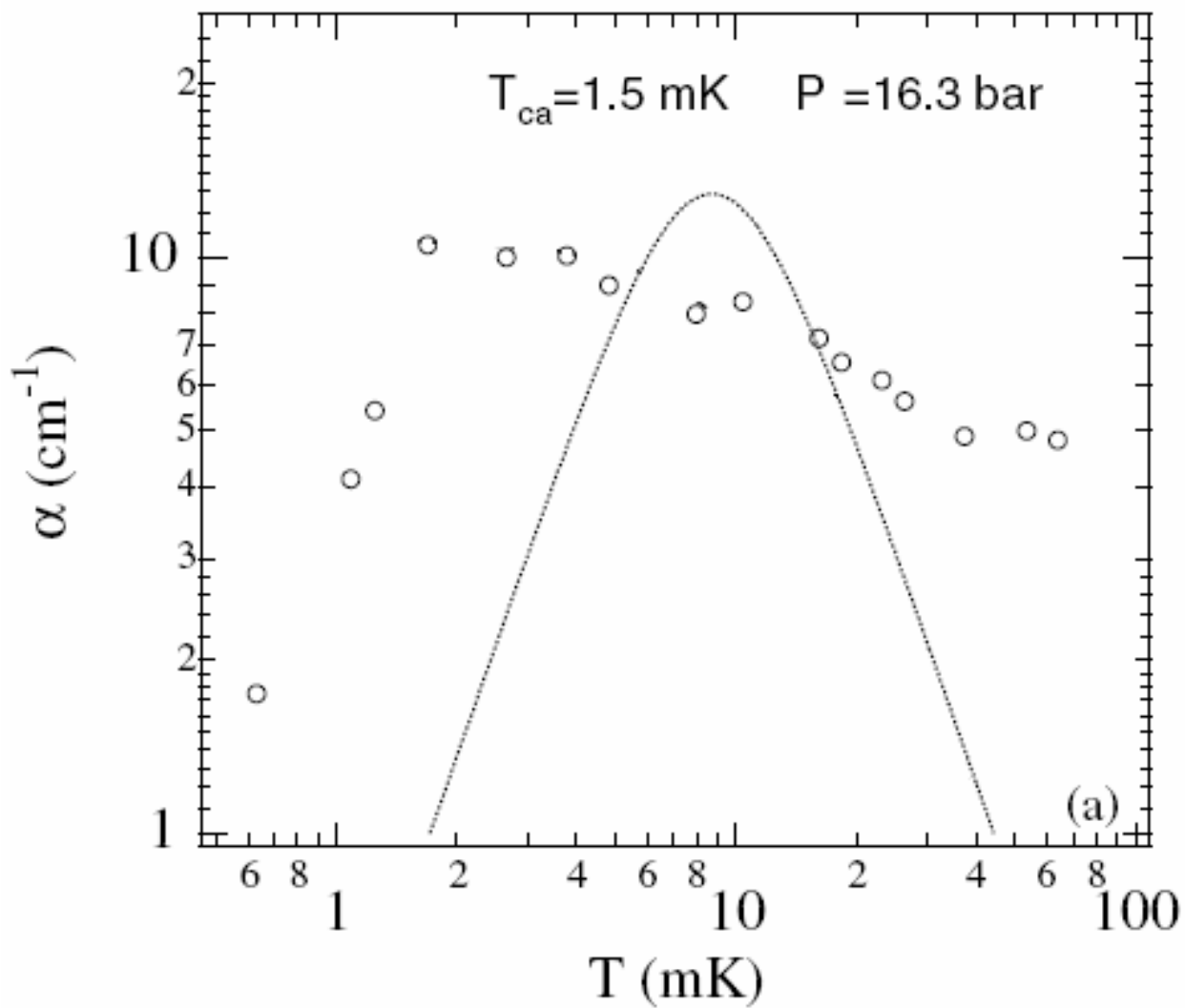
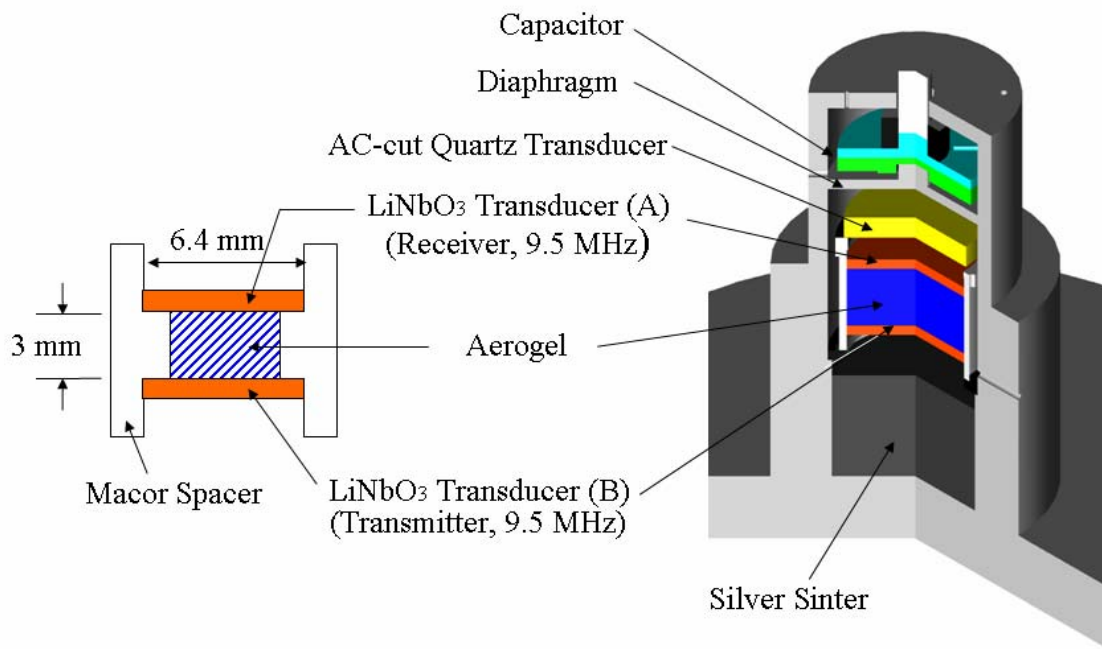
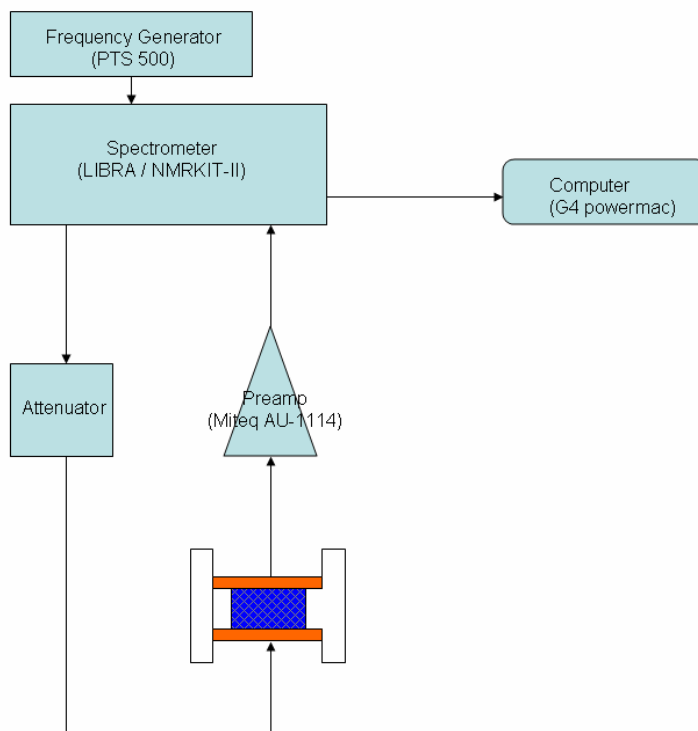


Figure 4-1. The attenuation of longitudinal sound in liquid  $^3\text{He}$ /aerogel at 16 bars for 15 MHz (circle) measured by Nomura *et al.* [Nom00]. The attenuation in bulk  $^3\text{He}$  (dotted line), given for comparison, shows the first to zero sound transition around 10 mK. Reprinted figure with permission from R. Nomura, G. Gervais, T.M. Haard, Y. Lee, N. Mulders, and W.P. Halperin, *Phys. Rev. Lett.* **85**, 4325 (2000). Copyright (2000) by the American Physical Society.



(a)



(b)

Figure 4-2. Schematic diagram of experimental setup. (a) Experimental cell (b) Pulse spectrometer.

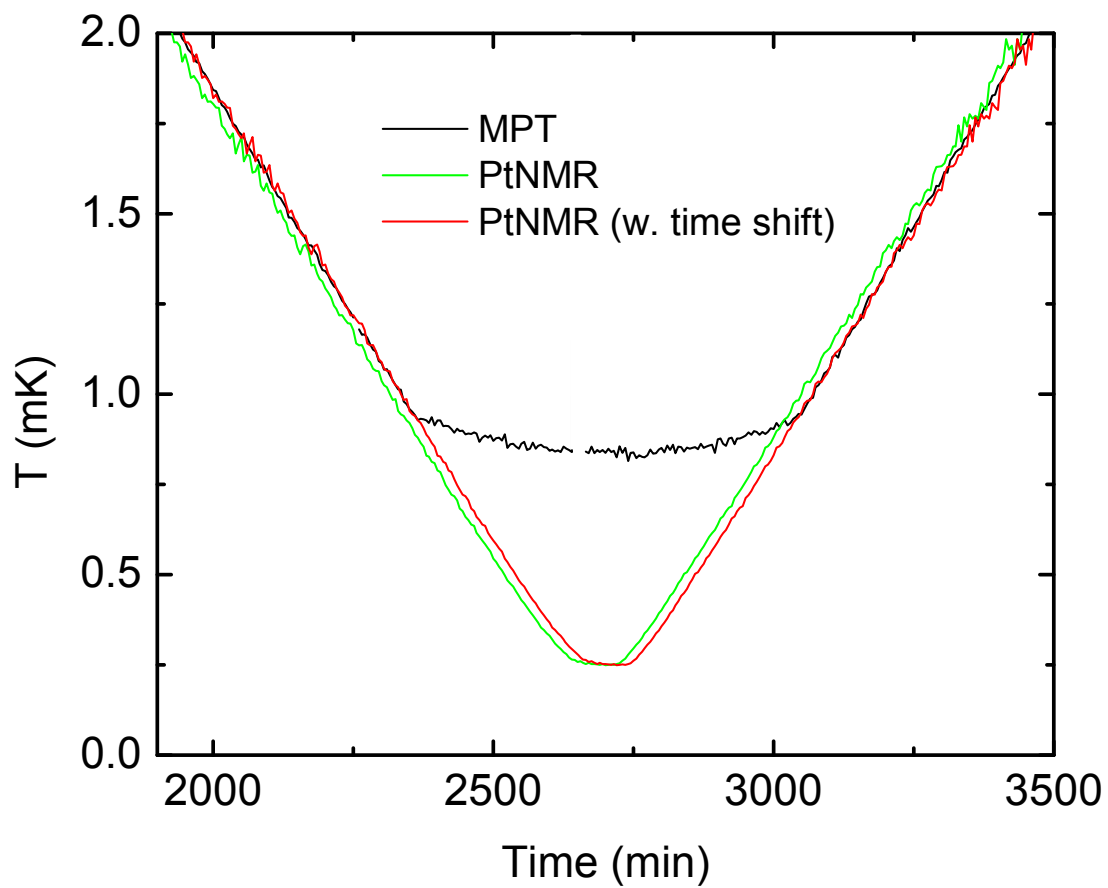


Figure 4-3. Temperature determined by MPT and Pt-NMR thermometer. With an appropriate shift in time, the Pt-NMR thermometer shows better match with MPT at high temperature (red line).

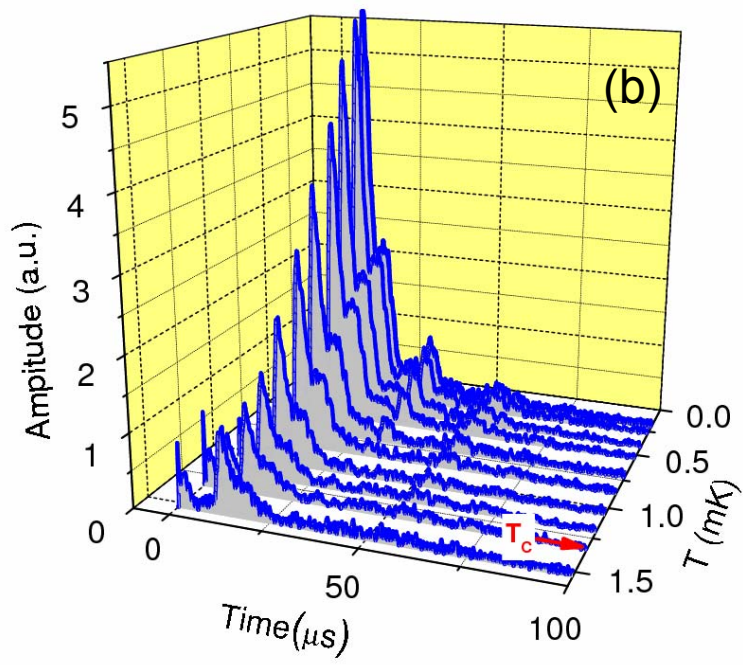
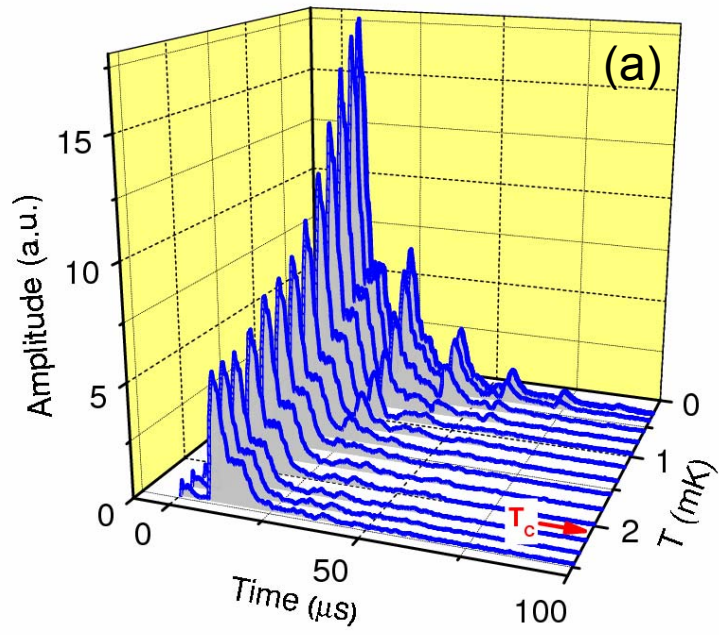


Figure 4-4. Evolution of receiver signals on warming. (a) For 34 bars, the superfluid transition is indicated by the arrow. Four echoes can be seen in the trace taken at the lowest temperature. (b) For 14 bars, only the first echo is observed at the lowest temperature.

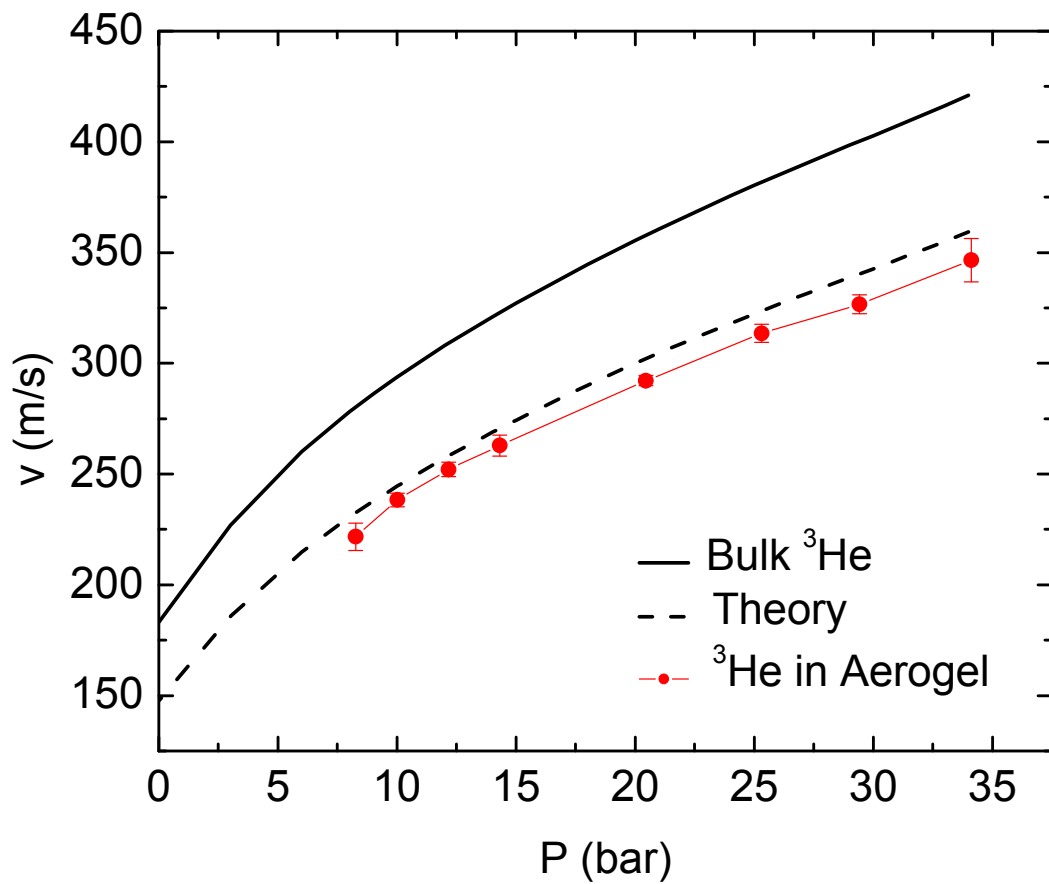
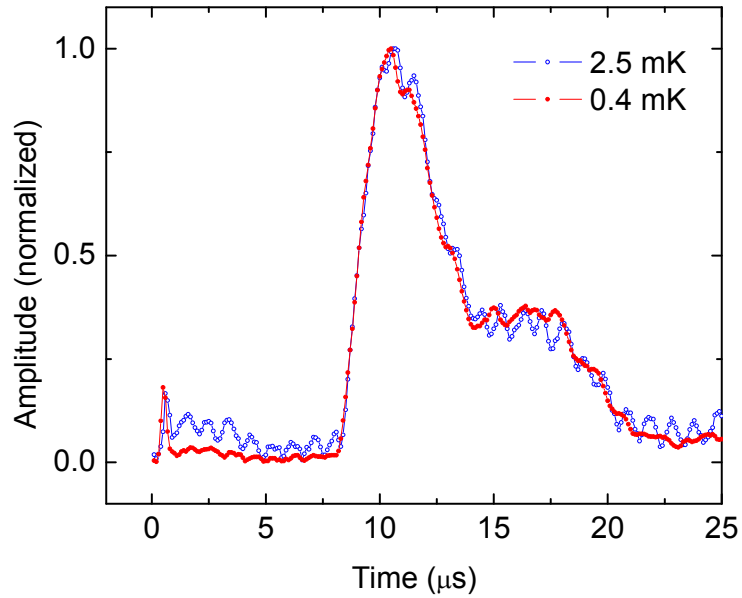
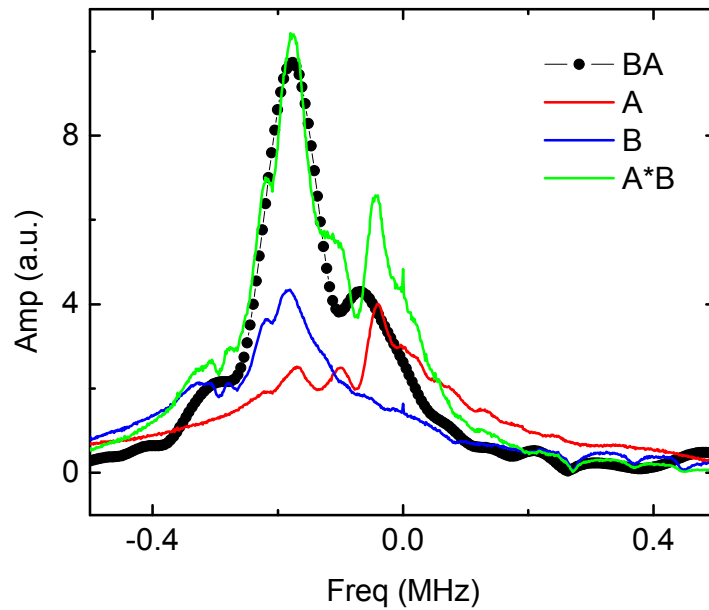


Figure 4-5. Velocity of bulk  $^3\text{He}$  [Hal90] and liquid  $^3\text{He}$  in aerogel at  $T_C$ . The dashed line is calculated from the two-fluid model modified by impurities (Eq. 4-1).

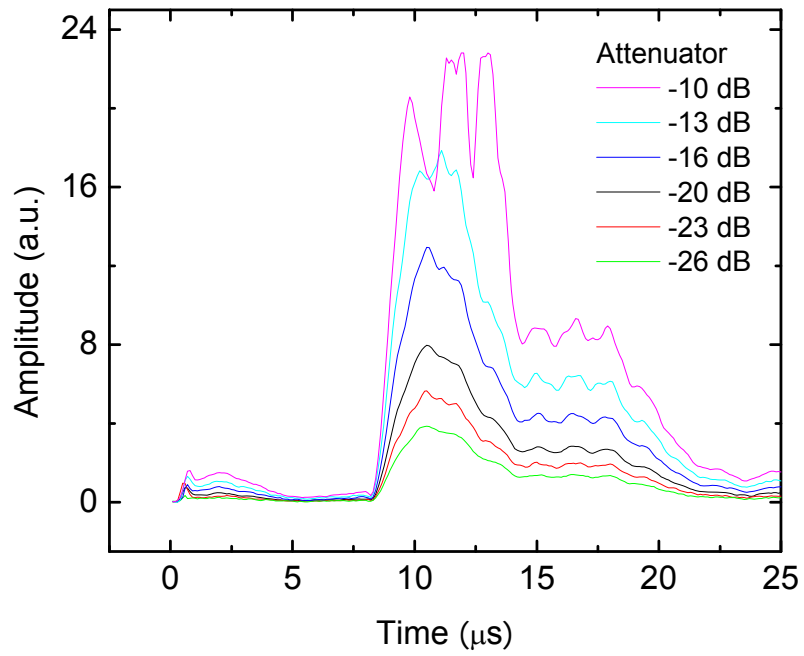


(a)

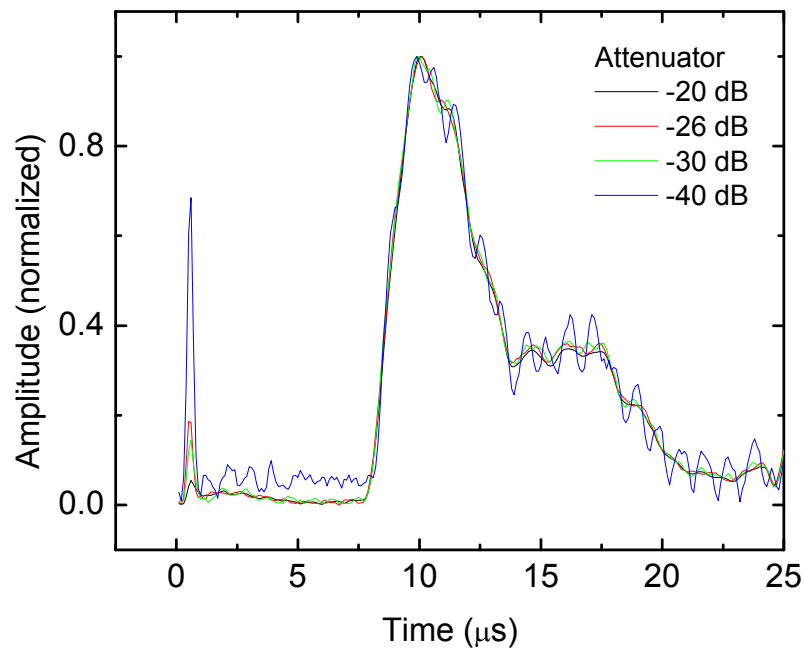


(b)

Figure 4-6. Signal from receiver. (a) Receiver signals normalized to its peak amplitude at 2.5 mK and 0.4 mK at 29 bars. (b) FFT of the transmitted signal (Black circles), each transducer (red and blue) at 0.3 mK and 34 bars. The green line is obtained by the product of the two FFT (A and B).



(a)



(b)

Figure 4-7. Linearity test. (a) for 40 mK and 33bars and (b) for 0.3 mK, and 33bars.

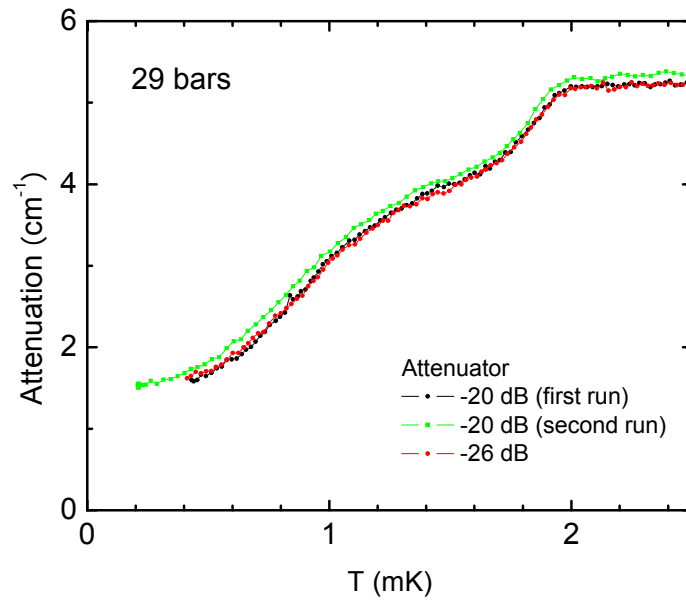


Figure 4-8. No significant change in attenuation indicates that the heating by the transducer is negligible.

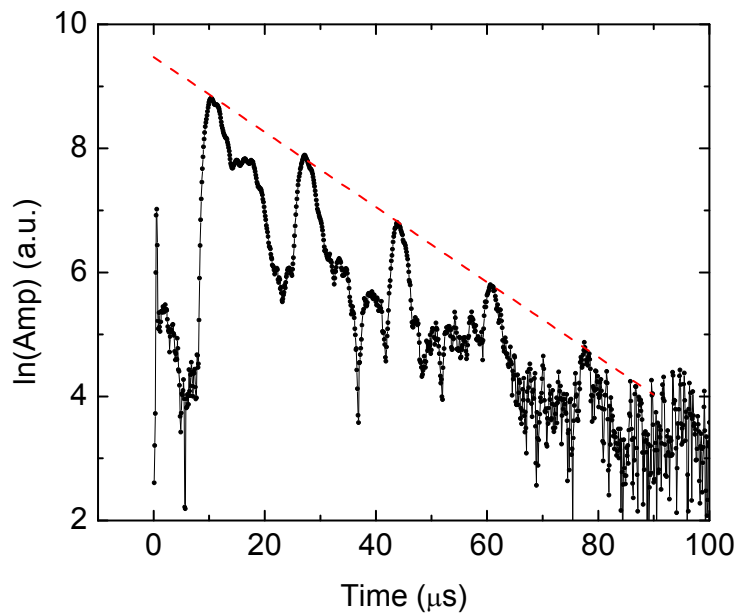


Figure 4-9. Receiver signal trace vs. time at 0.4 mK and 29 bars. The primary signal and the subsequent echoes follow an exponential decay.

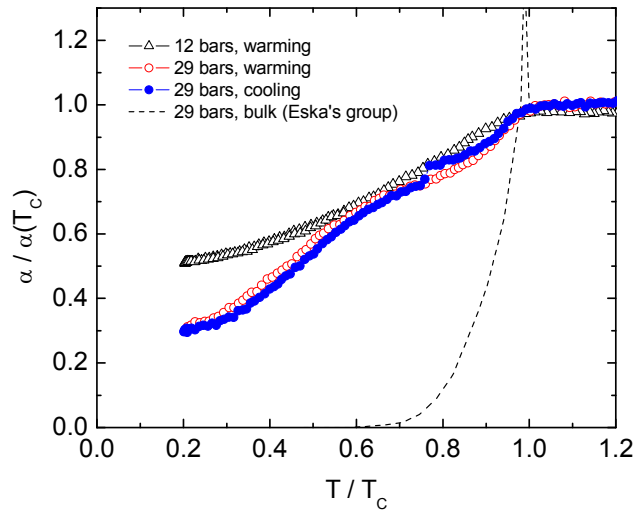


Figure 4-10. The normalized attenuation in the superfluid phase at 12 (triangle) and 29 (circle) bars as a function of the reduced temperature.  $T_C$  represents the superfluid transition temperature for the liquids in aerogel or bulk. The attenuation of the bulk is the measurement by Hristakos [Hri01], i.e. Eska's group.

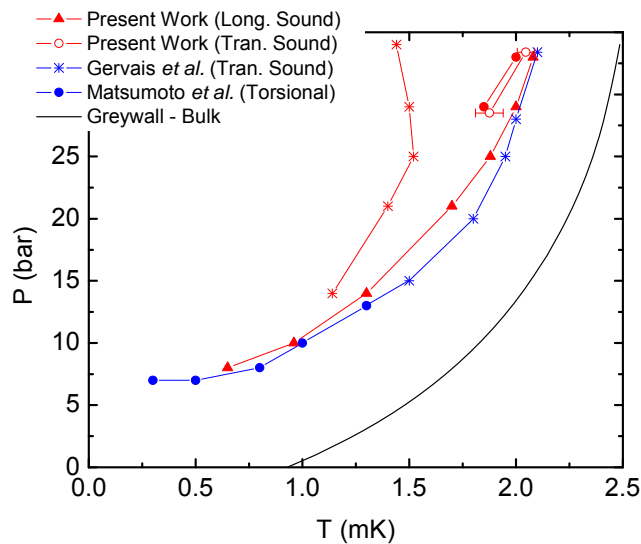


Figure 4-11. Phase diagram at zero field. Our  $T_{ac}$  (red triangle) values agree with those measured in other methods [Mat97, Ger00] (blue data). The  $AB$  transition on warming (red closed circle) and cooling (red star) is also observed in the transmission measurement. The red open circles are data from chapter 3. The black line represents bulk  $T_C$  [Gre86].

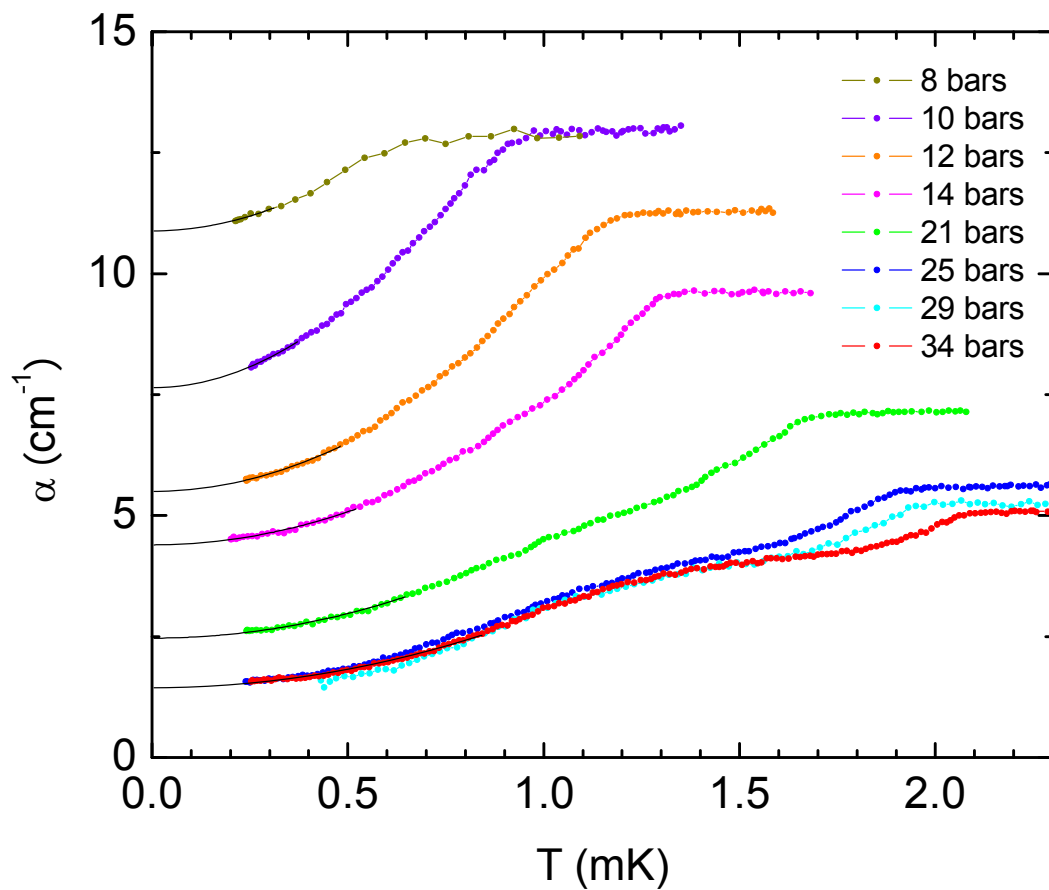


Figure 4-12. Absolute attenuations for pressures from 8 to 34 bars are presented as a function of temperature (on warming except 8 bars). Low temperature attenuation below the lowest temperature data point is obtained using a quadratic extrapolation (thin black line).

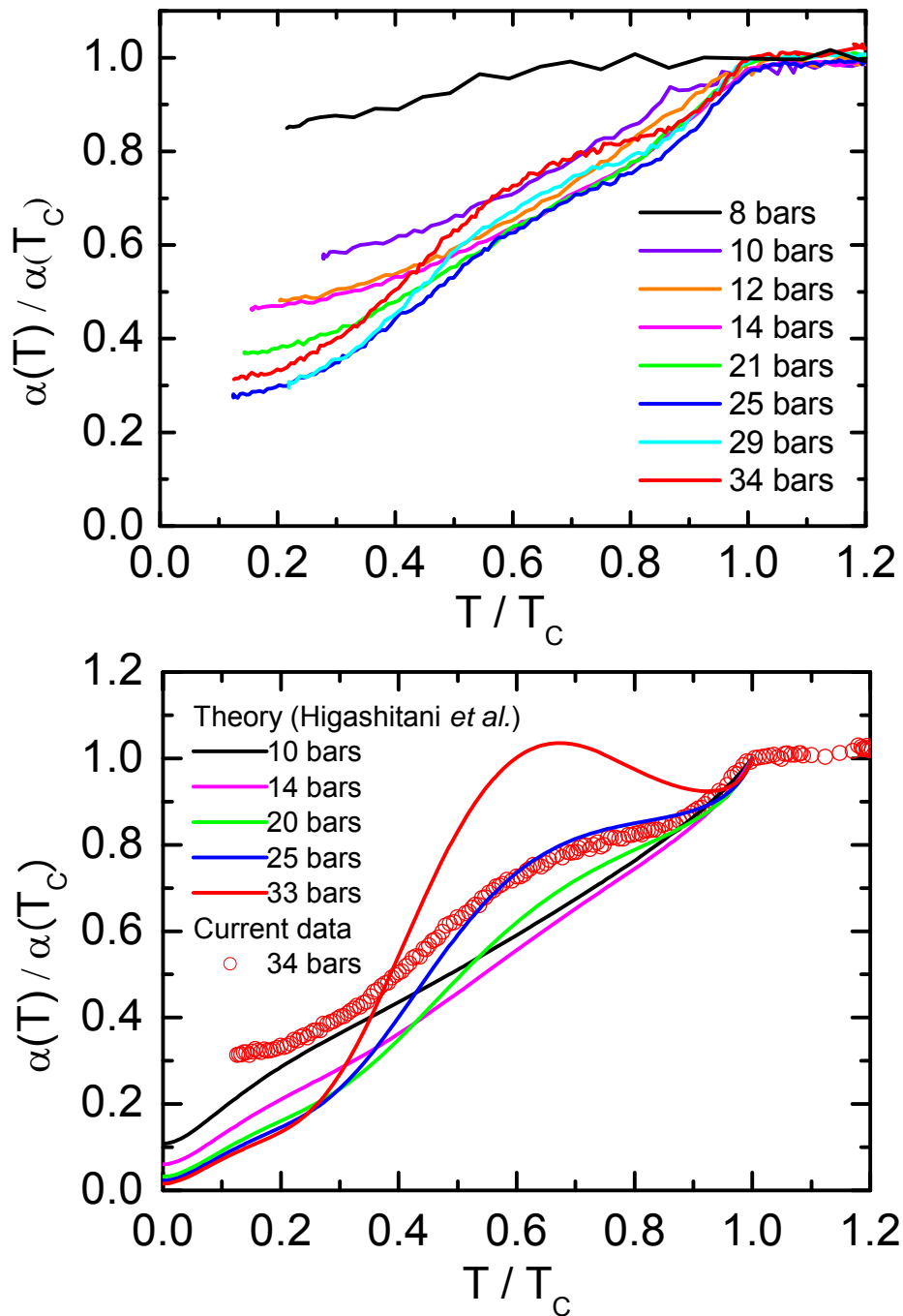


Figure 4-13. Normalized attenuation in superfluid. (a) Normalized attenuations are presented for each pressure (on warming except 8 bars). (b) Each line represents the attenuation calculated by Higashitani *et al.* [Hig06]. Current data for 34 bars are plotted as open circles.

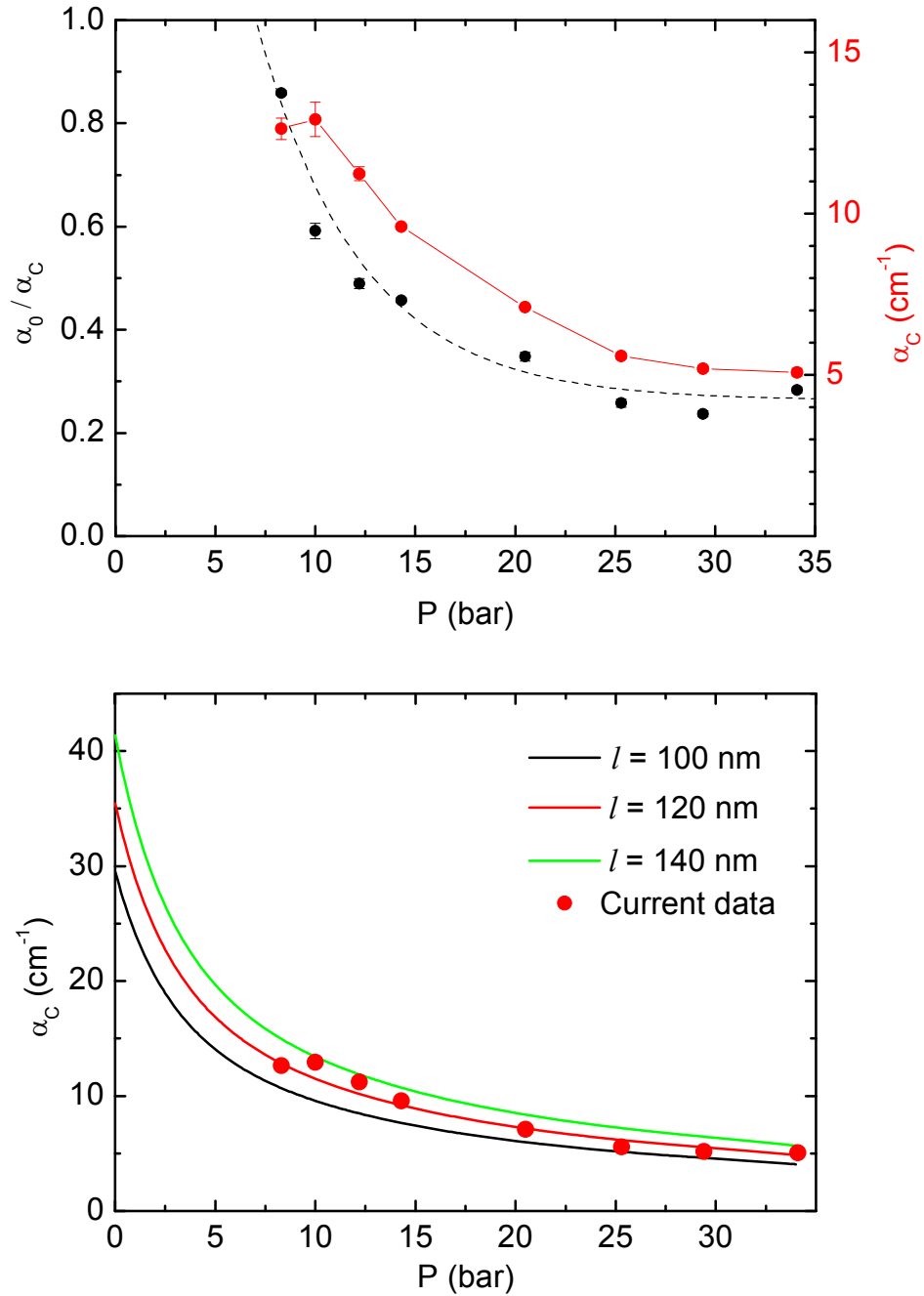


Figure 4-14. Attenuation vs. pressure. (a) Attenuation at the superfluid transition temperature ( $\alpha_c$ ) is plotted as a function of pressure (red circles). A ratio of the zero temperature attenuation to  $\alpha_c$  is presented by the black circles. The dashed line is a guide for eye. (b)  $\alpha_c$  for each mean free path is calculated by Higashitani *et al.* [Hig06] and is presented along with our data.

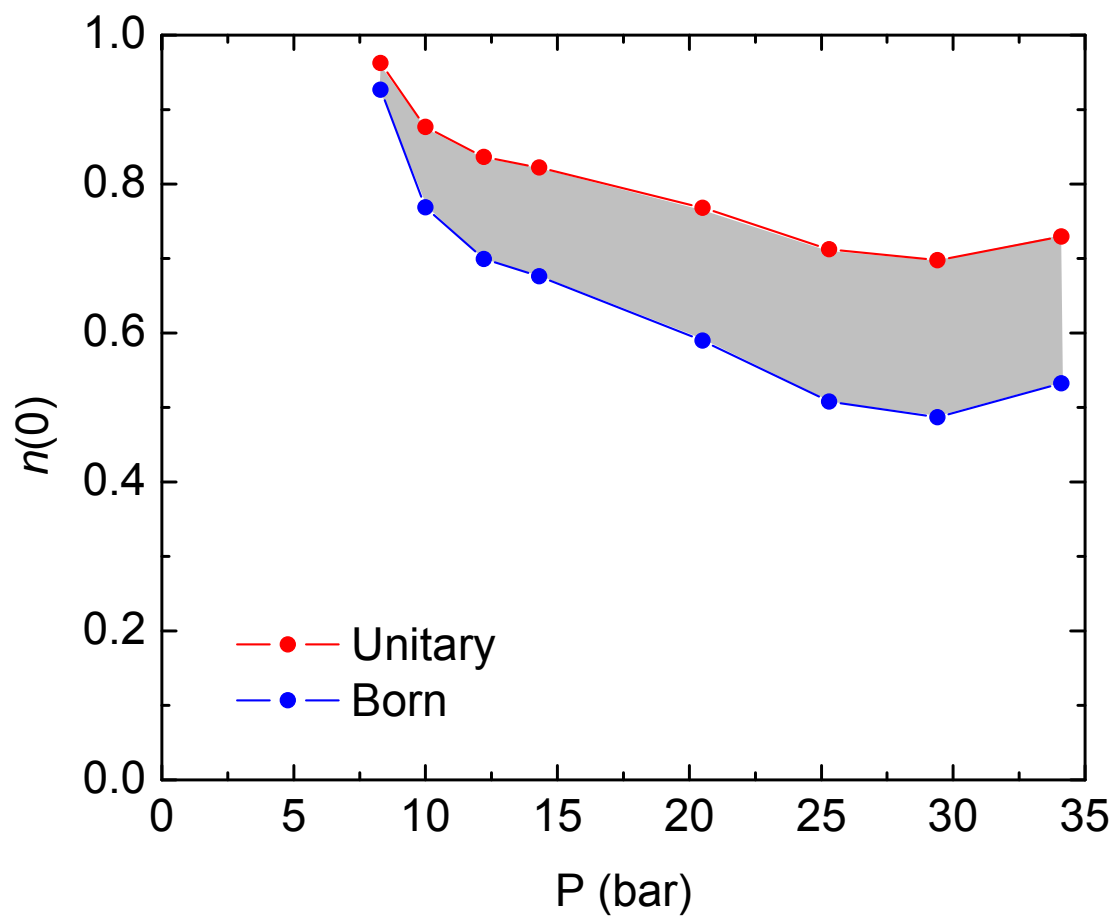


Figure 4-15. Zero energy density of states at zero temperature vs. pressure for the unitary and the Born scattering limits are estimated from  $\alpha_0 / \alpha_C$  in Fig. 4-14.

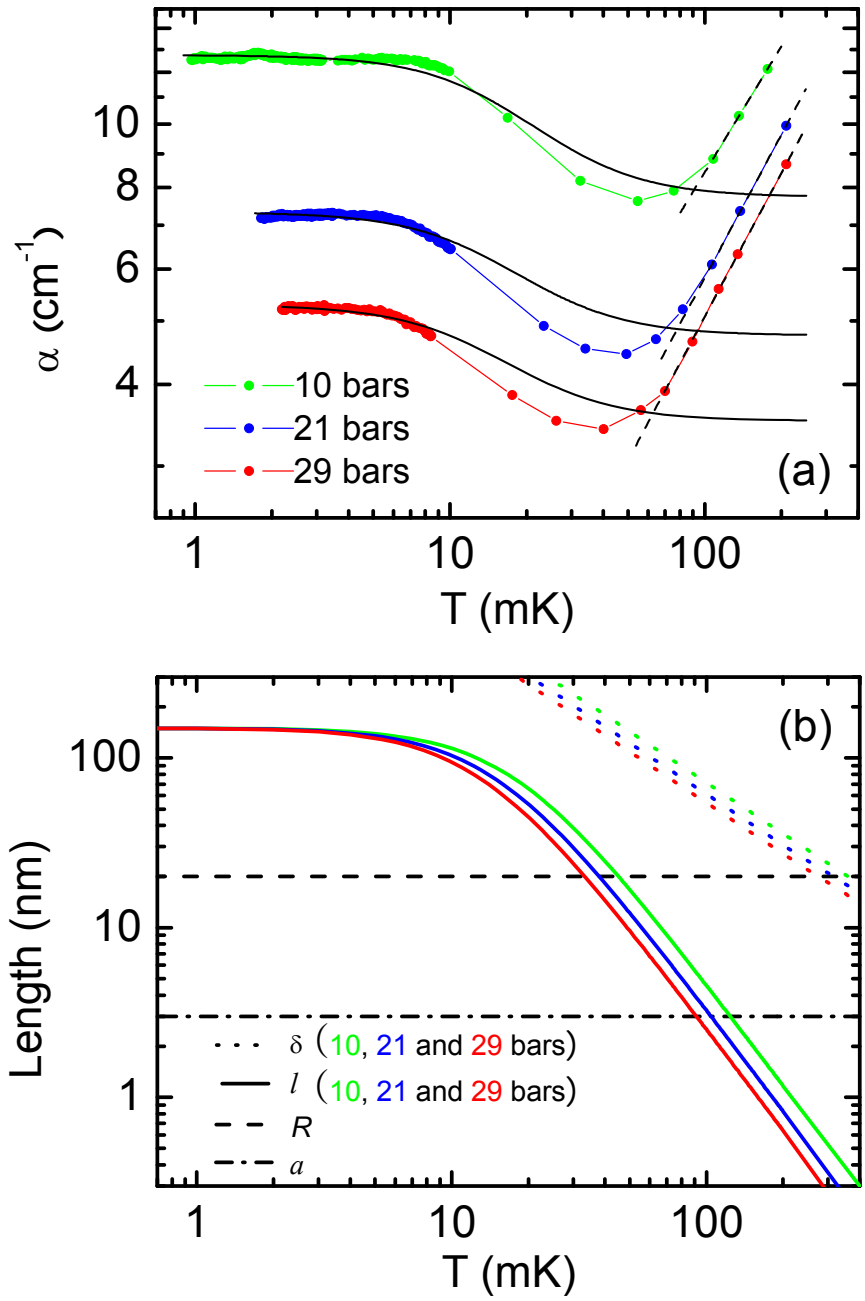


Figure 4-16. Attenuation for normal liquid. (a) Absolute attenuation above the aerogel superfluid transition for each pressure (circle). The solid black line is the result of a fit based on the theory of Higashitani *et al.* [Hig05]. The high temperature part is fit to  $T^{0.7}$  (dashed line). (b) Comparison of the relevant length scales for  $^3\text{He}$  in 98% aerogel.  $l$ : effective mean free path,  $\delta$ : viscous penetration depth,  $R$ : average distance between aerogel strands,  $a$ : average diameter of aerogel strand.

## CHAPTER 5 CONCLUSION

Superfluid  $^3\text{He}$  in high porosity aerogel is a system in which the effects of static impurities on a *p-wave* superfluid can be investigated in a systematic manner. We performed shear acoustic impedance measurements on 98% porosity aerogel in the presence of magnetic fields up to 15 T at the sample pressures of 28.4 and 33.5 bars. We observed the superfluid transition in the aerogel split into two transitions in the presence of magnetic fields above 3 T for both pressures. The field dependence of each transition is consistent with that of the  $A_I$  phase observed in pure liquid with a significantly reduced strong coupling effect. Our results provide the first evidence of the  $A_I$ -like phase in superfluid  $^3\text{He}$ /aerogel.

For the same experimental setup, we observed the  $A$ - $B$  transition on warming in zero magnetic field. Our observations show that the  $A$  and  $B$  phases in aerogel coexist in a width of same temperature of about 100  $\mu\text{K}$ . We propose that differences in the relative stability of the  $A$  and  $B$  phases arising from anisotropic scattering can account for our observations. Consequently, we propose that the effect of anisotropic scattering can be investigated experimentally in a systematic manner, at least in aerogel, by introducing controlled uniaxial stress, which would generate global anisotropy in addition to the local anisotropy. Aoyama and Ikeda's calculations agree with our interpretation with the anisotropic scattering [Aoy05]. Furthermore, in stretched aerogel, a sliver of a new phase, the polar phase, is predicted to appear just below  $T_{aC}$ .

We also performed measurements on longitudinal sound attenuation at 9.5 MHz from 8 to 34 bars in an attempt to investigate the orbital structure of the superfluid phases in 98% aerogel. Using pulsed ultrasound spectroscopic techniques, in the low attenuation regime, we were able to detect several echoes, which allowed us to determine the absolute attenuation. No acoustic features associated with the order parameter collective modes were observed, and these results

are a signature of the hydrodynamic regime [Hig05]. The finite attenuation at zero temperature provides clear evidence for the existence of zero-energy density of states inside the gap induced by impurity scattering. During cooling, the attenuation does not drop as fast as bulk and a shoulder structure is observed at high pressure. This could be explained by the effect of friction between the liquid  $^3\text{He}$  and the aerogel.

In superconductors, tunneling spectroscopy has been widely used in mapping out the gap structure [Wol89]. However, we do not have an equivalent experimental probe in the study of superfluid  $^3\text{He}$ . In this sense, it is interesting to note that unlike specific heat or thermal conductivity, sound attenuation could provide useful information on the profile of the impurity states by exploiting a wide range of excitation frequencies.

With the same experimental configuration, the absolute sound attenuation and sound velocity have been measured in the normal phase of liquid  $^3\text{He}$  in 98% aerogel at 10, 21 and 29 bars up to 200 mK. The attenuation shows a minimum at  $T_M \approx 40$  mK for 29 bars and follows a power law,  $T^{0.7}$ , for  $T > T_M$ . As the pressure is lowered,  $T_M$  is shifted to higher temperature. Currently, we do not have an explanation for the origin of the  $T^{0.7}$  dependence at  $T > T_M$ . As expected from a two-fluid model that incorporates impurities, the sound velocity is reduced from the bulk value at the same pressure by 20% and remains constant for the whole temperature range. Due to the scattering of the aerogel, the sound excitation remains as first sound over the entire range of temperatures and pressures studied, which is identified by the absence of a first to zero sound transition.

APPENDIX A  
ORIGIN SCRIPT FOR MPT CALIBRATION IN THE HIGH FIELD PHASE

I programmed MPTfukuyamalessTn.c and MPTfukuyamalow5.c with Origin C to calibrate numerically the MPT. These Origin C files should be located in the Origin C folder and are operated with Origin7.0-SR4. MPTfukuyamalessTn.c calculates a pressure shift for MPT calibration,  $P_{ad}$ , from the width of bulk  $A_1$  phase. MPTfukuyamalow5.c is programmed to calculate temperature for a given MPT pressure using  $P_{ad}$ . A text object was used to execute the C program. For example, if we click the text object, ' $\rightarrow T_{A_1}$ ', in the worksheet, 'Pad', it will calculate and show  $T_{A_1}$  and  $P_{ad}$  (Fig. A-1). A label control of the text object needs to be set as shown in Fig. A-2. How to make the object can be found at 'Objects on Windows' in the Origin Help menu. Worksheet 'PtoT' calculates temperature from MPT pressure, P, when the ' $P \rightarrow T$ ' object is clicked. Input parameters are arranged above the button. In Label Control for ' $P \rightarrow T$ ' object, PTfukuyamalow5 replaces MPTfukuyamalessTn.



	A[X]	Input[Y]	P[Y] kPa	T[Y] mK
1			3415.50907	1.44812
2			3415.50904	1.44812
3			3415.509	1.44812
4			3415.50897	1.44812
5			3415.50894	1.44812
6			3415.50894	1.44812
7			3415.50893	1.45724
8	P0	–	3408.68703	3415.50893
9	c4	–	-5.33531E-4	3415.50891
10	c6	–	-5.21108E-4	3415.5089
11	Pad	–	6.82916	3415.50889
12		–	P->T	3415.50889
13		–		3415.50888

Figure A-3. Origin worksheet, ‘PtoT’, calculates temperature, T, from MPT pressure, P.  $P_0, c_4, c_6$  are MPT calibration parameters for high field phase [Yaw01].  $P_{ad}$  is obtained from worksheet ‘Pad’.

## A.1 MPTfukuyamalessTn.c

```
//////////BEGIN
#include <origin.h>
//3He melting pressure temperature scale (Fukuyama scale).
//P in bar, T in mK.
//by Hyunchang Choi, Sept 2003 at UF.
//This convert Pressure to Temperature (from column named 'P' to 'T')
//Scale for 1~250mK
//Neel pressure 'Pn' should be given from script(Labtalk).

#define MAXIT 300           //Maximum allowed number of iterations.
#define Tacc 0.001         //accuracy of Temperature
#define Tmin 0.5           //Maximum and minimum of Temperature scale
#define Tmax 3.5

void MPTfukuyamalessTn()
{
    char    szTemp[100];           //Get active worksheet Name.
    LT_get_str("%H", szTemp, 100);
    string  worksheetName = szTemp;
    Dataset dd1(worksheetName+"_Ta1");
    dd1.SetSize(1);
    dd1[0]=rtsafe(Tmin,Tmax,Tacc); //Call root finding function.
}

float rtsafe(float x1,float x2,float xacc) //from 'Numerical recipes in C'
//Using a combination of Newton-Raphson and bisection, find the root of a function bracketed
//between x1 and x2. The root, returned as the function value rtsafe, will be refined until
//its accuracy is known within +/-xacc.funcd is a user-supplied routine that returns both the
//function value and the first derivative of the function.
{
    int j;
    float df,dx,dxold,f,fh,fl;
    float temp,xh,xl,rts;

    funcd(x1,&fl,&df);
    funcd(x2,&fh,&df);
    if ((fl>0.0&&fh>0.0)||(fl<0.0&&fh<0.0))
        nerror("Root must be bracketed in rtsafe");
    if (fl==0.0) return x1;
    if (fh==0.0) return x2;
    if (fl<0.0){ //Orient the search so that f(x1)<0.
        xl=x1;
        xh=x2;
    }else{
        xh=x1;
    }
}
```

```

        xl=x2;
    }
    rts=0.5*(x1+x2); //Initialize the guess for root,
    dxold=fabs(x2-x1); //the "stepsize before last,"
    dx=dxold; //and the last step.
    funcd(rts,&f,&df);
    for (j=1;j<=MAXIT;j++){ //Loop over allowed iterations.
        if (((rts-xh)*df-f)*((rts-xl)*df-f)>0.0) //Bisect if Newton out of range,
            || (fabs(2.0*f)>fabs(dxold*df)) { //or not decreasing fast enough.
                dxold=dx;
                dx=0.5*(xh-xl);
                rts=xl+dx;
                if (xl==rts) return rts; //Change in root is negligible.
            } else { //Newton step acceptable. Take it.
                dxold=dx;
                dx=f/df;
                temp=rts;
                rts-=dx;
                if (temp==rts) return rts;
            }
            if (fabs(dx)<xacc) return rts; //Convergence criterion.
            funcd(rts,&f,&df);
            //the one new function evaluation per iteration.
            if (f<0.0) //Maintain the bracket on the root.
                xl=rts;
            else
                xh=rts;
        }
        nrrror("Maximum number of iteration exceeded in rtsafe");
        return 0.0; //Never get here
    }
}

```

```

void funcd(float T,float *f,float *df)
{
    double dP,dT,c4,c6;
    char szTemp[100]; //Get active worksheet Name.
    LT_get_str("%H",szTemp,100);
    string worksheetName = szTemp;
    Dataset dd1(worksheetName+"_dP");
    Dataset dd2(worksheetName+"_dT");
    Dataset dd3(worksheetName+"_c4");
    Dataset dd4(worksheetName+"_c6");

    dP=dd1[0];dT=dd2[0];c4=dd3[0];c6=dd4[0];
    *f=dP+c4*(T^4-(T-dT)^4)+c6*(T^6-(T-dT)^6);
    *df=4*c4*(T^3-(T-dT)^3)+6*c6*(T^5-(T-dT)^5);
}

```

```
}  
  
//For error message.  
void nerror(char *error_text)  
{  
    printf("%s\n", error_text);  
    exit(1);  
}  
/////////END
```

## A.2 MPTfukuyamalow5.c

```
//////////BEGIN
#include <origin.h>
//3He melting pressure temperature scale (Fukuyama scale).
//P in bar, T in mK.
//by Hyunchang Choi, Sept 2003 at UF.
//This convert Pressure to Temperature (from column named 'P' to 'T')
//Scale for 1~250mK
//Neel pressure 'Pn' should be given from script(Labtalk).

#define MAXIT 300           //Maximum allowed number of iterations.
#define Tacc 0.001         //accuracy of Temperature
#define Tmin 0.1           //Maximum and minimum of Temperature scale
#define Tmax 3.5

void MPTfukuyamalow5()
{
    char    szTemp[100];           //Get active worksheet Name.
    LT_get_str("%H", szTemp, 100);
    string  worksheetName = szTemp;

    Dataset dd1(worksheetName+"_P");
    Dataset dd2(worksheetName+"_T");
    UINT nRows=dd1.GetSize();
    dd2.SetSize(nRows);
    for(int ii=dd1.GetLowerIndex();ii<dd1.GetUpperIndex();ii++)
        dd2[ii]=rtsafe(dd1[ii],Tmin,Tmax,Tacc);    //Call root finding function.
}

float rtsafe(float P,float x1,float x2,float xacc)    //from 'Numerical recipes in C'
//Using a combination of Newton-Raphson and bisection, find the root of a function bracketed
//between x1 and x2. The root, returned as the function value rtsafe, will be refined until
//its accuracy is known within +/-xacc.funcd is a user-supplied routine that returns both the
//function value and the first derivative of the function.
{
    int j;
    float df,dx,dxold,f,fh,fl;
    float temp,xh,xl,rts;

    funcd(P,x1,&fl,&df);
    funcd(P,x2,&fh,&df);
    if ((fl>0.0&&fh>0.0)||(fl<0.0&&fh<0.0))
        nerror("Root must be bracketed in rtsafe");
    if (fl==0.0) return x1;
    if (fh==0.0) return x2;
```

```

        if (fl<0.0){
f(x1)<0.          //Orient the search so that
                xl=x1;
                xh=x2;
        }else{
                xh=x1;
                xl=x2;
        }
        rts=0.5*(x1+x2);
        dxold=fabs(x2-x1);
        dx=dxold;
        funcd(P,rts,&f,&df);
        for (j=1;j<=MAXIT;j++){
iterations.
                if (((rts-xh)*df-f)*((rts-xl)*df-f)>0.0)
                    || (fabs(2.0*f)>fabs(dxold*df)) {
                        dxold=dx;
                        dx=0.5*(xh-xl);
                        rts=xl+dx;
                        if (xl==rts) return rts;
                    } else {
                        dxold=dx;
                        dx=f/df;
                        temp=rts;
                        rts-=dx;
                        if (temp==rts) return rts;
                    }
                if (fabs(dx)<xacc) return rts;
                funcd(P,rts,&f,&df);
                //the one new function evaluation per iteration.
                if (f<0.0)
                    xl=rts;
                else
                    xh=rts;
            }
        nrerror("Maximum number of iteration exceeded in rtsafe");
        return 0.0;
}

```

```

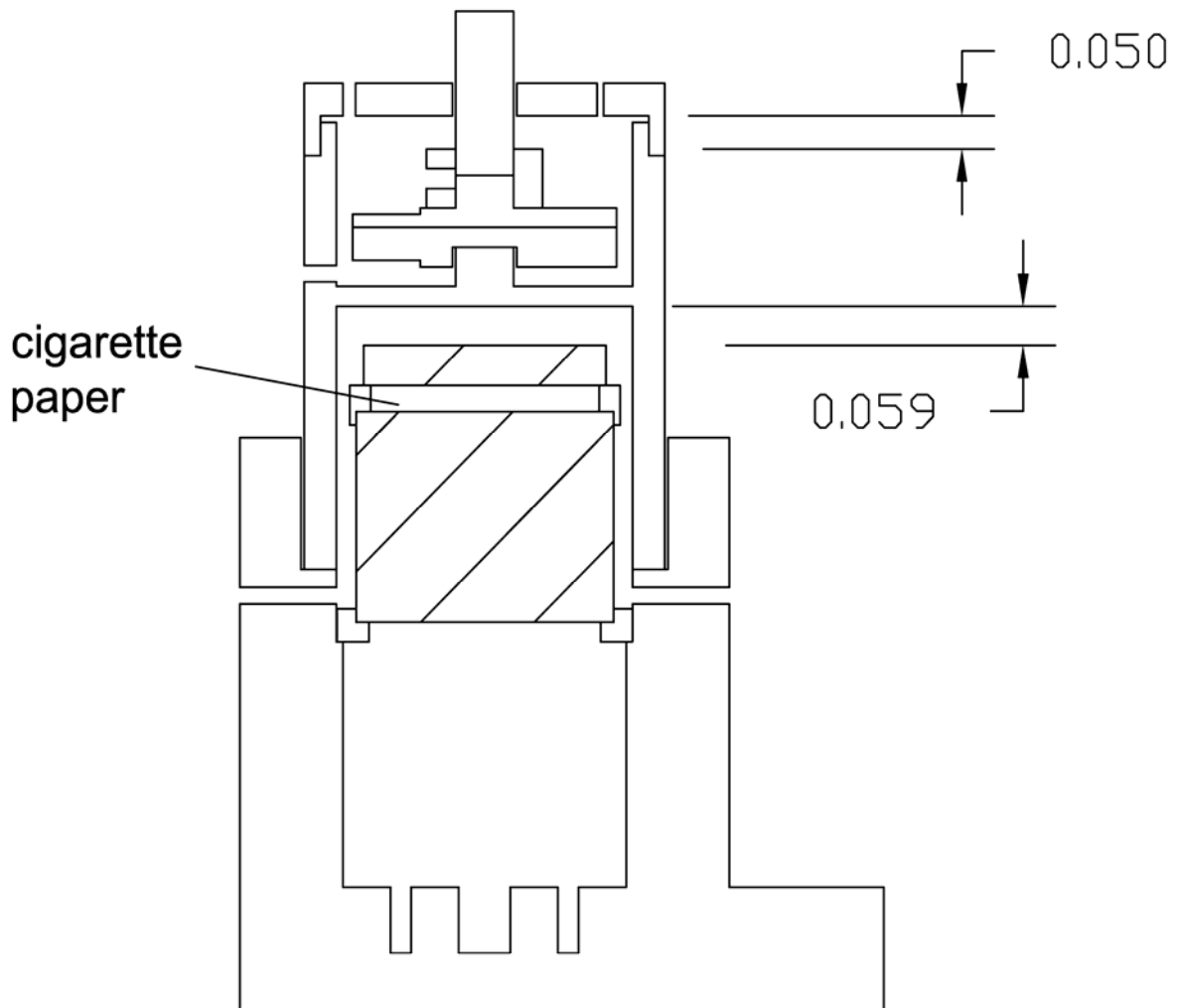
void funcd(float P,float T,float *f,float *df)
{
    char  szTemp[100];
    LT_get_str("%H",szTemp,100);
    string worksheetName = szTemp;
    Dataset dd1(worksheetName+"_Input");
}

```

```
        *f=dd1[7]+dd1[10]-P+dd1[8]*T^4+dd1[9]*T^6;
        *df=4*dd1[8]*T^3+6*dd1[9]*T^5;
    }

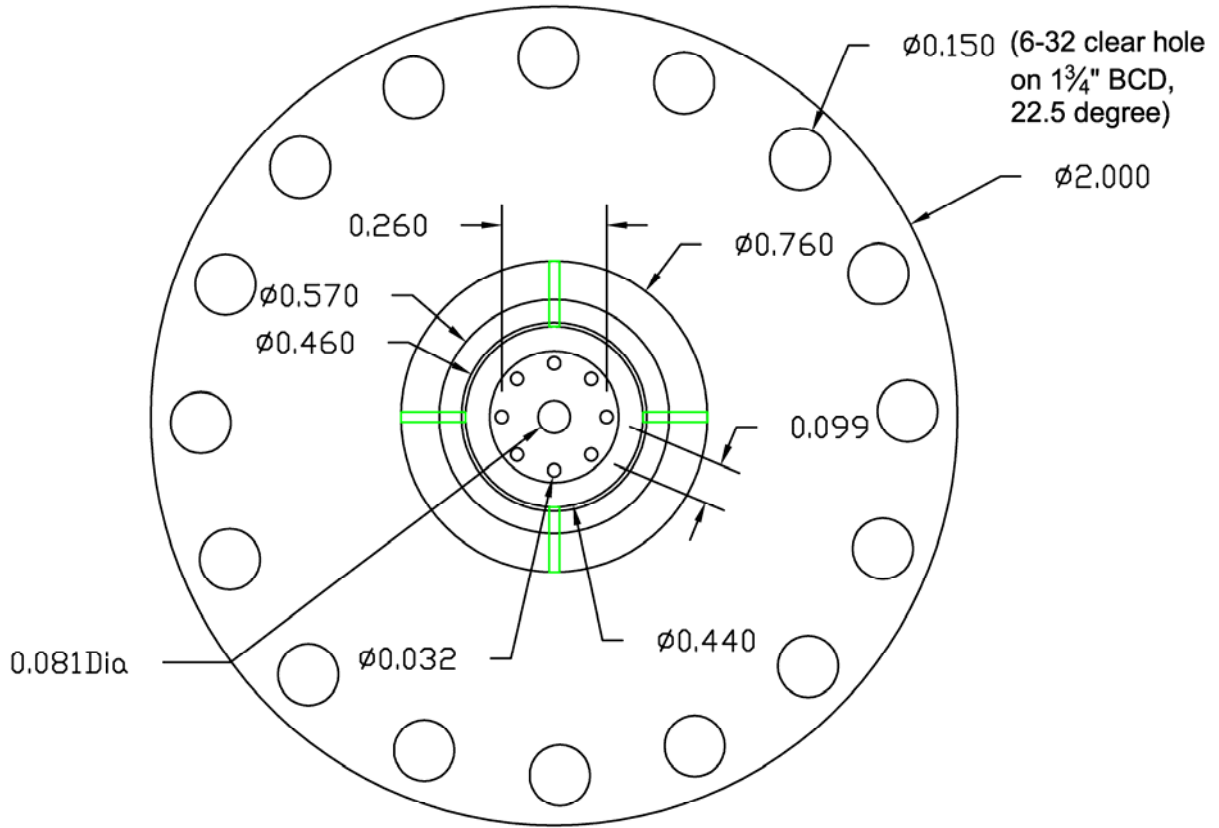
//For error message.
void nrerror(char *error_text)
{
    printf("%s\n", error_text);
    exit(1);
}
//////////END
```

APPENDIX B  
PARTS OF THE EXPERIMENTAL CELL FOR ATTENUATION MEASUREMENT

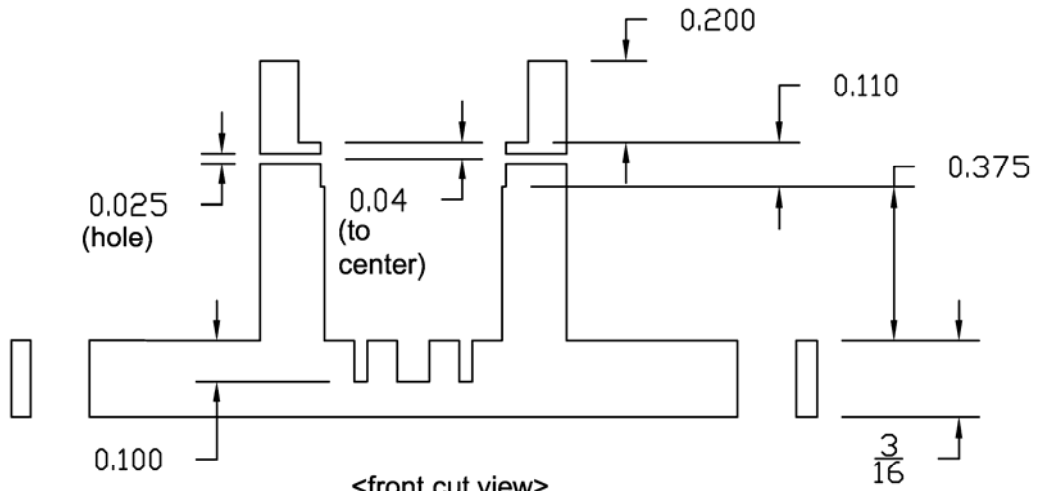


V(3He)~1.8cc  
 A(sinter)~8.9m<sup>2</sup>

AcouCell | assembled, just for view | Hyunchang Choi |  
 Jan.11,2005 | inch | B131NPB, 846-3121 | 1/5



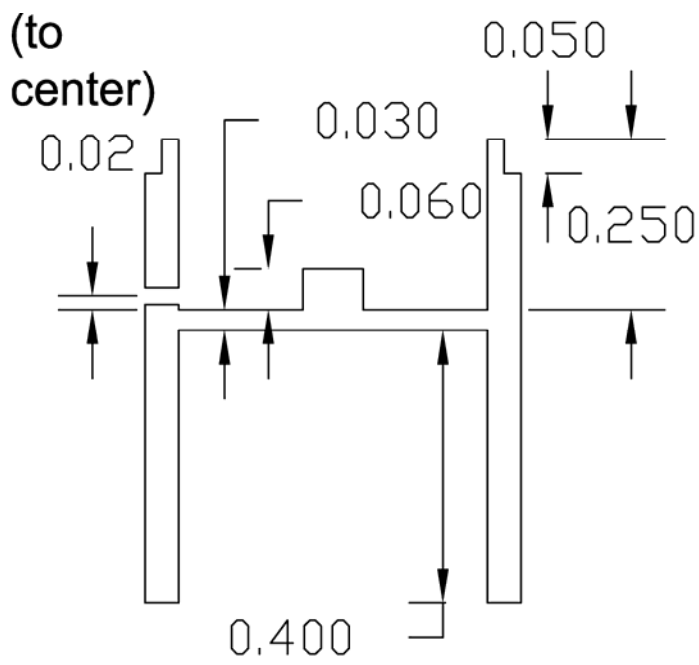
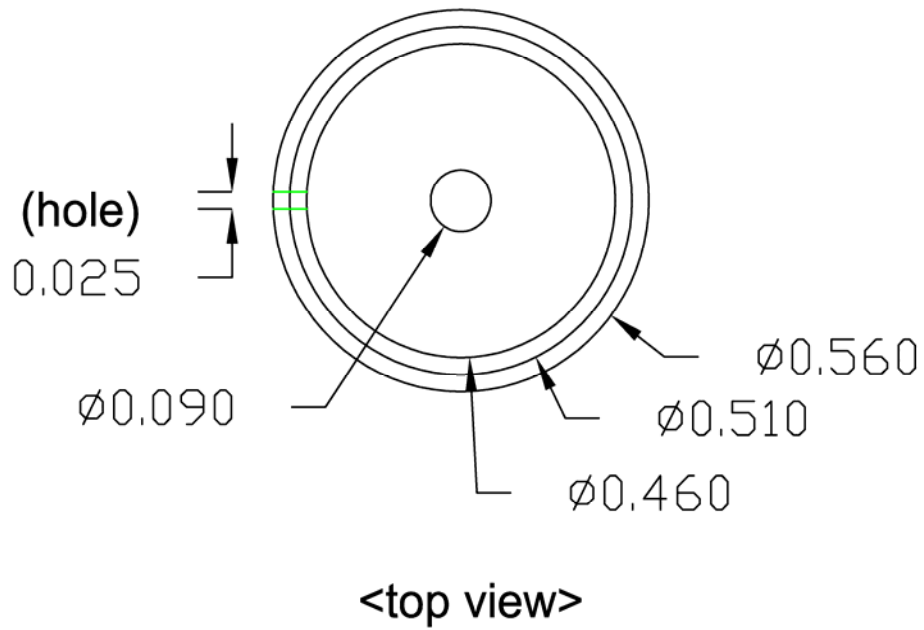
<top view>



<front cut view>

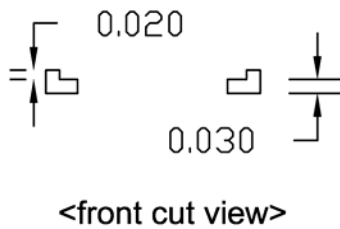
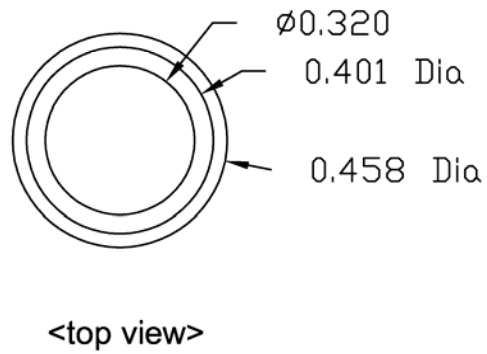
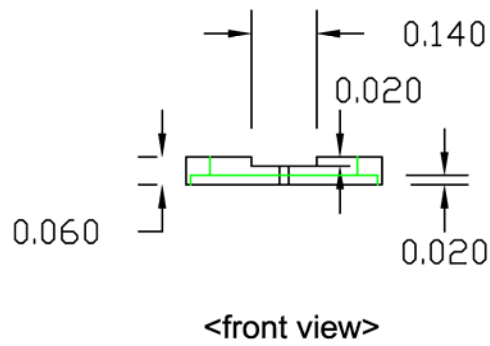
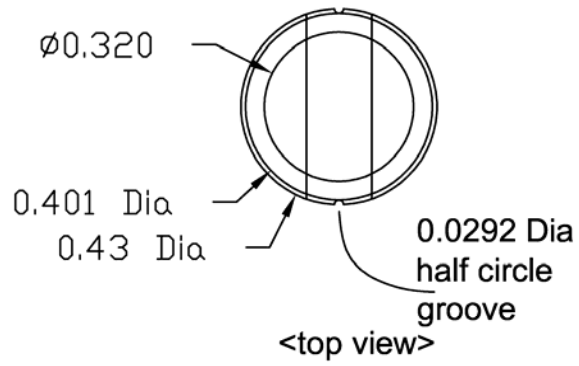
(green lines show inside view)

Bottom | Silver | Qt.1 | Hyunchang Choi | Jan.11,2005 |  
 inch | B131NPB, 846-3121 | 2/5

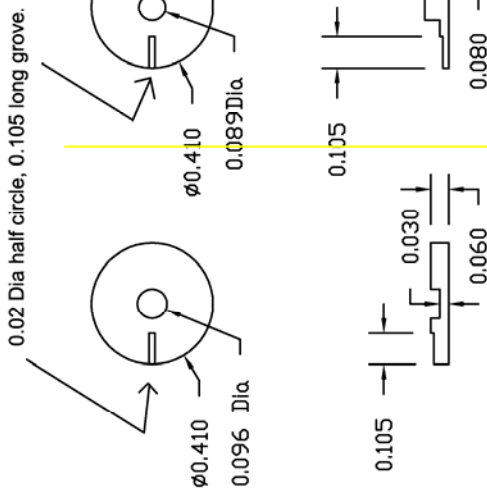


<front cut view>

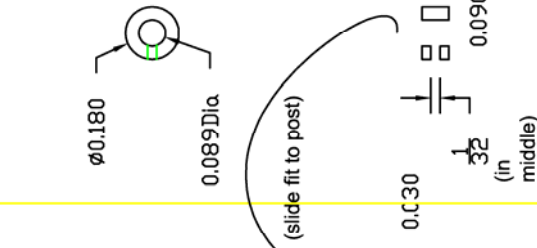
Middle | CoinSilver | Qt.2 | Hyunchang Choi | Jan.11,2005 |  
inch | B131NPB, 846-3121 | 3/5



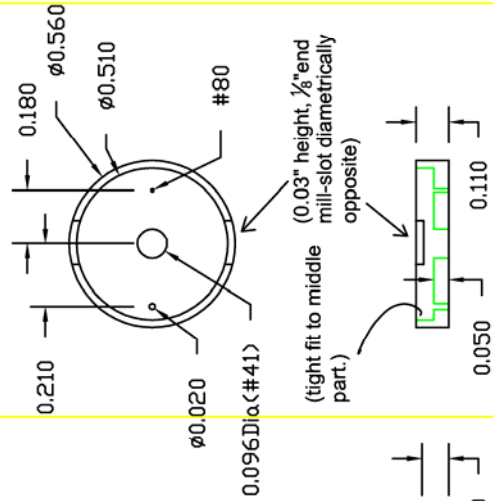
MacorSit | Macor | Qt.2 each | Hyunchang Choi |  
 Jan.11,2005 | inch | B131NPB, 846-3121 | 4/5



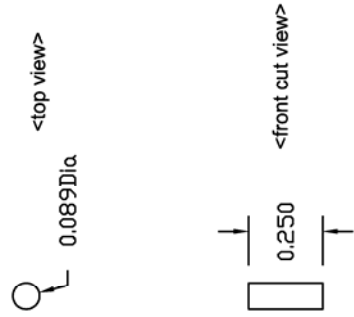
[CoinSilver, Qt.3 each]



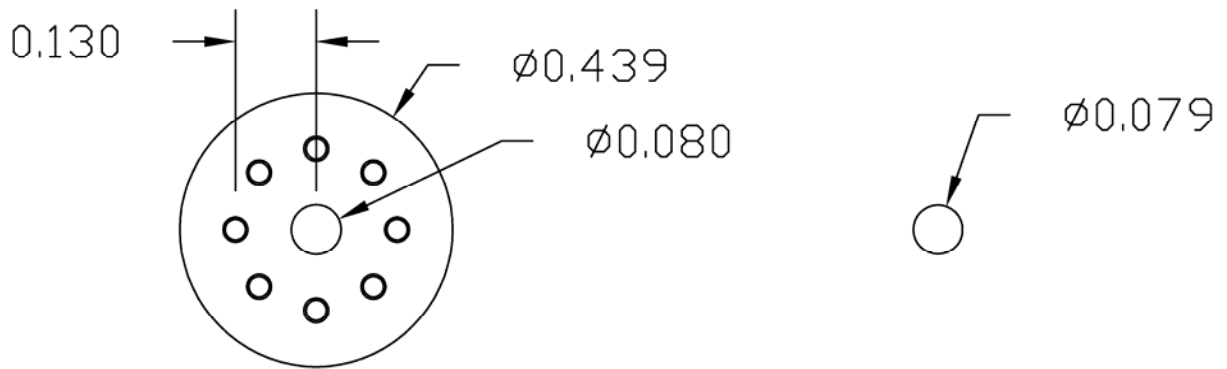
[VespeI, Qt.2]



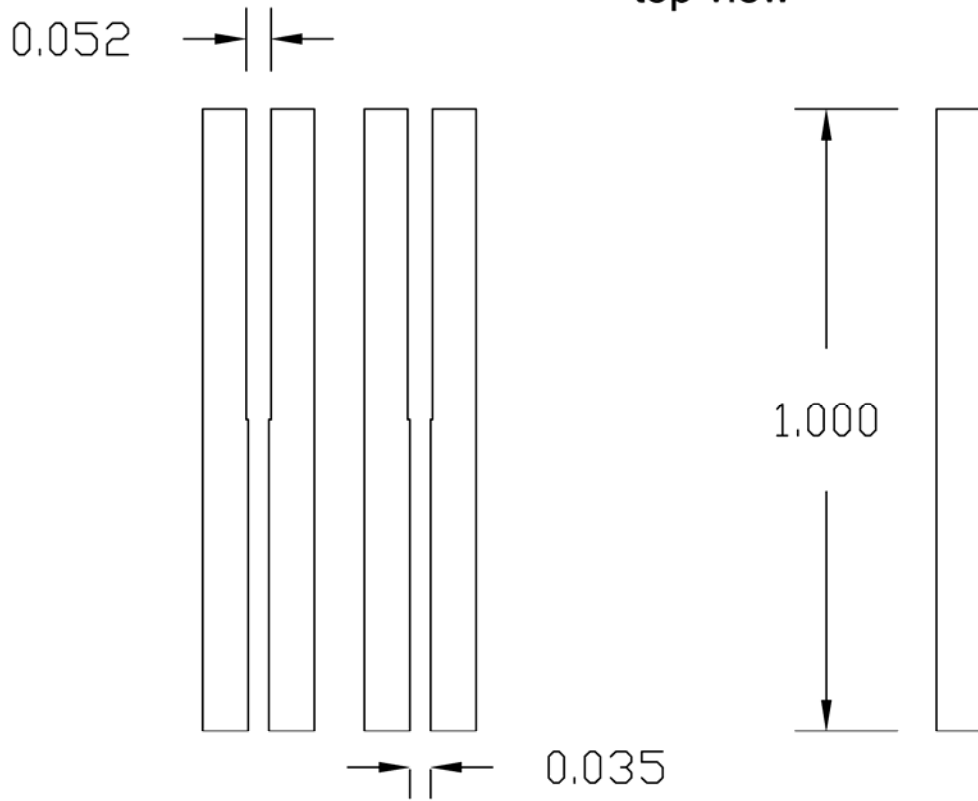
[CoinSilver, Qt.2]



[CoinSilver, Qt.2]



<top view>



<front cut view>

packing tool | S.S. | Qt.1 | Hyunchang Choi | Jan.11,2005 |  
inch | B131NPB, 846-3121 | 1/1

## APPENDIX C TYPICAL SETTING FOR NMRKIT II

NMRKitII/ LIBRA spectrometer was controlled by Macintosh computer. The NMRkitII software was commanded by the apple script to measure one sequence of transmitted signal and save it as a file. Labview was programmed to save data every 5 minutes for the MPT, the PtNMR thermometer, the transverse transducer, the cell pressure and the NMRkitII. For each data point, the Labview program calls the application written by apple script and the application orders the NMRkitII software to take and save data. The detail of apple script can be found in Watson's thesis [Wat00]. The typical setting for NMRkitII is given in Fig. C-1.

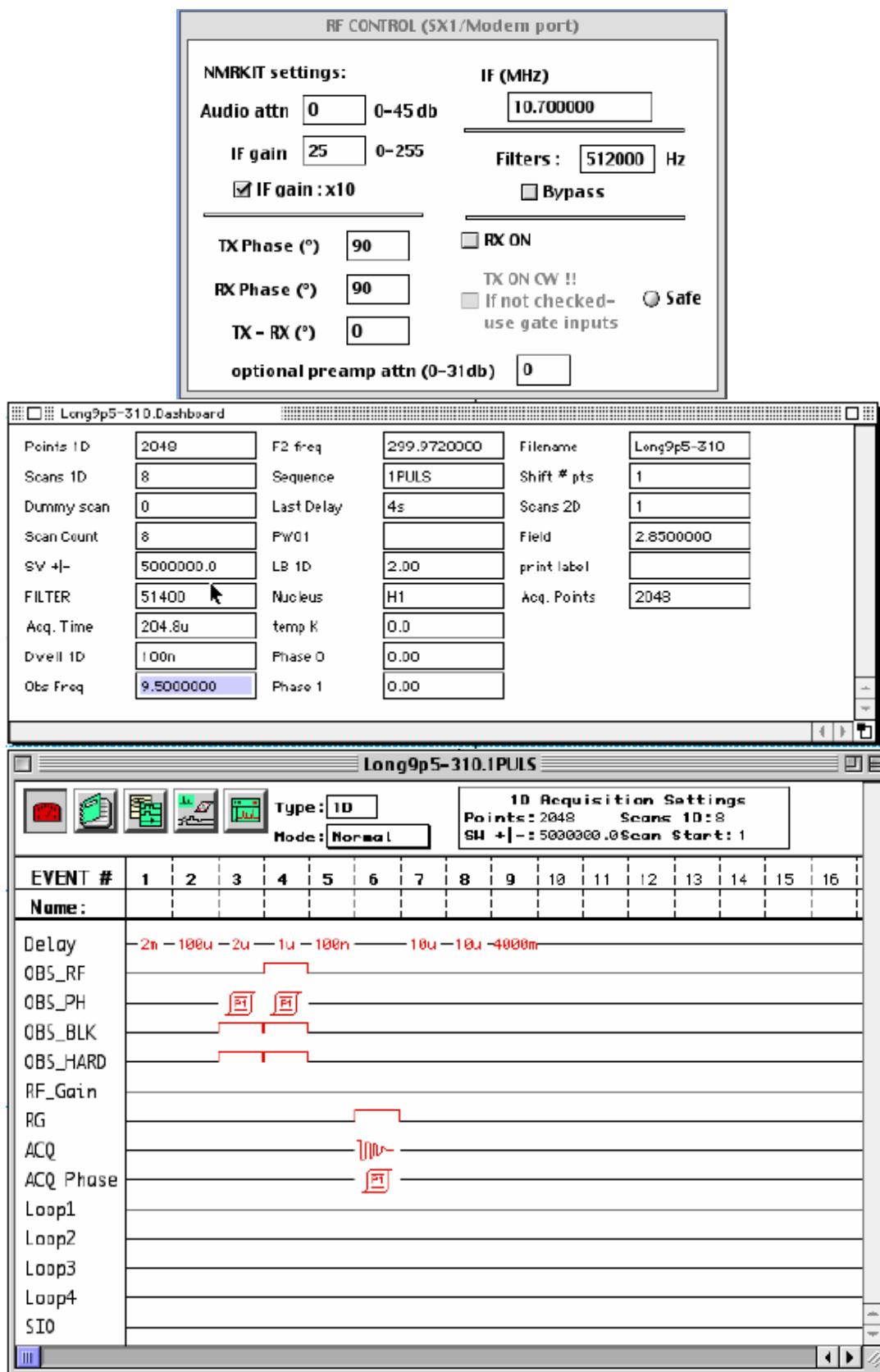


Figure C-1. The typical NMRkitII setting.

APPENDIX D  
ORIGIN SCRIPT FOR THE DATA ANALYSIS OF THE ATTENUATION  
MEASUREMENTS

Because the data taken by NMRkitII were huge in file size, an Origin script, '1main2.ogs' was programmed for importing and analyzing data. It was operated in Origin 6 or Origin 7. The screen shot of the Origin widow for data analysis is shown in Fig. D-1. Buttons to execute the Origin scripts are arranged on a layout, 'EXEbutton'. The buttons 'Import Data', 'Upload LS' and 'Upload Pt' are for importing data from the Labview program, the NMRkitII and the PrNMR thermometer. The button, 'CalMCT', is for calibrating temperature from a given MPT pressure in the spreadsheet 'MCTcal'. The spreadsheet 'MCTcalUF' is the P-T table of MPT UF scale and it is used during the calibration procedure. The buttons, 'Integ LS' and 'Sum Pt' are used to obtain the area of each signal from the longitudinal sound and the PtNMR. The ranges of data points for the area calculation are specified in the spreadsheet 'para'.

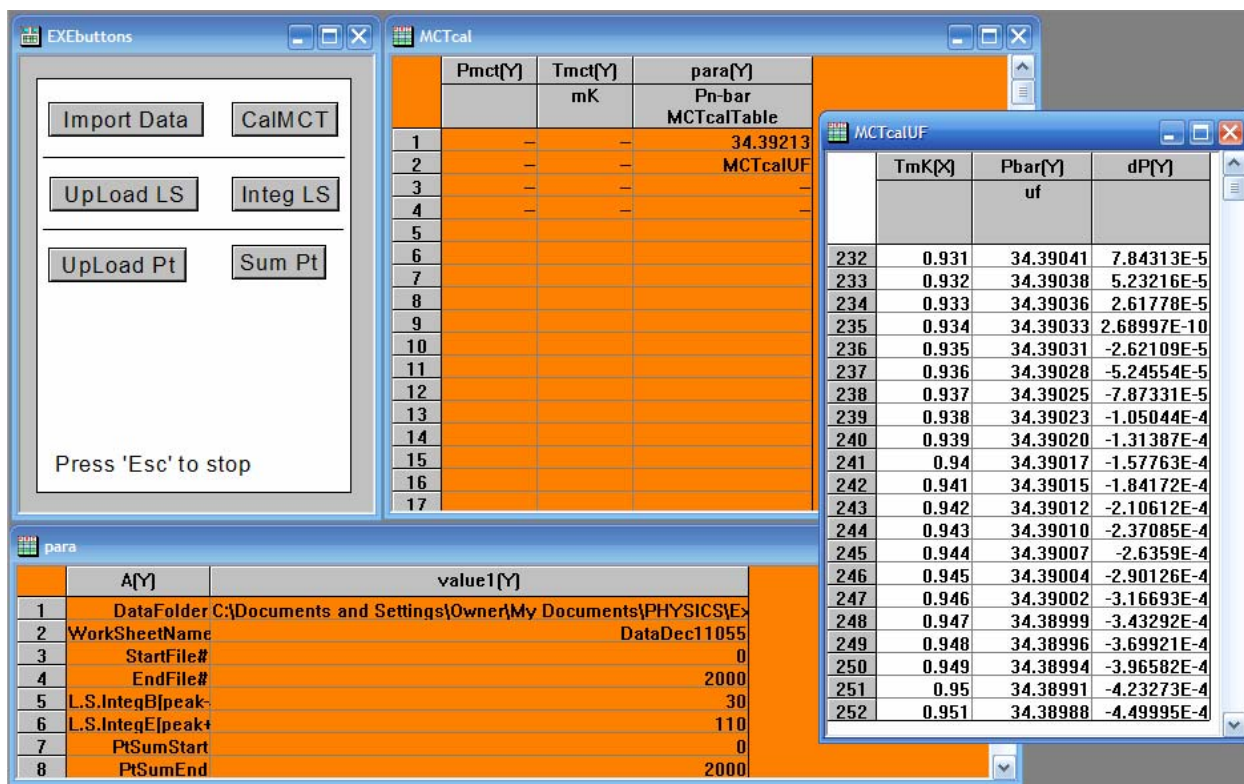


Figure D-1. The screen shot of Origin worksheet for data analysis.

## 1main2.ogs

```
//Hyunchang Choi;
//Necessary templates
//1fixedFN.otw ; worksheet template; contain two colulm named A and B, both set as Y axis.
//          Uncheck "Rename Worksheet to data file name" in ASCII import options.
//1MultiGraph.otp; graph template; five layers are arranged for each graph.
////////////////////////////////////////////////////////////////////////////////////////////////////////////////////////////////
//MCT Temp Calibration
////////////////////////////////////////////////////////////////////////////////////////////////////////////////////////////////;
[MCTcal]
type -b Did you check parameters?;
%D=MCTcal;
N=%(%D,3,1);    //Pn;
%l=%(%D,3,2);    //cal table;
win -a %D;
loop(i,1,wks.maxrows){
t=%D_Pmct[i]-N;
for (k=1; k<500;k++){
s=k*500+1;
if (t>%l_dP[s]){
for (j=1; j<=500; j++){
q=(k-1)*500+j;
if (t>=%l_dP[q]){
%D_Tmct[i]=%l_TmK[q];
break;}};
break;}};}};
type -b save file;

////////////////////////////////////////////////////////////////////////////////////////////////////////////////////////////////
//Import main dataset
////////////////////////////////////////////////////////////////////////////////////////////////////////////////////////////////;
[ImportData]
create data -w 1000;
getfile *.dat ;open -w %A;
wks.col1.name$=fileN;
wks.col2.name$=cellPb;
wks.col3.name$=cellPa;
wks.col4.name$=NewMCTb;
wks.col5.name$=NewMCTa;
wks.col6.name$=TranSXb;
wks.col7.name$=TranSXa;
wks.col8.name$=TranSYb;
wks.col9.name$=TranSYa;
wks.col10.name$=longS;
wks.col11.name$=pt;
wks.col12.name$=time;
```

```

wks.addcol(Smct2);
wks.addcol(SGpt);
wks.addcol(longSI);
wks.addcol(longSv);
wks.col13.label$=5fftSmooth;
wks.col14.label$=9sgSmooth;
wks.col1.type=1;
wks.labels();

%w=%h;
win -a %w;
%(para,2,1)="%B";
%(para,2,2)="%w";

worksheet -s 2 0 2 0; // select column 2
worksheet -p 202 1MultiGraph.otp; // plot selected column
layer -s 1;layer -i202 %w_cellPa;layer -a;
layer -s 2;layer -i202 %w_NewMCTa;layer -a;
layer -s 3;layer -i202 %w_TransXa;layer -a;
layer -s 4;layer -i202 %w_longS;layer -a;
layer -s 5;layer -i202 %w_pt;layer -a;
//layer -s 6;layer -d;
label -s -d 1300 100 %w;

getsave %w.opj;

////////////////////////////////////////////////////////////////////////////////////////////////////////////////////////////////
//Load Long Sound data;
////////////////////////////////////////////////////////////////////////////////////////////////////////////////////////////////
//.....;
//This script import long9p5-#.dat files, calculate magnitude from x,y
//and save it within one worksheet. If open a worksheet for each data file;
//origin file become huge and the process is too slow.;
//Jan13,2006 Hyunchang Choi;
//.....;
[LoadLS]
type -b Did you check parameters?;
%F=%(para,2,1); //data folder
%M=%(para,2,2);
B=%(para,2,3); //beginning file;
E=%(para,2,4); //end file;
create LSmag -w 1000;
wks.col1.type=1;
label -s %M;
win -t data 1fixedFN.otw long9p5; //Import rename off, col A set as y.
loop(ii,B,E){ //loop() is more stable than for()

```

```

window -a long9p5;
open -w %Flong9p5-$(ii).dat;
window -a LSmag;
worksheet -i ii f$(ii);
LSmag_f$(ii)=sqrt(long9p5_A^2+long9p5_B^2);
};
win -cd long9p5;
type -b save file;

/////////////////////////////////////////////////////////////////
//Integrate Long Sound
/////////////////////////////////////////////////////////////////;
[IntegLS]
type -b Did you check parameters?;
//Parameters.....
%M=%(para,2,2); //save file name
B=%(para,2,3); //beginning file;
E=%(para,2,4); //end file;
p=%(para,2,5);
q=%(para,2,6);
//.....
create LSmax -w 1000;
wks.col1.type=1;
worksheet -i 0 fileN;
worksheet -i 1 xmax;
worksheet -i 2 ymax;
worksheet -i 3 integ;
worksheet -i 4 x1integ;
worksheet -i 5 x2integ;
label -s %M;
loop(ii,B,E){
integrate LSmag_f$(ii) -b 60 -e 2048;//find Max inbetween 60~2048 of row.
x=integ.x0;
i=x-p;
j=x+q;
integrate LSmag_f$(ii) -b i -e j;
LSmax_fileN[ii+1]=ii;
LSmax_xmax[ii+1]=integ.x0;
LSmax_ymax[ii+1]=integ.y0;
LSmax_integ[ii+1]=integ.area;
LSmax_x1integ[ii+1]=integ.x1;
LSmax_x2integ[ii+1]=integ.x2;
};
type -b save file;

/////////////////////////////////////////////////////////////////

```

```

//Load PtNMR data
//////////////////////////////////////////////////////////////////////////////////////////////////////////////////////////////////;
[LoadPt]
type -b Did you check parameters?;
//Parameters.....
%F=%(para,2,1); //data folder
%M=%(para,2,2); //save file name
B=%(para,2,3); //begining file;
E=%(para,2,4); //end file;
//.....;
//This script import ptnmr#.dat files and save it within one worksheet. ;
//Jan13,2006 Hyunchang Choi;
//.....
create PtNMR -w 2048;
wks.col1.type=1;
label -s %M;
win -t data 1fixedFN.otw Pt;
loop(ii,B,E){ //loop() is more stable than for()
%B=%F\PtNMR$(ii).dat;
win -a Pt;
open -w %B;
win -a PtNMR;
worksheet -i ii f$(ii);
copy -a Pt_A PtNMR_f$(ii);
};
win -cd pt;
type -b save file;

//////////////////////////////////////////////////////////////////////////////////////////////////////////////////////////////////
//Sum PtNMR signal
//////////////////////////////////////////////////////////////////////////////////////////////////////////////////////////////////;
[SumPt]
type -b Did you check parameters?;
//Parameters.....
%M=%(para,2,2); //save file name
B=%(para,2,3); //beginning file;
E=%(para,2,4); //end file;
a=%(para,2,7); //beginning of sum;
z=%(para,2,8); //end of sum;
//.....;
create temp -w 10000;
worksheet -i 0 abs;
worksheet -i 1 sel;
set temp_sel -e 10000; //needed for copy command below
create ptSum -w 1000;
wks.col1.type=1;

```

```
worksheet -i 0 fileN;
worksheet -i 1 sum;
worksheet -i 2 InvSum;
wks.col2.label$=$(a)t$(z);
wks.labels();
label -s %M;
for(ii=B;ii<=E;ii++){
temp_abs=abs(PtNMR_f$(ii));
copy -b a temp_abs temp_sel -b a -e z;
sum(temp_sel); //using internal function is much faster than using loop for sum
PtSum_fileN[ii+1]=ii;
PtSum_sum[ii+1]=sum.total;
};
type -b save file;
```

APPENDIX E  
TRANSPORT MEASUREMENT OF  $\text{Ca}_{1.5}\text{Sr}_{0.5}\text{RuO}_4$

**E.1 Overview**

In-plane electrical transport measurements were performed on  $\text{Ca}_{1.5}\text{Sr}_{0.5}\text{RuO}_4$  in the presence of magnetic fields up to 15 T applied along the c-axis and in the direction  $20^\circ$  tilted away from that c-axis. Upon substituting Sr with isovalent Ca,  $\text{Ca}_{2-x}\text{Sr}_x\text{RuO}_4$  shows an intriguing phase diagram ranging from *p-wave* superconductor at  $x = 2$  to a Mott insulator at  $x \leq 0.2$  (Fig. E-1). The  $x = 0.5$  system investigated in this work is reported to be at the boundary between the magnetic metal ( $x < 0.5$ ) and the paramagnetic metallic phase. A small but distinct increase in resistance was observed at  $T^* \approx 450$  mK on warming, which is represented as the red circle in Fig. E-1. In addition,  $T^*$  decreases with the applied magnetic field, and the feature in resistance disappears around 500 G. Our detailed magneto-resistance measurements reveal unusual behavior in the low temperature and low magnetic field region that, we believe, is directly related to the resistance anomaly observed near 0.5 K in zero magnetic field. Interestingly, all transition temperatures at  $x = 0.5$  are near 1K for the magnetic metal (MM), the structure transition (ST), the spin glass (SG), and the Fermi liquid (FL).

**E.2 Experiments**

The sample was prepared by Rongying Jin in the Mandrus group at Oak Ridge National Laboratory. The conventional 4-wire measurements were performed. Typical sample size was  $1 \times 1 \times 2$  mm. The sample was mounted on thin sapphire plate (1.2 mm in thickness, 6.5 mm in diameter) with GE varnish and four gold wires (1 mm in diameter) were positioned and were fixed on the sapphire plate with GE varnish. Temporarily, the sapphire plate was glued with GE varnish on top of an aluminum plate for convenience to handle. To dry GE varnish it was heated for 2 minute on hot plate with  $100^\circ\text{C}$ . The electrical wires were attached to the sample using a

silver epoxy (EpoTek H20E). After applied between the sample and gold wire, it was heated for 5 minutes on hot plate at 300 °C. This procedure consistently results in  $\sim 1 \Omega$  contact resistance. However, the wire came off easily during cooling or at room temperature and only one sample wired by Juhyun Park, a student of M.W. Meisel, was survived through thermal cycles. After all 4 wires were set, the sapphire plate was removed from the aluminum plate and glued on the sample stage of the dilution cryostat. A test sample shown in Fig. E-2 was prepared by winding gold wire around the sample for secure contact. However, its resistance continuously increased in high fields and did not produce reliable results. The winding of a gold wire might cause too much Joule heating by eddy current.

It is crucial to have a low contact resistance to make low temperature transport measurements especially for highly conducting samples. A low sample resistance requires a high excitation (current) to have a reasonable S/N. However, the high current causes a significant heating mainly at the contact. Maeno group used Dupont silver paint 6838 [Ohm00] instead of EpoTek H20E used in our experiments. It is worth to try to evaporate small gold pads directly on the sample and attach wires on the pads using silver epoxy. This method was suggested by Ian Fisher at Stanford University who found that this method provides reliable and low loss contacts for thermal cycling.

The transport measurements were conducted with a LR700 AC resistance bridge typically with 1  $\mu$ V excitation. Most of the data were taken from a dilution cryostat at room B137 and a magneto resistance with tilted field was taken at Bay #3 in the Microkelvin Laboratory.

### **E.3 Results and Discussion**

The temperature dependences of resistance at zero field are presented for high temperatures (Fig. E-3) and for low temperatures (Fig. E-4). An abnormal drop in resistance was observed near 0.5 K. For 1  $\mu$ V excitation, the plot shows linear dependence in temperature

instead of the quadratic dependence which is characteristic for the Fermi liquid. In 2D metal, the linear  $T$  dependence of  $R$  is expected by Moriya *et al.* when the system is near antiferromagnetic instability [Mor90]. Below 0.3 K, the measurement with 2  $\mu\text{V}$  excitation shows consistently higher resistance than the one with 1  $\mu\text{V}$  excitation. The difference between two measurements became more pronounced as temperature lowered indicating that there was a substantial heating at this excitation level. To address this issue, we conducted systematic measurements at various excitation levels at several fixed temperatures. The temperature of the sample plate is P-I-D controlled at a constant temperature within 0.5% of the set temperature and the resistance was measured using various excitation levels from 1 – 3  $\mu\text{V}$ . Figure E-5 shows the result of this study. The effect of heating is clearly demonstrated in this plot. The resistance measured as the excitation level increased. This is consistent with our interpretation that the change in the resistance is caused by heating since the sample shows metallic behavior in this temperature range. The resistance shows linear excitation dependence and the slopes of the linear dependence at each temperature are plotted in Fig. E-6. One can extract zero excitation sample resistance value by extrapolating to the zero excitation point for each temperature. The orange line in Fig. E-4 was obtained in this manner and represents an estimated zero heating resistance which shows a linear temperature dependence.

The magneto resistance (MR) for a field perpendicular to the plane is presented in Fig. E-7 for wide range of fields. A detailed low field MR is displayed in Fig E-8. The MR increases with a field and dip around 40 kG. Above 40 kG, the MR decreases and finally crosses the zero at 70 kG. We observed unique features in low fields which have never been reported on this material. The inset shows the details of sharp increases in MR at low fields (shoulder like structures). This shoulder structure gets smaller and moves to a lower fields as  $T$  increases, and

the structure completely disappears at around 450 mK where the zero field anomaly in resistance was observed. In the low field region, the MR increases linearly and crosses over to a general quadratic behavior in higher fields. More interestingly, unexpected dips in MR were observed below 100 G. As temperature increased, these dips also moved to zero field and disappeared above 450 mK. The positions in field and temperature of the shoulder structures and dips are plotted in Fig. E-9. As the extended lines suggest, two features seem to converge to the same temperature where the zero field resistance anomaly was observed. This indicates that both features are coming from the same origin or that one induces the other as like the structure transition induce the magnetic metal transition [Nak03].

MR with the field applied  $20^\circ$  away from the c-axis was measured and displayed along with the one with the fields perpendicular to the plane. While the shoulder structure is still present, the low field dip structure is missing. Unfortunately, this project ended prematurely because the sample leads lost contacts in a magnet quench occurred during a field sweep.

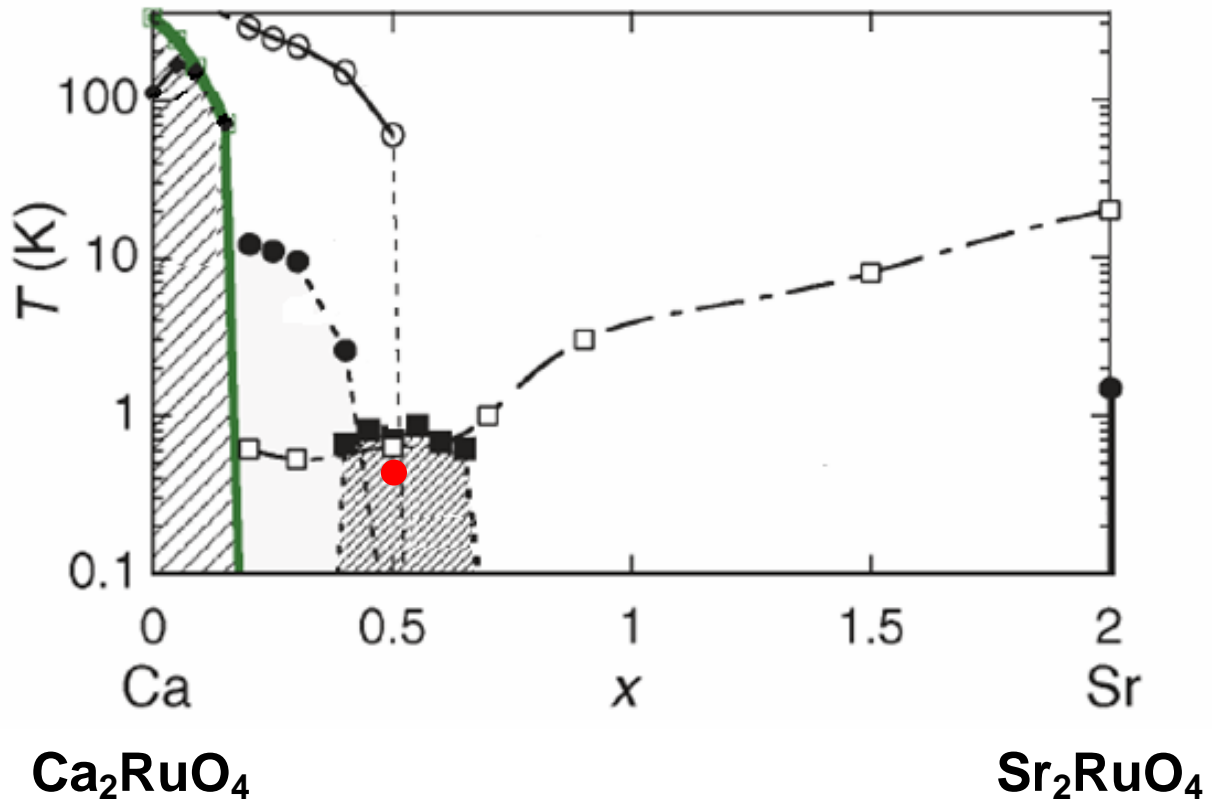


Figure E-1. A Zero field Phase diagram of  $\text{Ca}_{2-x}\text{Sr}_x\text{RuO}_4$  from S. Nakatsuji *et al.* [Nak03]. As the Ca is substituted with Sr, the phase of the sample changes from the antiferromagnetic insulator (AFI) to the magnetic metal (MM) and to the paramagnetic metal (PM). The AFI and MM transitions are represented green line and closed circle.  $\text{Sr}_2\text{RuO}_4$  is a superconductor (SC) below 1.1 K. For the low concentration region of Sr, the temperatures for structure transitions are marked as  $T_s$  (open circle). Their heat capacity and resistance measurement show that the metal phases are always Fermi liquid below  $T_{FL}$  (open square). In the shaded area around  $x = 0.5$ , the spin glass properties were observed from their susceptibility measurements. The red circle represents a point where the abnormal step in our resistance measurement was observed during a temperature sweep. Reprinted figure with permission from S. Nakatsuji, D. Hall, L. Balicas, Z. Fisk, K. Sugahara, M. Yoshioka, and Y. Maeno, *Phys. Rev. Lett.* **90**, 137202 (2003). Copyright (2003) by the American Physical Society.



Figure E-2. Picture of a test sample. The gold wires was wound the sample for better contact. Later it turned out that the winding loop caused heating problem (see text).

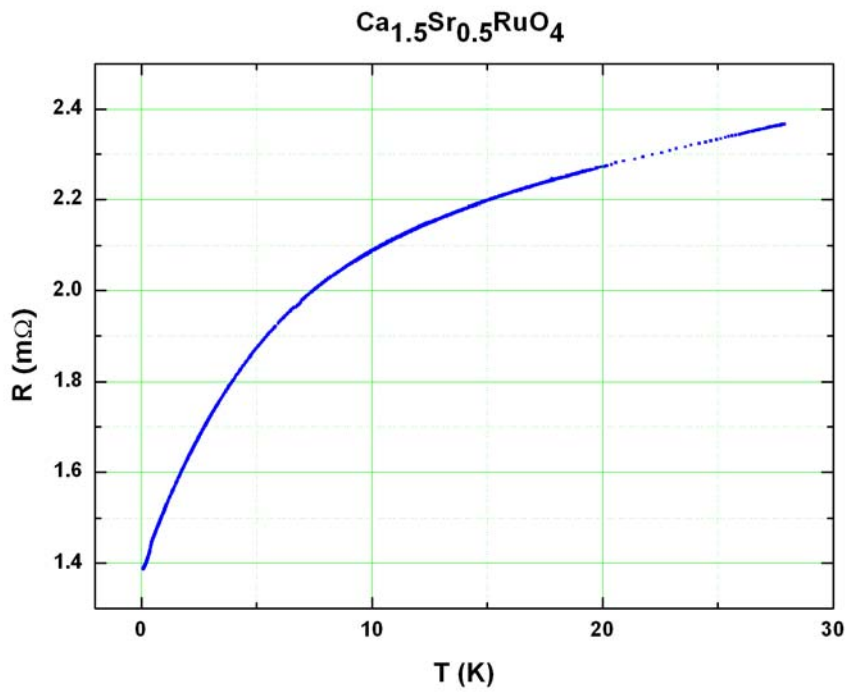


Figure E-3. Temperature dependence of the resistance in the absence of magnetic fields.

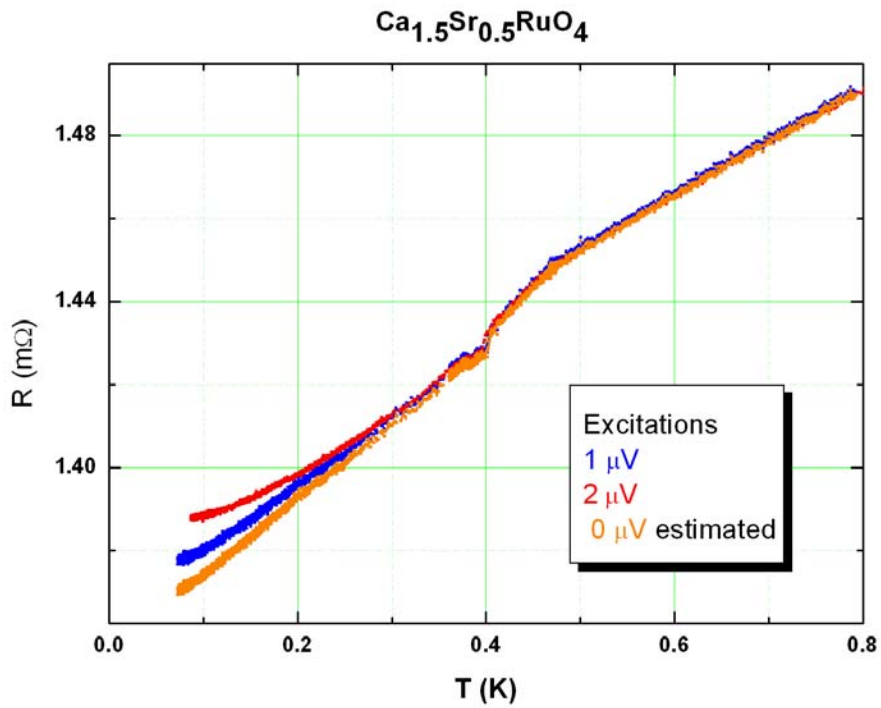


Figure E-4. Resistance vs. temperature for various levels of excitation at low temperature.

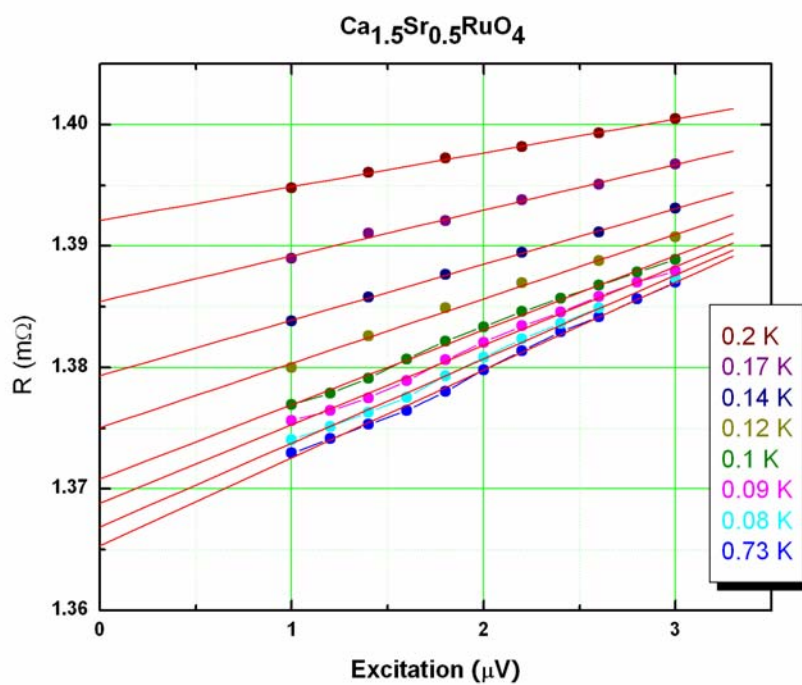


Figure E-5. The excitation dependence of the resistance for each temperature.

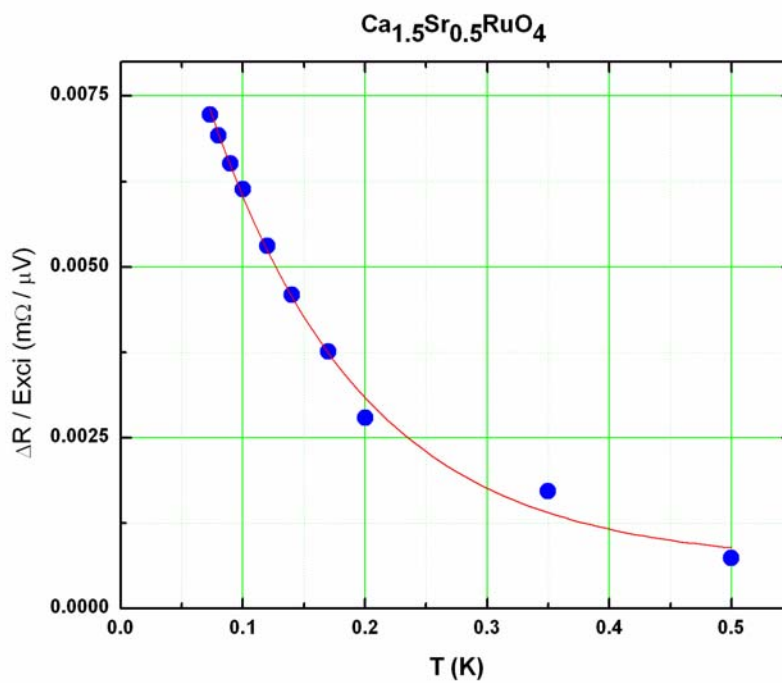


Figure E-6. The temperature dependence of the slopes in Fig E-5.

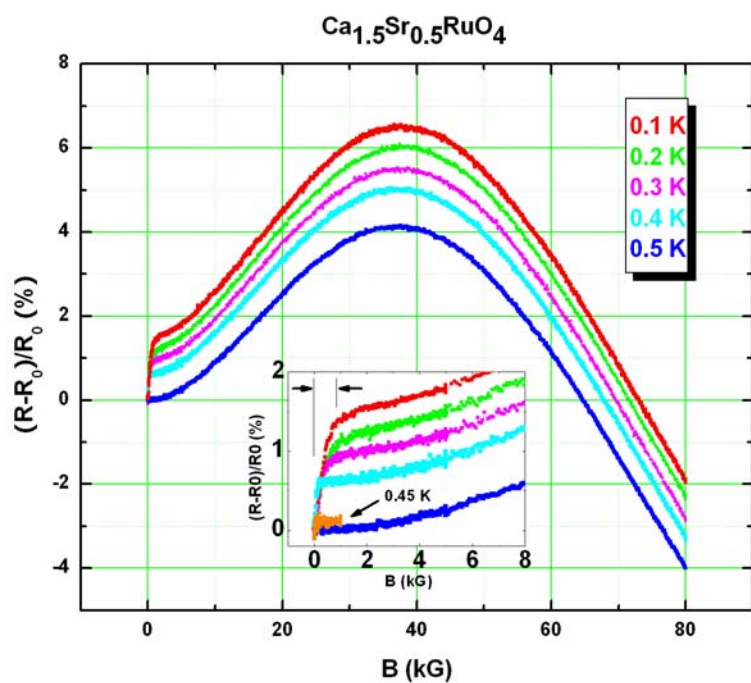


Figure E-7. Normalized magneto resistance.

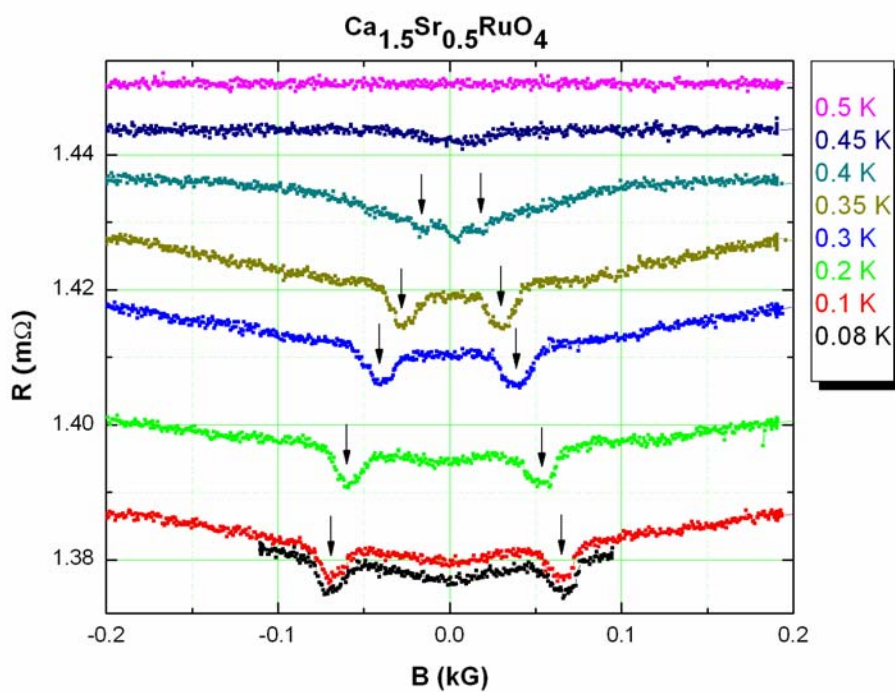


Figure E-8. Field sweeps below 200 G.

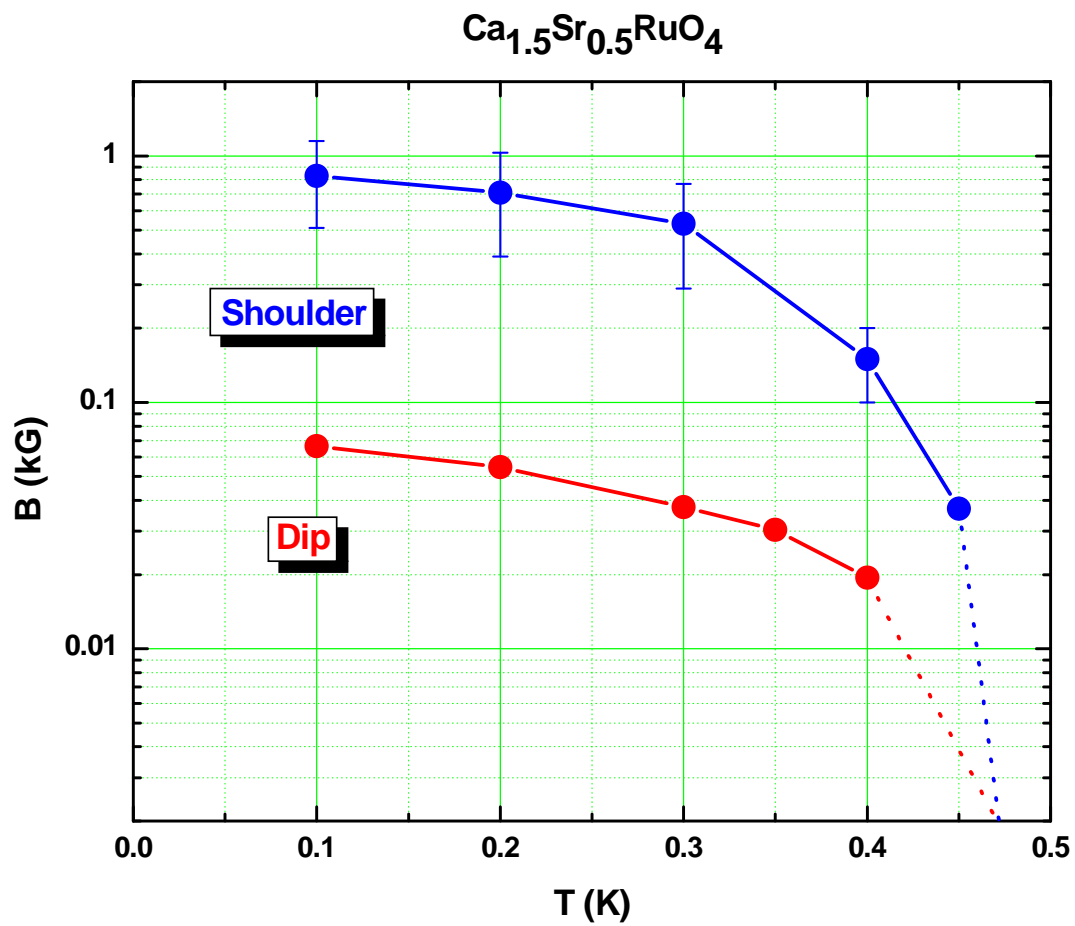


Figure E-9. The position of the shoulder and dip structure in fields vs. temperature.

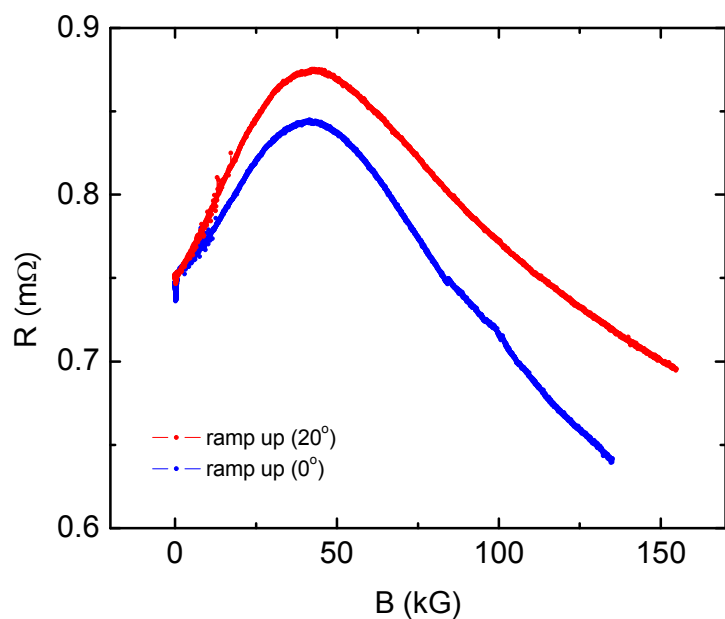


Figure E-10. Magneto resistance for fields perpendicular to the plane (blue) and  $20^\circ$  tilted away from the c-axis (red) at 20mK.

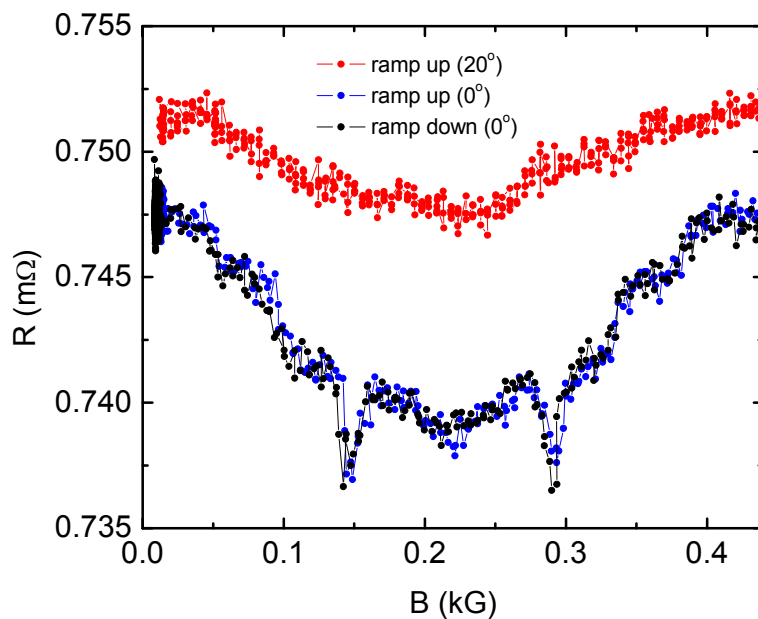


Figure E-11. Magneto resistance for low fields perpendicular to the plane (blue) and  $20^\circ$  tilted away from the c-axis (red) at 20mK.

APPENDIX F  
NEEDLE VALVE FOR DR137

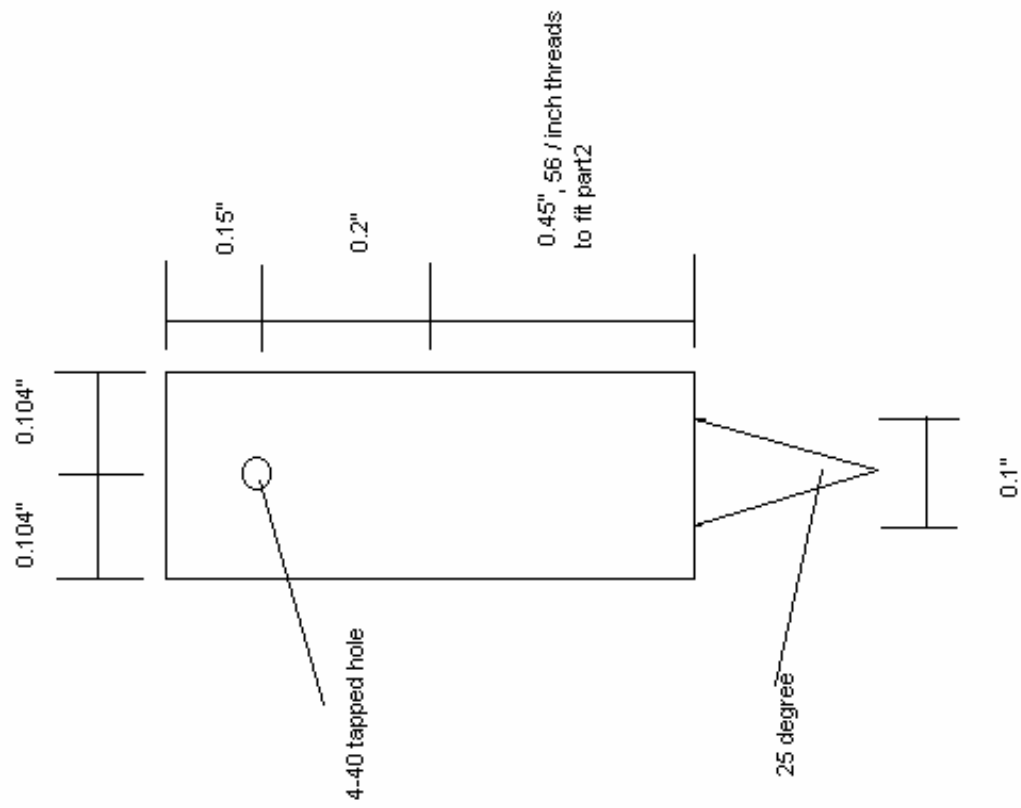
As a part of maintenance for the cryostat at B137 in Physics building (DR137), the needle valve for 1K pot was installed to prevent frequent impedance block.

Needle Valve part1

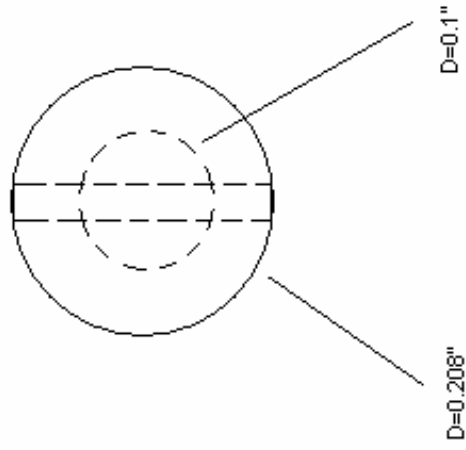
material: brass  
quantity: 1

dec23,2003

(front view)



(top view)

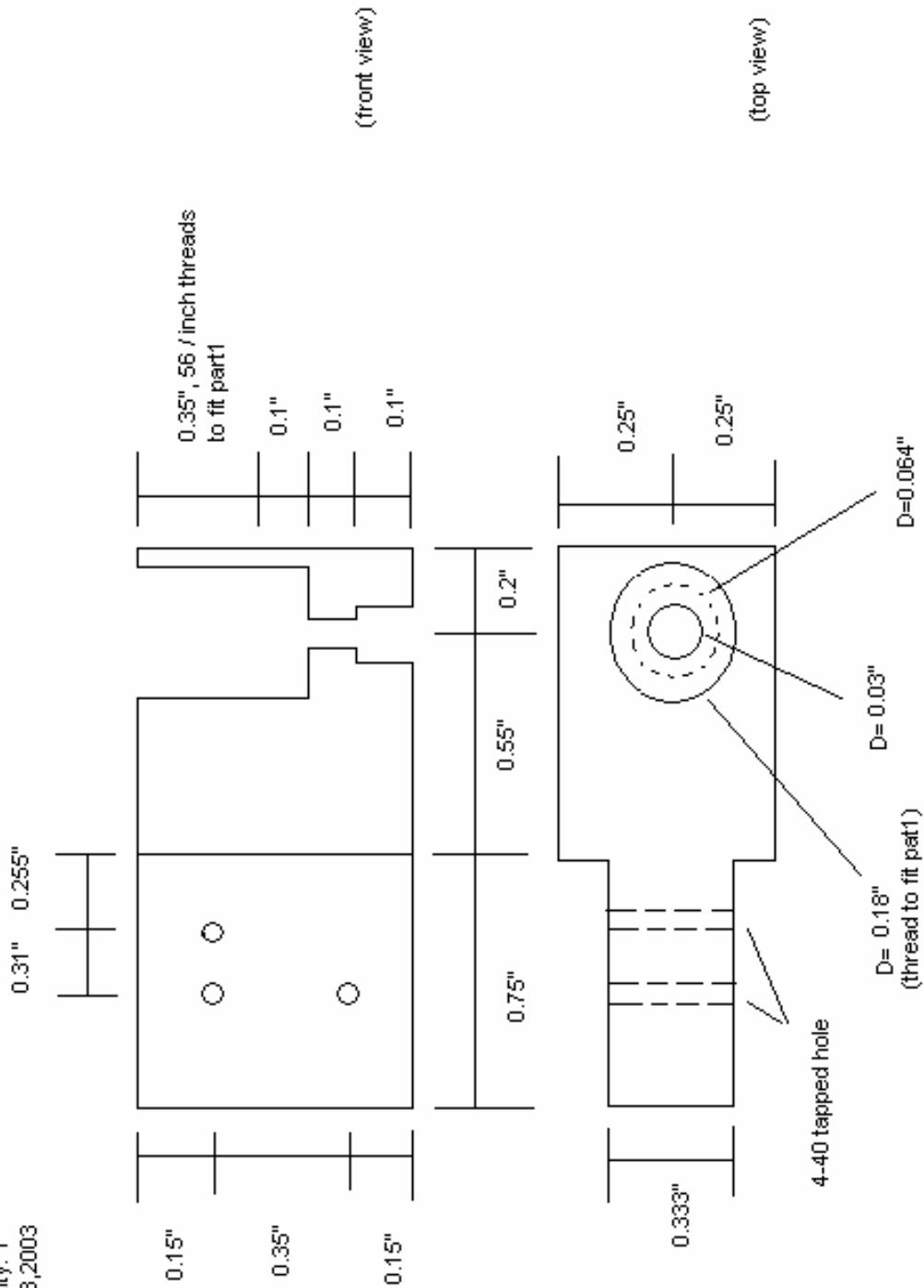


Needle Valve part2

material: brass

quantity: 1

dec23,2003

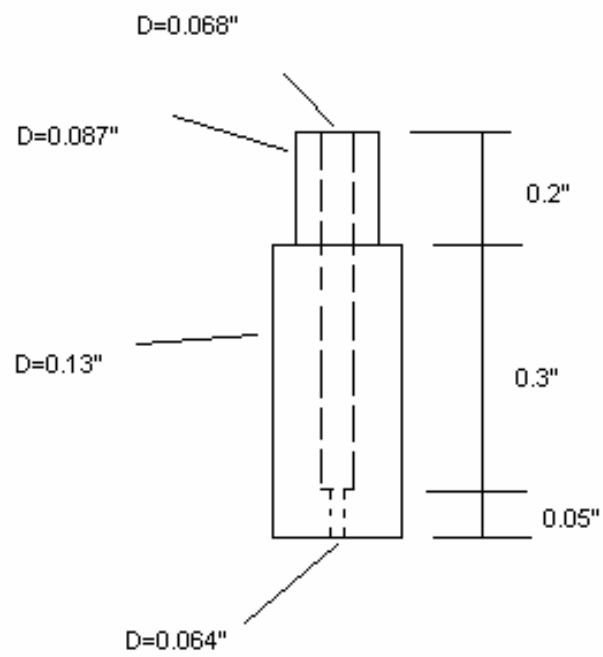


Needle Valve part3

material: brass

quantity: 2

dec23,2003



## LIST OF REFERENCES

- [Abe61] W.R. Abel, A.C. Anderson and J.C. Wheatley, Phys. Rev. Lett. **7**, 299 (1961).
- [Abe65] W.R. Abel, A.C. Anderson, W.C. Black and J.C. Wheatley, Physics **1**, 337 (1965).
- [Abe66] W.R. Abel, A.C. Anderson and J.C. Wheatley, Phys. Rev. Lett. **17**, 74 (1966).
- [Abr61] A.A. Abrikosov and L.P. Gorkov, Sov. Phys. JETP **12**, 1243 (1961).
- [All98] H. Alles, J.J. Kaplinsky, P.S. Wootton, J.D. Reppy and J.R. Hook, Physica B **255**, 1 (1998).
- [All99] H. Alles, J.J. Kaplinsky, P.S. Wootton, J.D. Reppy, J.H. Naish, and J.R. Hook, Phys. Rev. Lett. **83**, 1367 (1999).
- [Amb73] V. Ambegaokar and M. D. Mermin, Phys. Rev. Lett. **30**, 81 (1973).
- [And59] P.W. Anderson, J. Phys. Chem. Solids **11**, 26 (1959).
- [And60] P.W. Anderson and P. Morel, Physica **26**, 671 (1960).
- [And61] P.W. Anderson and P. Morel, Phys. Rev. **123**, 1911 (1961).
- [And73] P.W. Anderson and W.F. Brinkman, Phys. Rev. Lett. **30**, 1108 (1973).
- [And75] P.W. Anderson and W.F. Brinkman, in *The Helium Liquids*, edited by J.G.M. Armitage and I.E. Farquhar (Academic Press, New York, 1975) p. 315.
- [Aoy05] K. Aoyama and R. Ikeda, Phys. Rev. B **72**, 012515 (2005).
- [Aoy06] K. Aoyama and R. Ikeda, Phys. Rev. B **73**, 060504 (2006).
- [Bal63] R. Balian and N.R. Werthamer, Phys. Rev. **131**, 1553 (1963).
- [Bar57] J. Bardeen, L.N. Cooper and J.R. Schrieffer, Phys. Rev. **108**, 1175 (1957).
- [Bar99] G. Baramidze and G. Kharadze, JETP **88**, 415 (1999).
- [Bar00a] G. Baramidze and G. Kharadze, Physica B **284**, 305 (2000).
- [Bar00b] B. I. Barker, Y. Lee, L. Polukhina, and D. D. Osheroff, Phys. Rev. Lett. **85**, 2148 (2000).
- [Bar02] G. Baramidze and G. Kharadze, J. Phys. Condens. Matter **14**, 7471 (2002).
- [Bar03] G.A. Baramidze and G. A. Kharadze, arXiv: cond-matt/0307612.
- [Bar06] G.A. Baramidze and G.A. Kharadze, arXiv: cond-matt/0605054.

- [Bau04a] J.E. Baumgardner, Y. Lee, D.D. Osheroff, L.W. Hrubesh, and J.F. Poco, Phys. Rev. Lett. **93**, 055301 (2004).
- [Bau04b] J.E. Baumgardner and D.D. Osheroff, Phys. Rev. Lett. **93**, 155301 (2004).
- [Bet65] D.S. Betts, D.E. Keen and J. Wilks, Proc. R. Soc. A **284**, 125 (1965).
- [Bio55a] M.A. Biot, J. Acoust. Soc. Am. **28**, 168 (1956).
- [Bio55b] M.A. Biot, J. Acoust. Soc. Am. **28**, 179 (1956).
- [Bol71] D. I. Bolef and J. G. Miller, in *Physical Acoustics*, edited by W. P. Mason and R. N. Thurson (Academic Press, New York, 1971).
- [Bru01] P. Brussard, S.N. Fisher, A.M. Guénault, A.J. Hale, N. Mulders, and G.R. Pickett, Phys. Rev. Lett. **86**, 4580 (2001).
- [Buc81] L.J. Buchholtz and G. Zwicknagl, Phys. Rev. B **23**, 5788 (1981).
- [Cas79] B. Castaing and P. Nozieres, J. Phys. **40**, 257 (1979).
- [Cas80] B. Castaing, J. Phys. Lett. **41**, 333 (1980).
- [Cho04a] H.C. Choi, A.J. Gray, C.L. Vicente, J.S. Xia, G. Gervais, W.P. Halperin, N. Mulders, and Y. Lee, Phys. Rev. Lett. **93**, 145302 (2004).
- [Cho04b] H. Choi, K. Yawata, T.M. Haard, J.P. Davis, G. Gervais, N. Mulders, P. Sharma, J.A. Sauls, and W. P. Halperin, Phys. Rev. Lett. **93**, 145301 (2004).
- [Dag01] E. Dagotto, T. Hotta, and A. Moreo, Phys. Rep. **344**, 1 (2001).
- [Dmi03] V.V. Dmitriev, I.V. Kosarev, N. Mulders, and V.V. Zavjalov, Physica B **329**, 320 (2003).
- [Dob00] E.R. Dobbs, *Helium Three* (Oxford University Press inc., New York, 2000) p.487.
- [Dvo93] J. Dvorkin and A. Nur, Geophysics **58**, 524 (1993).
- [Esk83] G. Eska, K. Neumaier, W. Schoepe, K. Uhlig, and W. Wiedemannet, Phys. Rev. B **27**, 5534 (1983).
- [Fis03] S.N. Fisher, A.M. Guenault, N. Mulders, and G.R. Pickett, Phys. Rev. Lett. **91**, 105303 (2003).
- [Fom03] I.A. Fomin, JETP Lett. **77**, 240 (2003).
- [Fom04] I. A. Fomin, J. Low Temp. Phys. **134**, 769 (2004) ; arXiv: cond-matt/0401639.
- [Fom06] I. A. Fomin, arXiv: cond-matt/0605126.

- [Fri92] J. Fricke and A. Emmerling, *Structure and Bonding* **77**, 37 (1992).
- [Fuk03] H. Fukuyama, K. Yawata, D. Ito, H. Ikegami and H. Ishimoto, *Physica B* **329**, 1560 (2003).
- [Ger01] G. Gervais, R. Nomura, T.M. Haard, Y. Lee, N. Mulders and W.P. Halperin, *J. Low Temp. Phys.* **122**, 1 (2001).
- [Ger02a] G. Gervais, K. Yawata, N. Mulders, and W. P. Halperin, *Phys. Rev. B* **66**, 054528 (2002).
- [Ger02b] G. Gervais, Ph.D. thesis, Northwestern University, 2002.
- [Gol98] A. Golov, J.V. Porto and J.M. Parpia, *Phys. Rev. Lett.* **80**, 4486 (1998).
- [Gol99] A. Golov, D.A. Gella, and J.M. Parpia, *Phys. Rev. Lett.* **82**, 3492 (1999).
- [Gre86] D. S. Greywall, *Phys. Rev. B*, **33**, 7520 (1986).
- [Haa00] T.M. Haard, G. Gervais, R. Nomura and W.P. Halperin, *Physica B* **284**, 289 (2000).
- [Haa01] T.M. Haard, Ph.D. thesis, Northwestern University, 2001.
- [Hah93] I. Hahn, Ph.D. thesis, University of Southern California, 1993.
- [Hai99] T.J. Haire and C.M. Langton, *Bone* **24**, 291 (1999).
- [Hal90] W.P. Halperin and E. Varoquaux, in *Helium Three*, edited by W.P. Halperin and L.P. Pitaevskii (North-Holland, Amsterdam, 1990) p. 353.
- [Hal04] W.P. Halperin and J.A. Sauls, arXiv: cond-matt/0408593.
- [Ham72] E.L. Hamilton, *Geophysics* **37**, 620 (1972).
- [Han98] R. Hanninen, T. Setala and E.V. Thuneburg, *Physica B* **255**, 11 (1998).
- [He69] A.J. Heeger, *Solid State Physics*, edited by F. Seitz, D. Turnbull, and H. Ehrenreich (Academic, New York, 1969), **23**, p. 283.
- [He02a] J.Z. He, A.D. Corwin, N. Mulders, J.M. Parpia, J.D. Reppy and M.H.W. Chan, *J. Low Temp. Phys.* **126**, 679 (2002).
- [He02b] J. He, A.D. Corwin, J.M. Parpia, and J.D. Reppy, *Phys. Rev. Lett.* **89**, 115301 (2002).
- [Hig03] S. Higashitani, T. Ichikawa, M. Yamamoto, and K. Nagai, *Physica B* **329**, 299 (2003).
- [Hig05] S. Higashitani M. Miura, M. Yamamoto, and K. Nagai, *Phys. Rev. B* **71**, 134508 (2005).

- [Hig06] S. Higashitani, M. Miura and K. Nagai, Informal meeting on liquid  $^3\text{He}$  in aerogel, in *International Symposium on Quantum Fluids and Solids* (QFS), 2006.
- [Hri01] L. Hristakos, Ph. D. thesis, University of Bayreuth, 2001.
- [Ich01] T. Ichikawa, M. Yamamoto, S. Higashitani, and K. Nagai, *J. Phys. Soc. Jap.* **70**, 3483 (2001).
- [Isr84] U.E. Israelsson, B.C. Crooker, H.M. Bozler, and C.M. Gould, *Phys. Rev. Lett.* **53**, 1943 (1984).
- [Joh89] D.L. Johnson, *Phys. Rev. Lett.* **63**, 580 (1989).
- [Joh94a] D.L. Johnson, D.L. Hemmick and H. Kojima, *J. Appl. Phys.* **76**, 104 (1994).
- [Joh94b] D.L. Johnson, T.J. Plona and H. Kojima, *J. Appl. Phys.* **76**, 115 (1994).
- [Kam11] O.H. Kamerlingh, *Leiden Commun.* **108**; *Proc. R. Acad. Amsterdam* **11**, 168 (1911).
- [Kee63] B.E. Keen, P.W. Mathews and J. Wilks, *Phys. Lett.* **5**, 5 (1963).
- [Kee65] B.E. Keen, P.W. Matthews and J. Wilks, *Proc. R. Soc. A* **284**, 125 (1965).
- [Ket75] J.B. Ketterson, P.R. Roach, B.M. Abraham and P.D. Roach in *Quantum Statistics and the Many-Body Problem*, edited by S.B. Trickey, W.P. Kirk and J.W. Dufty (Plenum, New York, 1975), p.35.
- [Kim93] S.B. Kim, J.Ma, and M.H.W. Chan, *Phys. Rev. Lett.* **71**, 2268 (1993).
- [Kra80] H.L. Krauss, C.W. Bostian and F.H. Raab, *Solid State Radio Engineering* (John Wiley & Sons, New York, 1980) p. 272.
- [Nak03] S. Nakatsuji, D. Hall, L. Balicas, Z. Fisk, K. Sugahara, M. Yoshioka, and Y. Maeno, *Phys. Rev. Lett.* **90**, 137202 (2003)
- [Lan56] L.D. Landau *Zh. Eksp. Teor. Fiz.* **30**, 1058 (1956) [*Sov. Phys. JETP* **3**, 920 (1957)].
- [Lan57] L.D. Landau, *Zh. Eksp. Teor. Fiz.* **32**, 59 (1957) [*Sov. Phys. JETP* **5**, 101 (1957)].
- [Lan58] L.D. Landau, *Zh. Eksp. Teor. Fiz.* **35**, 97 (1958) [*Sov. Phys. JETP* **8**, 70 (1959)].
- [Lan59] L.D. Landau and E.M. Lifshitz, *Statistical Physics* (Pergamon, London, 1959) p.178.
- [Lar65] A.I. Larkin, *JETP Lett.* **2**, 130 (1965).
- [Lau73] P.C. Lauterbur, *Nature* **242**, 190 (1973).
- [Lee85] P.A. Lee and T.V. Ramakrishnan, *Rev. Mod. Phys.* **57**, 287 (1985).

- [Lee97] Y. Lee, Ph.D. Thesis, Northwestern University, 1997.
- [Lee99] Y. Lee, T.M. Haard, W.P. Halperin, and J.A. Sauls, *Nature* **400**, 431 (1999).
- [Leg90] A.J. Leggett and S.K. Yip, in *Helium Three*, edited by W.P. Halperin and L.P. Pitaevskii (North-Holland, Amsterdam, 1990) p.523.
- [Li88] Y.H. Li and T.L. Ho, *Phys. Rev. B* **38**, 2362 (1988).
- [Mae94] Y. Maeno, H. Hashimoto, K. Yoshida, S. Nishizaki, T. Fujita, J.G. Bednorz and F. Lichtenberg, *Nature* **372**, 532 (1994).
- [Mar00] M.P. Marder, *Condensed Matter Physics* (John Wiley & Sons, New York, 2000) p.462.
- [Mas00] N. Masuhara, B.C. Watson and M.W. Meisel, *Phys. Rev. Lett.* **85**, 2537 (2000).
- [Mat97] K. Matsumoto, J.V. Porto, L. Pollack, E.N. Smith, T.L. Ho, and J.M. Parpia, *Phys. Rev. Lett.* **79**, 253 (1997); **79**, 2922 (E) (1997).
- [Mor90] T. Moriya, Y. Takahashi and K. Ueda, *J. Phys. Soc. Jpn.* **59**, 2905 (1990).
- [Nak03] S. Nakatsuji, D. Hall, L. Balicas, Z. Fisk, K. Sugahara, M. Yoshioka, and Y. Maeno, *Phys. Rev. Lett.* **90**, 137202 (2003).
- [Naz04a] E. Nazaretski, N. Mulders, and J.M. Parpia, *JETP Lett.* **79**, 383 (2004).
- [Naz04b] E. Nazaretski, N. Mulders, and J.M. Parpia, *J. Low Temp. Phys.* **134**, 763 (2004).
- [Naz05] E. Nazaretski, D. M. Lee and J. M. Parpia, *Phys. Rev. B* **71**, 144506 (2005).
- [Nom00] R. Nomura, G. Gervais, T.M. Haard, Y. Lee, N. Mulders, and W.P. Halperin, *Phys. Rev. Lett.* **85**, 4325 (2000).
- [Noz64] P. Nozieres, *Theory of interacting Fermi systems* (W.A. Benjamin, New York, 1964).
- [Ohm00] E. Ohmichi, Y. Maeno, S. Nagai, Z.Q. Mao, M.A. Tanatar, and T. Ishiguro, *Phys. Rev. B* **61**, 7101 (2000).
- [Oli33] M.L.E. Oliphant, B.B. Kinsey and E. Rutherford, *Proc. R. Soc. Lond. A* **141**, 722 (1933).
- [Osh72a] D.D. Osheroff, R.C. Richardson and D.M. Lee, *Phys. Rev. Lett.* **28**, 885 (1972).
- [Osh72b] D.D. Osheroff, W.J. Gully, R.C. Richardson, and D.M. Lee, *Phys. Rev. Lett.* **29**, 920 (1972).
- [Osh74] D.D. Osheroff and P.W. Anderson, *Phys. Rev. Lett.* **33**, 686 (1974).
- [Pau74] D.N. Paulson, H. Kojima, and J.C. Wheatley, *Phys. Rev. Lett.* **32**, 1098 (1974).

- [Pol06] J. Pollanen, S. Blinstein, H. Choi, J.P. Davis, T.M. Lippman, L.B. Lurio, and W.P. Halperin, arXiv: cond-matt/0606784.
- [Por95] J.V. Porto and J.M. Parpia, Phys. Rev. Lett. **74**, 4667 (1995).
- [Por99] J.V. Porto and J.M. Parpia, Phys. Rev. B **59**, 14583 (1999).
- [Pri93] S.R. Pride, F.D. Morgan and A.F. Gangi, Phys. Rev. B **47**, 4964 (1993).
- [Rai77] D. Rainer and M. Vuorio, J. Phys. C **10**, 3093 (1977).
- [Rai98] D. Rainer and J.A. Sauls, J. Low Temp. Phys. **110**, 525 (1998).
- [Rem98] P. Remeijer, L.P. Roobol, S.C. Steel, R. Jochemsen and G. Frossati, J. Low Temp. Phys. **111**, 119 (1998).
- [Roa76] P.R. Roach and J.B. Ketterson, Phys. Rev Lett. **36**, 736 (1976).
- [Roa77] P.R. Roach and J.B. Ketterson, in *Quantum Fluids and Solids*, edited by S.B. Trickey, E.D. Adams, and J.F. Duffy (Plenum Press, New York, 1977) p.223.
- [Rud80] I. Rudnick, 1980, J. Low Temp. Phys. **40**, 287 (1980).
- [Sac99] S. Sachdev, *Quantum Phase Transition* (Cambridge University Press, New York, 1999).
- [Sag84] D.C. Sagan, P.G.N. deVegvar, E. Polturak, L. Friedman, S.S. Yan, E.L. Ziercher, and D.M. Lee, Phys. Rev. Lett. **53**, 1939 (1984).
- [Sau03] J. A. Sauls and P. Sharma, Phys. Rev. B **68**, 224502 (2003).
- [Sha01] P. Sharma and J.A. Sauls, J. Low Temp. Phys. **125**, 115 (2001).
- [Sha03] P. Sharma and J.A. Sauls, Physica B **329**, 313 (2003).
- [Spr95] D.T. Sprague, T.M. Haard, J.B. Kycia, M.R. Rand, Y. Lee, P.J. Hamot, and W.P. Halperin, Phys. Rev. Lett. **75**, 661 (1995).
- [Spr96] D.T. Sprague, T.M. Haard, J.B. Kycia, M.R. Rand, Y. Lee, P.J. Hamot, and W.P. Halperin, Phys. Rev. Lett. **77**, 4568 (1996)
- [Syd49a] S.G. Sydoriak, E.R. Grilly and E.F. Hammel, Phys. Rev. **75**, 303 (1949).
- [Syd49b] S.G. Sydoriak, E.R. Grilly and E.F. Hammel, Phys. Rev. **75**, 1103 (1949).
- [Tan91] Y.H. Tang, I Hahn, H.M. Bozler, and C.M. Gould, Phys. Rev. Lett. **67**, 1775 (1991).
- [Thu98a] E. V. Thuneberg, S. K. Yip, M. Fogelström, and J. A. Sauls, Phys. Rev. Lett. **80**, 2861 (1998).

- [Thu98b] E. V. Thuneberg, arXiv: cond-matt/9802044.
- [Tin96] M. Tinkham, *Introduction to Superconductivity 2<sup>nd</sup> ed.* (McGraw-Hill Inc., New York, 1996) p.394.
- [Tsi02] D. Tsiklauri, J. Acoust. Soc. Am. **112**, 843 (2002).
- [Tsu00] C.C. Tsuei and J.R. Kirtley, Rev. Mod. Phys. **72**, 969 (2000).
- [Ven00] P. Venkataramani and J.A. Sauls, Physic B **284**, 297 (2000).
- [Vic05] C.L. Vicente, H.C. Choi, J.S. Xia, W.P. Halperin, N. Mulders, and Y. Lee, Phys. Rev. B **72**, 094519 (2005).
- [Vol84] D. Vollhardt, 1984, Rev. Mod. Phys. **54**, 99 (1984).
- [Vol90] D. Vollhardt and P. Wolfle, *The Superfluid Phases of Helium Three* (Taylor and Francis, London, 1990).
- [Vol96] G.E. Volovik, JETP Lett. **63**, 301 (1996).
- [Vol05] G.E. Volovik, JETP Lett. **81**, 647 (2005).
- [Vol06] G. E. Volovik, arXiv: cond-matt/0605276.
- [Vor93] T. Vorenkamp, M.C. Aronson, Z. Koziol, K. Bakker, and J.J.M. Franse, Phys. Rev. B **48**, 6373 (1993).
- [War94] K. Warner and J.R. Beamish, Phys. Rev. B **50**, 15896 (1994).
- [Wat00] B.C. Watson, Ph.D. Thesis, University of Florida, 2000.
- [Wat03] B.C. Watson, N. Masuhara and M.W. Meisel, J. Low Temp. Phys. **130**, 77 (2003).
- [Web1] Superfluid phase diagram of helium three, <http://liisteri.hut.fi/Archive>.
- [Whe70] J.C. Wheatley in: *Progress in Low Temperature Physics*, Vol. VI, edited by C.J. Groter (North-Holland, Amsterdam, 1970) p. 77.
- [Wik06] Frequency modulation, <http://en.Wikipedia.org>
- [Wil67] J. Wilks, *Liquid and Solid Helium* (Oxford University Press, 1967) p.487.
- [Wol89] E.L. Wolf, *Principles of Electron Tunneling Spectroscopy*, (Oxford University Press, New York, 1989).
- [Yam88] T. Yamamoto and A. Turgut, J. Acoust. Soc. Am. **83**, 1744 (1988).
- [Yaw01] K. Yawata, Ph.D. thesis, University of Tsukuba, 2001.

[Yip91] S. K. Yip, T. Li, and P. Kumar, Phys. Rev. B **43**, 2742 (1991).

[Zha02] L. Zhang, C. Israel, A. Biswas, R. L. Greene, and A. de Lozanne, Science **298**, 805 (2002).

[Zho89] M.Y. Zhou and P. Sheng, Phys. Rev. B **39**, 12027 (1989).

\*The contents in this dissertation were or will be published at Journals below.\*

H.C. Choi, A.J. Gray, C.L. Vicente, J.S. Xia, G. Gervais, W.P. Halperin, N. Mulders, Y. Lee, Phys. Rev. Lett. **93**, 145302 (2004). “Copyright (2004) by the American Physical Society.”

H.C. Choi, A.J. Gray, C.L. Vicente, J.S. Xia, G. Gervais, W.P. Halperin, N. Mulders, Y. Lee, J. Low Temp. Phys. **138**, 107 (2005). “The original publication is available at [www.springerlink.com](http://www.springerlink.com)”

C.L. Vicente, H.C. Choi, J.S. Xia, W.P. Halperin, N. Mulders, Y. Lee, Phys. Rev. B **72**, 094519 (2005). “Copyright (2005) by the American Physical Society.”

Y. Lee, H.C. Choi, N. Masuhara, B.H. Moon, P. Bhupathi, M.W. Meisel, and N. Mulders, will appear in J. Low Temp. Phys. “The original publication is available at [www.springerlink.com](http://www.springerlink.com)”

H.C. Choi, N. Masuhara, B.H. Moon, P. Bhupathi, N. Mulders, M.W. Meisel, and Y. Lee, J. Low Temp. Phys., submitted in July 2006. “The original publication is available at [www.springerlink.com](http://www.springerlink.com)”

Y. Lee, H.C. Choi, N. Masuhara, B.H. Moon, P. Bhupathi, M.W. Meisel, and N. Mulders, in preparation.

H.C. Choi, N. Masuhara, B.H. Moon, P. Bhupathi, N. Mulders, M.W. Meisel, and Y. Lee, in preparation.

\*Usages for figures cited from published articles are following regulations as written below.\*

Readers may view, browse, and/or download material for temporary copying purposes only, provided these uses are for noncommercial personal purposes. Except as provided by law, this material may not be further reproduced, distributed, transmitted, modified, adapted, performed, displayed, published, or sold in whole or part, without prior written permission from the publisher.

## BIOGRAPHICAL SKETCH

Hyunchang Choi was born in Seoul, Korea, as the eldest son and has two younger sisters. He spent his early childhood in a rural area of Daejeon City, Korea. During his elementary school years, his family moved back to Seoul. His best hobby was competing on math puzzles with classmates at that time. He also enjoyed making pra-models and assembling simple circuits like a clapping switch. In the third year of high school, he received an award as a progressive student. The curiosity for the principle of nature guided him to physics and he began his study of physics at Kyunghee University, Korea, in 1992. Owing to his success in the entrance exam, he was granted a full scholarship for one year. After 2 years of mandatory army service, he decided to continue his study in the USA to learn academics in a more open culture. He joined the Physics Department at the University of Florida in 1999 and joined Professor Lee's group in 2002.